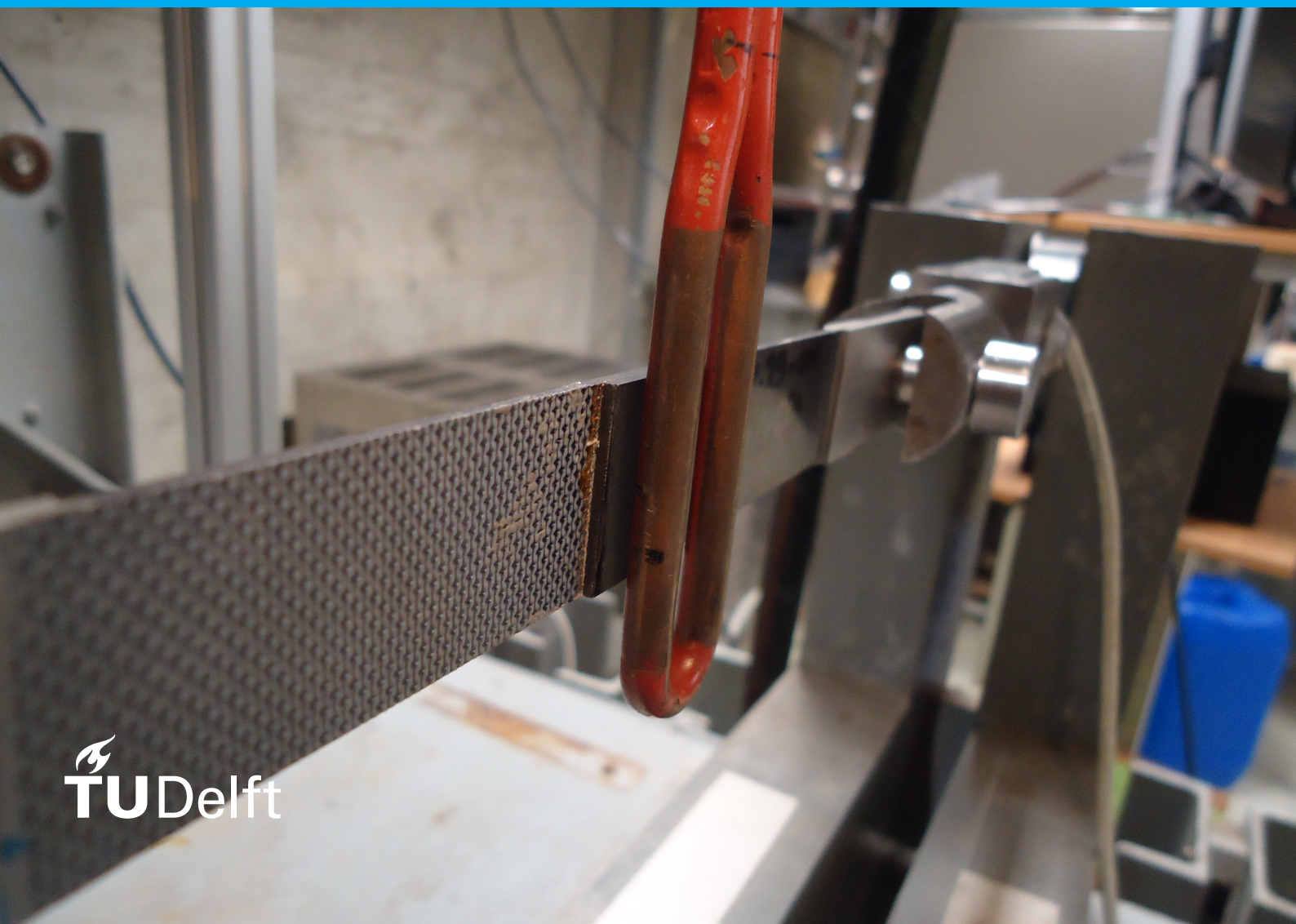
Disassembly of fusion bonded thermoplastic composite joints aided by induction heating

Effects of induction heating on disassembly force and damage patterns

Loïc De Weert

Under supervision of:
Dr. I. Fernandez Villegas

Student number 5139864



TU Delft

Disassembly of fusion bonded thermoplastic composite joints aided by induction heating

Effects of induction heating on disassembly force and damage patterns

by

Loïc De Weert

to obtain the degree of Master of Science
at the Delft University of Technology,
to be defended publicly on Friday September 24th, 2021 at 10:00 AM.

Student number:	5139864	
Project duration:	November 9th, 2020 – September 24th, 2021	
Thesis committee:	Dr. ir. I. Fernandez Villegas,	TU Delft, supervisor
	Dr. ir. D. M. J. Peeters,	TU Delft
	Ir. J. Sinke,	TU Delft

An electronic version of this thesis is available at `http://repository.tudelft.nl/`.

TU Delft

Preface

A thesis report would never be successfully completed without the continuous help, guidance and support of many people. Therefore, I will use this preface to express my gratitude towards people who assisted me in this journey.

Firstly I would like to thank Dr. I. Fernandez Villegas for her continuous guidance in the research process. She challenged me to think ahead, helped me to plan the research process and to explain results. Without her support, this thesis would not have been possible.

I would also like to thank the researchers of the Composites Welding Group at the Aerospace Structures and Materials Laboratory, for their patience and answers to my numerous questions. My gratitude also goes to Eirini Tsiangou, who helped me carrying out the literature review at the start of this thesis.

An experimental research in material science requires quite some machinery for the production of samples and the experimental tests. Therefore, I would like to thank all lab technicians who helped me to familiarize with the laboratory equipment I needed. Special thanks to Alexander Uithol and Berthil Grashof, who provided a lot of help and knowledge to build the experimental setup.

Lastly, I would like to express my gratitude to everyone who motivated and supported me throughout my studies. Thank you for your encouraging words when things were not going as planned, and for your warmth and pride when things were going well. I hope you enjoy reading this work, since it would not have been possible without you.

Loïc De Weert
Delft, September 2021

Contents

Abstract vii

List of Figures ix

List of Tables xi

Nomenclature xi

1 Introduction 1

2 Literature review & research questions 3
- 2.1 Literature review . . . 3
  - 2.1.1 Disassembly approaches for adhesive joints . . . 3
  - 2.1.2 Heating mechanisms . . . 3
  - 2.1.3 Ultrasonic welding . . . 5
  - 2.1.4 Knowledge gap . . . 6
- 2.2 Research questions and hypotheses . . . 7

3 Method 9
- 3.1 Model . . . 9
  - 3.1.1 Susceptor material model . . . 9
  - 3.1.2 Laminate material model . . . 13
  - 3.1.3 Model geometry and meshing . . . 15
  - 3.1.4 Model physics . . . 16
  - 3.1.5 Sensitivity analysis . . . 16
  - 3.1.6 Model validation . . . 17
  - 3.1.7 Simulations . . . 17
- 3.2 Experimental . . . 17
  - 3.2.1 Sample preparation . . . 17
  - 3.2.2 Ultrasonic welding . . . 19
  - 3.2.3 Reference case . . . 20
  - 3.2.4 Experimental setup . . . 21
  - 3.2.5 Calibration of the setup sensors . . . 22
  - 3.2.6 Disassembly of co-consolidated joints . . . 25
  - 3.2.7 Microscopic investigation . . . 26

4 Results 27
- 4.1 Model . . . 27
  - 4.1.1 Sensitivity analysis . . . 27
  - 4.1.2 Model validation . . . 28
  - 4.1.3 Model results . . . 31
- 4.2 Experimental . . . 34
  - 4.2.1 Reference case . . . 34
  - 4.2.2 Ultrasonic welding . . . 36
  - 4.2.3 Disassembly . . . 37

5 Discussion 51
- 5.1 Influence of the susceptor on disassembly of co-consolidated joints . . . 51
  - 5.1.1 Heat focusing . . . 51
  - 5.1.2 Influence of the susceptor on the disassembly characteristics . . . 52
  - 5.1.3 Influence of the susceptor on damage patterns . . . 54

5.2 Influence of fusion bonding process type . . . 55
5.2.1 Influence of the joint type on the disassembly characteristics . . . 55
5.2.2 Influence of the joint type on damage patterns . . . 56
5.3 Answering the main research question . . . 57
5.4 Validity of results . . . 57
5.4.1 Sources of uncertainty in measurements. . . . 57
5.4.2 Practical applications . . . 58

6 Conclusions & recommendations 61

A Model equations 63
A.1 Susceptor material model derivation . . . 63
A.1.1 Thermal and electrical conductivity . . . 63
A.1.2 Volume fractions of steel and polymer . . . 64
A.2 Equations of the model physics . . . 64
A.2.1 Magnetic fields interface . . . 64
A.2.2 Heat transfer in solids interface . . . 65

B Sensitivity analysis 67

C Welch's T-test 69

D Microscopy and damage 75
D.1 Fracture surfaces . . . 75
D.2 Cross-sections . . . 79

Bibliography 89

Abstract

Fusion bonding techniques of thermoplastic composites have been attracting much attention in recent years, due to their promising characteristics. These characteristics comprise fast processing, reduction of stress concentrations and reducing required labour [14]. Despite this increasing attention for fusion bonding, disassembly of these bonds is barely researched. Since disassembly is the first step in re-work during manufacturing, repair in-service and recycling at the end of life, research into this topic seems highly viable.

This study investigated disassembly of fusion bonded joints aided by induction heating. Single-lap shear experiments were carried out while heating the joint with an induction coil to research the effect on force required and damage inflicted during disassembly. Co-consolidated samples with and without a metal mesh susceptor as well as ultrasonically welded samples were tested and compared. All samples were made of two adherends consisting of a $[0/-45/90/-45/45/-45]_s$ layup of Toray Cetex® TC1200 carbon fibre/PEEK unidirectional tape. Prior to experiments, an induction heating model was built to facilitate experimental design and to help analyze the effect of the susceptor on the heating process.

Induction heating appeared successful in lowering the disassembly force. Large reductions were achieved, but this came at the cost of thermal damage in the disassembled adherends. This damage mainly occurs at the edges due to the edge effect, which is caused by a local concentration of excitation currents due to constraints in the current paths [18]. For a reduction to around 37% of the original strength, no thermal damage was inflicted during disassembly for all samples, except for one outlier.

Co-consolidated samples with susceptor were relatively easier to disassemble. They required less disassembly energy and reached lower surface temperatures than their susceptorless counterparts. Both the model and damage patterns suggested that interface temperatures were higher than surface temperatures, which was the goal of including a susceptor. As a consequence, lower excitation currents could be applied to limit damage inflicted during disassembly. However, the inclusion of the susceptor also diminished joint strength at room temperature.

Ultrasonically welded samples were most complicated to disassemble. This was presumably caused by pure PEEK energy director remnants at the joint interface acting as an electrically and thermally insulating layer. This likely diminished heat generation at the interface. Additionally, the extra layer of polymer requires more energy and time to soften before fracture. At the lowest load level tested, some samples even failed to break within four minutes, despite suffering thermal damage.

Much research is still required in order to develop this disassembly technique. For more complex parts, testing disassembly by applying peel forces might be more realistic for real-life disassembly. Investigating the influence of changing boundary conditions by testing plates with joints far from the edge might also be interesting, as most damage induced by disassembly was caused by the edge effect. The disassembly method tested in this study could be especially viable for samples with susceptor. Since the susceptor used in this research diminished strength at room temperature, investigating different kinds of susceptors could be an option. Alternatively, the method could be developed further for joints in which a metal mesh susceptor is embedded anyway, such as resistance welded joints.

List of Figures

2.1 The five phases indicated on the power and displacement curves [12] . . . 6

3.1 Unit cell of the susceptor . . . 10
3.2 Transformed unit cell for mesh model, based on Xu and Wirtz [42] . . . 11
3.3 Equivalent resistive network in the horizontal plane [42] . . . 11
3.4 Equivalent resistive model through the thickness . . . 12
3.5 Model geometry . . . 15
3.6 Stacked co-consolidated plates with susceptor . . . 17
3.7 Mould lay-out . . . 18
3.8 Cutting procedure for a co-consolidated plate . . . 18
3.9 Sonotrode and custom-made welding jig . . . 19
3.10 Schematic of how overlap width was measured for ultrasonically welded samples . . . 20
3.11 Measuring the overlap length and width using the mark left behind after fracture . . . 21
3.12 Experimental setup . . . 21
3.13 Calibration curve of the Wheatstone bridge . . . 22
3.14 Thermocouple response in induction field . . . 24
3.15 FLIR data versus coil-facing thermocouple data (TC wire diameter 2 mm) . . . 24
3.16 Positioning of the thermocouples on a sample . . . 25
3.17 Cutting steps for microscopic investigation . . . 26

4.1 Comparison of the model prediction versus experimental measurements for susceptorless co-consolidated samples tested at 300.3 A . . . 29
4.2 Comparison of the model prediction versus experimental measurements for susceptorless co-consolidated samples tested at 499.8 A . . . 29
4.3 Comparison of the model prediction versus experimental measurements for co-consolidated samples with susceptor, for an excitation current of 300.3 A . . . 30
4.4 Comparison of the model prediction versus experimental measurements for co-consolidated samples with susceptor for adjusted properties . . . 30
4.5 Microscopical image of the cross-section of a sample with susceptor . . . 31
4.6 Influence of the coupling distance on the temperature evolution . . . 32
4.7 Eccentricity . . . 32
4.8 Influence of the eccentricity on the temperature evolution . . . 33
4.9 Heating profile at 20 s for susceptorless sample . . . 33
4.10 Heating profile through the thickness at 8 seconds of heating time . . . 34
4.11 Mean lap shear strength at different temperatures for co-consolidated samples . . . 35
4.12 Fracture surfaces of reference case samples tested at 168-170°C . . . 35
4.13 Microscopic images of the cross-section for reference case samples tested at 168-170°C . . . 36
4.14 Fracture surface of an ultrasonically welded sample . . . 36
4.15 Microscopic images of the cross-section for an ultrasonically welded sample . . . 37
4.16 Mean and standard deviation of different disassembly parameters . . . 40
4.17 Evolution of temperature vs. time during disassembly for co-consolidated samples with susceptor (TC wire diameter 1 mm) . . . 41
4.18 Evolution of temperature vs. time during disassembly for the co-consolidated samples without susceptor (TC wire diameter 1 mm) . . . 41
4.19 Evolution of temperature vs. time during disassembly for ultrasonically welded samples (TC wire diameter 1 mm) . . . 42
4.20 Temperature profile across the coil-facing surface . . . 42
4.21 Fracture surfaces of co-consolidated samples with susceptor for different weight-excitation current combinations . . . 43

4.22 Fracture surfaces of co-consolidated samples without susceptor for different weight-excitation current combinations . . . 43
4.23 Sample surfaces of co-consolidated samples without susceptor for 5 kg and 0 kg . . . 44
4.24 Fracture surfaces of ultrasonically welded samples for different weight-excitation current combinations . . . 44
4.25 Spot with different light reflection on the coil-facing adherend of an unbroken sample tested at 0 kg - 499.8 A . . . 45
4.26 Edge of the cross-section of a disassembled sample for 15 kg . . . 45
4.27 Edge of the cross-section of a disassembled sample for 10 kg . . . 46
4.28 Edge of the cross-section of a disassembled sample for 5 kg . . . 46
4.29 Edge of the cross-section of a disassembled sample for 0 kg . . . 47
4.30 Unbroken susceptorless sample, tested at 300.3 A and 5 kg . . . 47
4.31 Full cross-section of both types of co-consolidated samples . . . 47
4.32 Full cross-section of ultrasonically welded samples disassembled at different weight-excitation current combinations . . . 48
4.33 Cross-sections of an ultrasonically welded sample disassembled at 5 kg and 499.8 A . . . 49
4.34 Cross-sections of a co-consolidated sample without susceptor disassembled at 5 kg and 499.8 A 49
4.35 Cross-sections of an ultrasonically welded sample disassembled at 0 kg and 499.8 A . . . 50

5.1 Comparison of reference case experiments with disassembly experiments . . . 52
5.2 Comparison of disassembly energy per unit of coil impedance for co-consolidated samples with and without susceptor . . . 53
5.3 Comparison of disassembly energy per unit of coil impedance for co-consolidated samples without susceptor and ultrasonically welded samples . . . 55
5.4 Example of possible application: the disassembly of an L-shaped stringer fusion bonded to a plate . . . 59

C.1 T-distribution table [24] . . . 70

D.1 Two series of fracture surfaces of co-consolidated samples with susceptor, ordered from highest to lowest weight level . . . 76
D.2 Two series of fracture surfaces of co-consolidated samples without susceptor, ordered from highest to lowest weight level . . . 77
D.3 Two series of fracture surfaces of ultrasonically welded samples, ordered from highest to lowest weight level . . . 78
D.4 Cross-sections of co-consolidated samples disassembled at 15 kg . . . 79
D.5 Cross-sections of co-consolidated samples disassembled at 10 kg . . . 80
D.6 Cross-sections of co-consolidated samples disassembled at 5 kg . . . 81
D.7 Cross-sections of co-consolidated samples disassembled at 0 kg . . . 82
D.8 Damage pattern on cross-sections of co-consolidated samples with susceptor disassembled at 0 kg . . . 83
D.9 Damage pattern on cross-sections of co-consolidated samples without susceptor disassembled at 0 kg . . . 83
D.10 Cross-sections of ultrasonically welded samples disassembled at 15 kg . . . 84
D.11 Cross-sections of ultrasonically welded samples disassembled at 10 kg . . . 84
D.12 Cross-sections of ultrasonically welded samples disassembled at 5 kg . . . 85
D.13 Cross-sections of ultrasonically welded samples disassembled at 0 kg . . . 86
D.14 Cross-sections of co-consolidated samples without susceptor, disassembled at 5 kg . . . 87

List of Tables

3.1 Geometric parameters of the metal mesh . . . 10
3.2 Input material properties and result for susceptor properties . . . 13
3.3 Input material properties and result for laminate properties . . . 14
3.4 Final weld parameters used. . . . 20
3.5 Excitation current per weight level for different types of samples . . . 25

4.1 Results of the sensitivity analysis . . . 28
4.2 Lap shear strength results for co-consolidated samples . . . 34
4.3 Initial and final weld parameters . . . 36
4.4 Results of the disassembly experiments . . . 38

B.1 Influence of variations of $\sigma_{in-plane}$ for 20 s simulation time . . . 67
B.2 Influence of variations of c_p for 20 s simulation time . . . 68

C.1 T-test procedure . . . 70
C.2 T-test results for trends in the reference case lap shear strength . . . 71
C.3 T-test results for trends in the disassembly time . . . 71
C.4 T-test results for trends in the FLIR temperature at fracture . . . 72
C.5 T-test results for trends in the TC2 temperature at fracture . . . 72
C.6 T-test results for trends in the disassembly energy . . . 73

D.1 Sample names of fracture surfaces shown in report . . . 75
D.2 Sample names of cross-sections shown in report . . . 79

Nomenclature

Abbreviations

CC	Co-consolidated
CC w mesh	Co-consolidated joint with susceptor
CC wo mesh	Co-consolidated joint without susceptor
CFRP	Carbon fibre reinforced polymer
ED	Energy director
FLIR	Infrared camera
LSS	Lap shear strength
PPS	Polyphenylene sulfide
prop.	Property
RT	Room temperature
st. dev.	Standard deviation
TC	Thermocouple
TC1	Coil-facing thermocouple
TC2	Coil-opposing thermocouple
USW	Ultrasonically welded

Greek Symbols

ϵ	Emissivity
ϵ_0	Electric permittivity in vacuum
ϵ_r	Relative electrical permittivity
μ_0	Magnetic permeability in vacuum
μ_r	Relative magnetic permeability
ω	Angular frequency
ρ	Density
ρ_f	Density of the fibres
ρ_m	Density of the matrix
$\rho_{el.}$	Electrical resistivity
ρ_{pol}	Density of polymer
ρ_{st}	Density of steel
$\rho_{susceptor}$	Density of the susceptor

ρ_{tot} Total density of the laminate

σ Electrical conductivity

σ_m Electrical conductivity of the matrix

σ_p Electrical conductivity of polymer

σ_s Electrical conductivity of steel

σ_z Electrical conductivity through the thickness of the laminate

$\sigma_{eq,xy}$ Equivalent electrical conductivity in xy-plane (susceptor)

$\sigma_{eq,z}$ Equivalent electrical conductivity in z-direction (susceptor)

$\sigma_{in-plane}$ In-plane electrical conductivity

$\sigma_{L,f}$ Electrical conductivity of the fibres in longitudinal direction

$\sigma_{through-thickness}$ Through the thickness electrical conductivity

θ Angle of the fibres of a ply with respect to the 0°-direction

ε_0 Strain amplitude

Letters

$\dot{Q}_{avg}$ Average heat generation viscoelastic heating

A Magnetic vector potential

B Magnetic field

D Electric displacement field

E Electric field

H Magnetizing field (or magnetic field intensity)

$\mathbf{J_c}$ Conductive current density

J Current density

q Conductive heat flux

u Fluid velocity vector

A Cross-sectional area

A_i Cross-sectional area of the i^{th} layer

c_p Specific heat capacity at constant pressure

$c_{p,tot}$ Total heat capacity at constant pressure of the laminate

$c_{p,f}$ Heat capacity at constant pressure of the fibres

$c_{p,m}$ Heat capacity at constant pressure of the matrix

$c_{p,pol}$ Heat capacity at constant pressure for polymer

$c_{p,st}$ Heat capacity at constant pressure for steel

$c_{p,susceptor}$ Heat capacity at constant pressure of the susceptor

d Wire diameter susceptor

$d\mathbf{s}$	Curve element of a conductor
E"	Loss modulus
g	Geometrical parameter
h_i	height (thickness) of the ith ply
h_{tot}	Total height (thickness) of the laminate
I	Excitation current
j	Imaginary unit
k	Thermal conductivity
k_L	Longitudinal thermal conductivity in a composite ply
k_p	Thermal conductivity of polymer
k_s	Thermal conductivity of steel
k_T	Transverse thermal conductivity in a composite ply
k_z	Thermal conductivity through the thickness of the laminate
$k_{eq,xy}$	Equivalent thermal conductivity in xy-plane (susceptor)
$k_{eq,z}$	Equivalent thermal conductivity in z-direction (susceptor)
$k_{in-plane}$	In-plane thermal conductivity
$k_{L,f}$	Longitudinal thermal conductivity of the fibres
$k_{T,f}$	Transverse thermal conductivity of the fibres
$k_{through-thickness}$	Through the thickness thermal conductivity
$k_{x,\theta}$	Thermal conductivity of a ply with orientation θ in x-direction
$k_{x,i}$	Thermal conductivity of the ith ply of a laminate
$k_{x,tot}$	Total thermal conductivity of the laminate in x-direction
$k_{y,\theta}$	Thermal conductivity of a ply with orientation θ in y-direction
$k_{y,tot}$	Total thermal conductivity of the laminate in y-direction
l	Path length of heat or current
l_o	Overlap length of the joint
M	Thread count susceptor
Q	Heat of a heat source
Q_{ted}	Thermoelastic damping
r_{cp}	Distance to the coil (in bold: vector)
$R_{electrical}$	Electrical resistance
$R_{p,b}$	Resistance of polymer block at centre in z-direction (susceptor)
$R_{p,e}$	Resistance of polymer at edge in z-direction (susceptor)
R_{p1}	Resistance of polymer in layer 1 (susceptor)

R_{p2}	Resistance of polymer in layer 2 (susceptor)
$R_{s,c}$	Resistance of steel at corner in z-direction (susceptor)
$R_{s,e}$	Resistance of steel at edge in z-direction (susceptor)
R_{s1}	Resistance of steel wire in layer 1 (susceptor)
R_{s2}	Resistance of steel wire in layer 2 (susceptor)
$R_{thermal}$	Thermal resistance
R_{tot}	Total resistance
S	Wire length in unit cell susceptor
T	Temperature
t	Time
V	Voltage
v_f	Fibre volume fraction
v_m	Matrix volume fraction
v_{pol}	Volume fraction of polymer
v_{st}	Volume fraction of steel
V_s	Volume of steel
V_{tot}	Total volume
w_f	Weight fraction of the fibres
w_m	Weight fraction of the matrix
w_o	Overlap width of the joint
Z	Impedance
$f_{\text{LSS-RT}}$	Fraction of the lap shear strength at room temperature

1

Introduction

Disassembly of aircraft components allows for re-work during manufacturing, inspection and repair in service and recycling at the end-of-life. It is therefore vital in every stage of a component's lifetime. In metal aircraft structures, bolted or riveted joints were relatively easy to disassemble. With the advent of composite structures, however, joining methods became more complex and disassembly of these new types of joints is less straightforward.

For thermoset composites, adhesive bonding is preferred over mechanical fastening. Adhesive bonding does not require holes to be drilled in the composite, preventing severe stress concentrations in service and lowering the risk of delamination during manufacturing [3]. These adhesive joints are difficult to separate cleanly, unless they are specially designed for disassembly [23]. Moreover, the joining process of adhesive bonding is time-consuming and labour-intensive, due to the required surface preparation and long curing times of the adhesive.

Thermoplastic composites, on the other hand, allow for relatively rapid joining by fusion bonding. In fusion bonding, two parts are locally heated to processing temperature, after which they are pressed together. The polymer resin's molecular chains then cross the joint interface and entangle with polymer chains of the other adherend. Upon cooling, these entanglements form a relatively strong bond between the adherends. Since these bonds can be formed in a fraction of the time required for adhesive bonds, fusion bonding has attracted a lot of attention in recent years [16].

Despite the attention for these novel joining methods, research on disassembly of fusion bonded joints is virtually non-existent. Theoretically, fusion bonded joints could be reheated to soften the joint and lower the force required for disassembly. It would be useful to localize this heating into the joint interface, in order to limit the extent of the heat-affected zone. This heat affected zone could negatively affect the composite's properties. Induction heating is selected as the preferred heating mechanism, since it does not require contact with the heated part and only single-sided access to the joint is needed.

The aim of this research is to experimentally investigate disassembly of fusion bonded joints aided by induction heating. To this end, a literature study is first conducted to formulate proper research questions and hypotheses based on available knowledge. An experimental setup is designed to disassemble single lap joints by applying a fixed shear force while heating up the joint locally. The induction heating process is modelled using COMSOL Multiphysics® to facilitate the design of experiments. Disassembly experiments are carried out on co-consolidated samples with and without metal mesh susceptor and ultrasonically welded joints. The results are analysed and discussed, after which conclusions and recommendations for future research are formulated.

2

Literature review & research questions

Due to the scarcity of literature on disassembly of fusion bonded joints, disassembly methods of adhesive joints are researched for inspiration. From this review, re-heating of the joint to lower the required disassembly force seems one of the most viable options to facilitate disassembly. Therefore, three different heating mechanisms are investigated more closely: induction heating, resistance heating and microwave heating. Since disassembly will be investigated for both co-consolidated and ultrasonically welded joints, the process of ultrasonic welding is also addressed briefly. The insights gained during the literature review are used to identify the knowledge gap, after which research questions and hypotheses are formulated.

2.1. Literature review

2.1.1. Disassembly approaches for adhesive joints

Currently, adhesive joints are taken apart by mechanical cutting, sometimes assisted by thermal techniques or by solvent immersion to soften or degrade the adhesive [23]. For complex joints this can become very labour-intensive, and often residual adhesive remains on the adherends. Therefore, much research is done into so-called "disbond-on-demand" methods. These techniques incorporate features within the adhesive that lower the strength of the adhesive under certain conditions, thus simplifying disassembly.

For structural applications, a viable disbond-on-demand method seems to be the inclusion of expandable particles that react to heating [29]. The expansion of these particles upon application of heat causes internal stresses within the adhesive, which then cracks and breaks apart. Sometimes a small force is required to fully separate the adherends [23]. Unfortunately, this method does not prove to be viable for high-end thermoplastic composites used in aerospace. Even the most promising expandable particles currently in research expand at temperatures much lower than the processing temperature of these composites [33]. This would cause the particles to expand during processing, rendering them useless in service.

Another type of additives that can be included in the bond line for disbond-on-demand purposes are particles that heat up faster than the adherends and adhesive itself upon application of external heating. This heat can then degrade a thermoset adhesive or soften a thermoplastic adhesive to weaken the joint. Haq and Drzal [19] used carbon nanotubes in a thermoplastic adhesive to reheat the adhesive for disassembly. As carbon nanotubes allow to heat to sufficiently high temperatures for aerospace composites, this method could be used for disassembly of fusion bonded joints.

2.1.2. Heating mechanisms

Since lowering the joint strength by local re-heating seems to be a viable method for facilitating disassembly, different heating mechanisms are reviewed in literature. Induction heating, resistance heating and microwave heating will be assessed.

Induction heating
In induction heating, a coil carrying an alternating current is brought close to the sample to be heated. The alternating current creates an alternating magnetic field, which in turn induces a voltage difference within a conductive sample. This voltage difference causes eddy currents to flow. The voltage drop and associated electric current cause power dissipation in the form of heat within the sample [46].

Since carbon fibres are conductive, carbon fibre reinforced polymer (CFRP) can be heated by induction heating, provided that the fibres form closed loops within the composite. For carbon fibre fabric, heating can occur within a ply, while for unidirectional tapes different fibre orientations should be present in the laminate for induction heating to occur [43].

CFRP heats up due to three different heating mechanisms. Joule heating occurs along the fibres, while at the junctions heat is generated through dielectric heating and contact resistance heating. Yarlagadda et al. [43] developed a model comprising all three mechanisms and noted that fibre architecture, temperature and pressure influence which heating mechanism is dominant. Fibre Joule heating can be dominant when contact between fibres is abundant, such as in woven fabrics, or when laminates are heated and pressed together. Generally speaking, it was found that junction heating was dominant for most cases, with contact resistance heating being more prevalent.

A challenge in induction heating is the rapid decline of the magnetic field with distance from the coil. This causes the surface of a heated part to heat up preferentially. As the joint needs to be weakened primarily at the joint interface, this heating profile is rather inconvenient. For induction welding – a process that also requires heat to be concentrated at the joint interface – this is often solved by inserting a susceptor at the joint interface. This susceptor is more responsive to the magnetic field than the adherends and thus heats up more easily [15].

Since metals couple more easily with magnetic fields, they are an obvious candidate for usage as a susceptor material [6]. Metal particulates are mainly used in non-conductive materials, while metal meshes seem more promising for focusing heat in carbon fibre composites. However, the inclusion of a foreign material at the joint interface might cause stress concentrations reducing fatigue life [9], increase the weight of the composite and would complicate the final goal of recycling at the end-of-life. Therefore carbon fibre susceptors might be preferred. For a carbon fibre susceptor to be effective, it should have more fibre junctions to heat up preferentially. A higher fibre volume content also increases heating [5]. For laminates made of unidirectional tapes this might be complicated, as the fibre volume content of these laminates is already very high. Thin ply carbon fibre susceptors proved to be effective in recent research [8], but are rather complicated and expensive to manufacture. Carbon black particles [6] or carbon nanotubes [4] are sometimes also used as susceptor, but it is unclear whether these materials can concentrate heating in a carbon fibre composite with high fibre volume content.

In general, induction heating seems a very suitable candidate to use for disassembly purposes. It provides a fast yet controlled heating rate and offers the possibility to focus heating at the joint interface with susceptors. Moreover, it does not require contact and only single-sided access to the joint is necessary. These two factors simplify its applicability to disassembly in service.

Resistance heating
For resistance heating a current is injected directly in a resistive implant at the joint interface. The injected current causes Joule losses, resulting in local heating of the joint interface. Resistive implants used for resistance welding of aircraft components could be used for disassembly purposes [37]. These implants are either metal or carbon fibre meshes. Resistance heating is rather straightforward to control and flexible towards processable sizes [16].

For disassembly purposes, some complications arise. Electrical contact is required to both sides of the resistor to inject a current, which might be impractical in real-life applications. Moreover, if metal meshes are used these bare ends required for electrical contact might cause corrosion problems. For carbon fibre meshes, proper clamping is required to provide sufficient electrical contact [1]. If parts are difficult to access, clamping these ends might be not possible at all. Resistance heating seems therefore less practical for in-service disassembly than induction heating.

Microwave heating
Microwave heating happens in reaction to high frequency electromagnetic waves. A frequency of 2.45 GHz is usually used for the purpose of material processing [6]. For CFRP, heating primarily happens through eddy current heating and dielectric heating [44].

Focusing heat can happen by placing a highly absorbent material at the joint interface. Staicovici et al. [36] showed that if this material remains at the interface, it can be used for disassembly purposes. Haq and Drzal [19] used microwave heating to disassemble a CFRP composite with graphene nanoparticles at the joint interface. Therefore, microwave heating surely shows potential for disassembly purposes.

For real-life applications, however, some complications arise. When applying microwave heating, a shielded chamber should be used around the heated part to protect the environment against electromagnetic radiation. This may seriously hamper the usability of microwave heating for disassembly. As microwave heating is not available in the aerospace lab of TU Delft, it will not be used further in this research.

2.1.3. Ultrasonic welding
Ultrasonic welding is a fast, energy-efficient fusion bonding technique that can be automated relatively easily [13]. The technique is very popular for joining thermoplastics [16], and is currently investigated intensively for joining thermoplastic composites.

Ultrasonic welding uses high-frequency, low amplitude mechanical vibrations to heat up material. For thermoplastic composites, heating mainly occurs because of two mechanisms: surface friction between adherends and viscoelastic heating of the polymer resin. In the initial heating stages, surface friction is more important, while viscoelastic heating becomes dominant once the sample reaches the glass transition temperature of the polymer [13]. The mean heat generation of viscoelastic heating per unit of time is given by the following formula:

$$\dot{Q}_{avg} = \frac{\omega E'' \varepsilon_0^2}{2} \tag{2.1}$$

with ω the angular frequency of vibrations, E'' the loss modulus of the polymer and ε_0 the strain amplitude.

To focus heating at the joint interface, so called energy directors are used. Traditional energy directors are polymer protrusions (often triangular) moulded on top of the composite laminate. The protrusions deform more than the composite, locally increasing strain amplitude and thus increasing the viscoelastic heating (equation 2.1). Additionally, surface friction between these protrusions and the other adherend also enhance heating. Moulding these protrusions on top of the adherend requires and extra production step and complicates the design of joints, as the number, shape and distribution of the energy directors influence the heating. Therefore, these parameters should be optimized carefully for specific applications [41]. A simpler approach is to use flat neat resin films as energy directors. Owing to their lower stiffness, these polymer films deform more, thus increasing the strain amplitude and heat generation (equation 2.1). They also enable surface friction between the adherends' and energy directors' surfaces. It was shown by Palardy and Fernandez Villegas [32] that satisfactory welds could be produced for different sheet thicknesses.

Fernandez Villegas [12] established that the ultrasonic welding process with flat energy directors happens in five phases, based on the power-displacement curves obtained during welding (figure 2.1):

1. In the first phase, the energy director heats up without noticeable physical changes. The power increases steadily.
2. In the second phase, the energy director locally melts in so-called hot-spots, causing a drop in power while the displacement remains constant. The nucleation of these hot-spots is random and depends on surface friction.
3. The third phase is characterized by a rise in both power and displacement as the energy director is now fully molten and starts to flow.
4. At the start of the fourth phase, the adherends begin to melt, causing the power to level off in a plateau while the displacement keeps increasing. Energy director flow continues throughout the fourth phase.
5. In the last phase, melting adherends cause a power drop. Almost all resin is squeezed out in this phase.

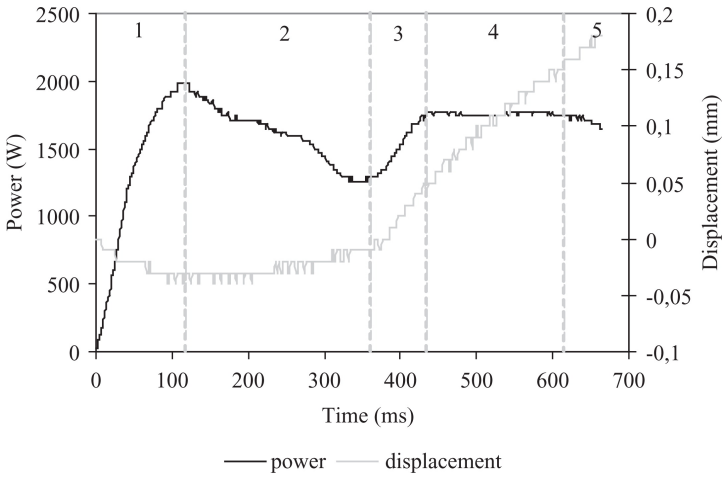


Figure 2.1: The five phases indicated on the power and displacement curves [12]

Moreover, Fernandez Villegas [11] showed that optimum welds are obtained if welding is stopped in the fourth phase using displacement control. In phase five, the melting of adherends causes increased fibre distortions, reducing joint strength. Stopping in phase three, on the other hand, causes incomplete welds. The research also showed that displacement control gives a more consistent weld quality than time-control, since the time to reach the fourth phase depends on the unpredictable surface friction. The power curve on the other hand changes if the setup is changed, as power is also dissipated in the clamping jig and sonotrode. Therefore, controlling the process based on the displacement curve is preferred. The five phases are also applicable for traditional energy directors, although the power and displacement curves are slightly different in this case [41].

To influence the welding process, different process parameters are important at different times in the process. During the vibration phase, welding force, vibration amplitude and vibration time are of prime importance. They primarily influence the rate of heat generation [13]. A combination of high weld force and high vibration amplitude increases the heating rate. Only increasing the amplitude might be less effective in increasing the heating rate, as cyclic loss of contact (known as hammering) limits the introduction of the vibrations within the sample [26]. Increasing the welding force decreases this hammering effect. The vibration time directly influences the energy input at the weld line. Longer vibration times lead to more energy input. Therefore the vibration time is directly linked to the weld quality [13].

In the consolidation phase, which starts just after vibrations stop, the main process parameters are consolidation force and consolidation time. Since cooling happens very quickly after vibrations stop, the consolidation time is usually set to a couple of seconds. For the consolidation force, a value equal to the welding force is chosen in practice.

2.1.4. Knowledge gap

From the literature review, it is clear that very little knowledge in the field of disassembly of fusion bonded thermoplastic composite joints is available. Possibilities to weaken the joint by heating prior to disassembly are often mentioned [3, 16, 37, 44], but as of yet not thoroughly researched. As disassembly plays an important role throughout the lifetime of aircraft components, exploratory research in this field could be valuable for future use.

As ultrasonic welding is a promising fusion bonding technique, it would also be interesting to try disassembly of ultrasonically welded thermoplastic composites. However, it might be necessary to place inserts at the joint interface to make disassembly more feasible. These inserts would influence the stiffness of the weld stack at the joint interface, and therefore greatly influence the ultrasonic welding process. The exact influence is as of yet unknown and remains to be researched.

2.2. Research questions and hypotheses

Based on the literature review, lowering the joint strength by locally heating the joint with induction heating seems a viable method to facilitate disassembly of fusion bonded joints. Moreover, a susceptor could be used to concentrate the heating at the interface. Metal meshes seem to provide the best performance regarding heat focusing. Additionally, investigating disassembly of ultrasonically welded joints would be interesting due to the promising joining characteristics of ultrasonic welding. All of these considerations allow to formulate research questions, hypotheses and a research methodology.

Research questions

The identified knowledge gap and the decisions made based on the literature review culminate in the following main research question:

How can induction heating be used to lower the required force for disassembly of fusion bonded thermoplastic composite joints, while minimizing damage to the joined parts inflicted during disassembly?

To help solve this question, multiple sub-questions can be formulated:

1. What is the effect of a metal mesh susceptor on the disassembly process and disassembly-related damage?
   (a) How effectively can the susceptor focus heating?
   (b) How are the disassembly characteristics, such as time and temperature, affected by the presence of the susceptor when applying a fixed excitation current and disassembly force?
   (c) What is the effect of the susceptor on the type and extent of damage?
2. How does the type of fusion bonding process (ultrasonic welding versus co-consolidation) affect the disassembly process and disassembly-related damage?
   (a) How are the disassembly characteristics, such as time and temperature, affected by the type of fusion bonded joint when applying a fixed excitation current and disassembly force?
   (b) What is the effect of the type of fusion bonded joint on the type and extent of damage?

Hypotheses

Hypotheses are formulated based on the studied literature. For consistency, the hypotheses will be formulated per sub-question of the main research question:

1. The main goal of the susceptor is to concentrate heating at the interface, locally weakening the joint. Compared to susceptorless joints, disassembly of samples with susceptor could therefore be faster and/or require a less high temperature at the sample's surface. Possibly a lower excitation current can be chosen as well. The heat concentration could also limit the extent of damage for samples with susceptor as compared to susceptorless samples.
2. In ultrasonic welding, an energy director in the form of a pure polymer film is used to facilitate the joining process. This could negatively affect heating during disassembly, as this film prevents current from flowing through the joint interface. The insulating layer might also decrease the magnitude of current in the coil-opposing adherend, which could limit the thermal damage locally. However, as ultrasonic welding of small coupons already inflicts some damage at the edges of the sample, this might be difficult to detect.

Summary of the methodology

The main research question addresses disassembly of fusion bonded joints in general, and will be answered by investigating both co-consolidated and ultrasonically welded joints. Co-consolidation is more straightforward than ultrasonic welding, as less variables and process parameters are of an influence during manufacturing and inclusion of a susceptor is rather easy. Therefore, the research will start investigating co-consolidated joints with and without metal mesh susceptor. Prior to measurements, a model will be built. This model should facilitate experimental design and help to solve the research questions that are difficult to solve experimentally, such as the effectiveness of heat focusing. After modelling, the disassembly process and damage inflicted during disassembly of co-consolidated joints will be evaluated experimentally.

Subsequently, disassembly of ultrasonically welded joints will be investigated. Since including a metal mesh susceptor would severely influence the ultrasonic welding process and optimizing this process can be a master thesis in itself, it is chosen to only test disassembly of susceptorless ultrasonically welded samples. The results of these tests will then be compared with the results of susceptorless co-consolidated samples to answer the second sub-question.

The full methodology is described in depth in chapter 3.

3

Method

This chapter details the applied research methodology. First, the modelling of induction heating is addressed from the setup of the model to the validation and simulations. Subsequently, the experimental part of the research is described. The sample preparation procedure, ultrasonic welding and testing of a reference case are described first. Then, the experimental setup, its calibration and the actual disassembly experiments are reported. The chapter concludes with outlining the approach for microscopic investigation. The results of this methodology will be described in chapter 4.

3.1. Model

Prior to experiments involving induction heating, the induction heating process was modelled using COMSOL Multiphysics®. With these simulations, a better idea of the process parameters required to heat the sample to the necessary temperatures was gained. After validation, the model could also be useful to investigate the difference in heating between samples with and without susceptor. Essential to a good prediction of the heating characteristics is the model setup. The first part of the setup is modelling of the material properties. The setup is completed with applying a mesh of finite elements and inserting induction heating physics in COMSOL. After setting up the model, a sensitivity analysis, model validation and the final simulations were performed.

3.1.1. Susceptor material model

A plain weave metal mesh was used as susceptor. For modelling purposes, a couple of assumptions were made:

- The gaps within the mesh are all perfectly filled with PEEK polymer after fusion bonding.
- The thickness of the susceptor layer equals the thickness of the metal mesh, i.e. there is no additional PEEK polymer layer at the top and bottom of the mesh.

This allows for the susceptor to be modelled as a thin block of homogenized material. The material properties were calculated based on the approaches of Xu and Wirtz [42] and Zhao et al. [45].

The required properties were calculated in a unit cell of the susceptor material, as shown in figure 3.1. In this study a square mesh was used, for which $M_x = M_y$ and $d_x = d_y$. The arc length of arc AB is given by the following equation [45]:

$$S = |AB| = \frac{1}{M}\left(\frac{Md}{2} + \frac{1}{2Md}\right)\arcsin\left(\frac{1}{\frac{Md}{2} + \frac{1}{2Md}}\right) \tag{3.1}$$

The geometric parameters of the mesh used in this study are given in table 3.1. Before starting the calculation of material properties, the unit cell geometry was transformed to a simpler geometry.

Simplified geometry

To set up the material model, the geometry of the metal mesh was simplified to a layered geometry with wires with a rectangular cross-section. The dimensions of the simplified geometry were chosen such that the

Table 3.1: Geometric parameters of the metal mesh

Property	Value	Unit
Wire diameter (d)	200	µm
Mesh opening	904	µm
$\frac{1}{M_x} = \frac{1}{M_y} = \frac{1}{M}$	1104	µm
S	1127	µm

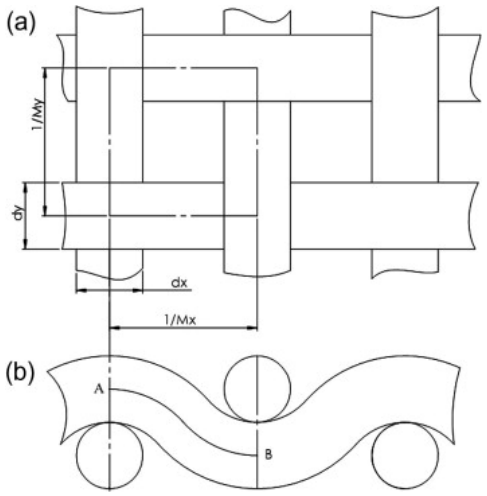


Figure 3.1: Unit cell of the susceptor, (a) top view (b) side view [45]

rectangular wires have the same cross-sectional area ($\frac{\pi d^2}{8}$) and length (S) as the wires in the original unit cell (figure 3.1). The transformed unit cell is depicted in figure 3.2.

Thermal and electrical conductivity
To estimate the thermal and electrical conductivity, equivalent resistive networks were drawn from the transformed unit cell of figure 3.2. From these networks and the definition of thermal and electrical resistance, the thermal and electrical conductivity can be calculated. The definition of thermal resistance states:

$$R_{thermal} = \frac{l}{kA} \tag{3.2}$$

with l the length the heat has to travel, k the thermal conductivity and A the cross-sectional area of the path the heat follows. For electrical resistance, a similar definition applies:

$$R_{electrical} = \frac{\rho_{el.} l}{A} = \frac{l}{\sigma A} \tag{3.3}$$

where l and A have the same meaning as before, while $\rho_{el.}$ represents the electrical resisitivity and σ the electrical conductivity. Equations 3.2 and 3.3 were solved for k and σ, respectively, to find the thermal and electrical conductivity of the susceptor material.

Two equivalent resistive networks were drawn: one for the in-plane properties and one for the through-the-thickness properties. The equations will be given for the thermal conductivity k. For the electrical conductivity, it suffices to replace k with σ.

The resistive network for the in-plane conductivity is shown in figure 3.3. In this network, "p" stands for polymer and "s" for steel. In the bottom layer, the heat entering the model first encounters a steel wire (Rs1), then travels through a polymer region (Rp1) and finally encounters the second wire (Rs1). This is equivalent to three resistors in series. The bottom layer is connected in parallel to the top layer, in which the heat can travel

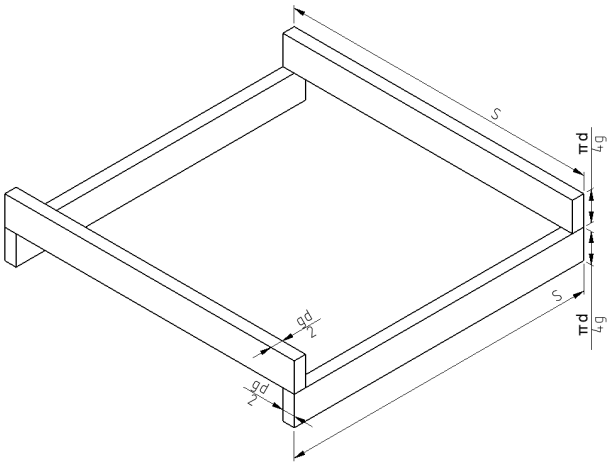


Figure 3.2: Transformed unit cell for mesh model, based on Xu and Wirtz [42]

through the wires (Rs2) or through the polymer (Rp2) in parallel paths. From this schematic the equation of total thermal resistance follows: [42]:

$$\frac{1}{R_{tot}} = \frac{1}{2R_{s1} + R_{p1}} + \frac{2}{R_{s2}} + \frac{1}{R_{p2}} = k_{eq,xy}\frac{\pi d}{2g} \tag{3.4}$$

The equations for R_{s1}, R_{p2}, R_{s2} and R_{p2} can be derived from the simplified geometry (figure 3.2) and the definition of thermal resistance (equation 3.2). The detailed derivation is given in Appendix A.

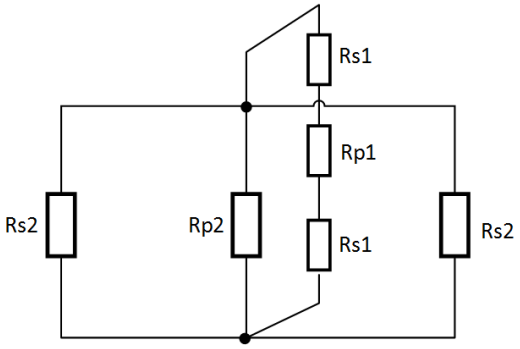


Figure 3.3: Equivalent resistive network in the horizontal plane [42], indices: s = steel, p = PEEK, 1 = bottom layer and 2 = top layer of figure 3.2

From the conservation of volume between the two unit cell representations, it follows that $g = \frac{\pi}{4}$. Solving equation 3.4 for $k_{eq,xy}$ delivers the final result for the in-plane thermal conductivity of the susceptor.

Finding the electrical conductivity requires little extra effort. It suffices to replace the thermal conductivity of steel and polymer with the respective electrical conductivity. Solving for $\sigma_{eq,xy}$ instead of $k_{eq,xy}$ then delivers the final result for the in-plane electrical conductivity of the susceptor. The input parameters of the equations as well as the final results are given in table 3.2, while geometrical parameters of the mesh are given in table 3.1.

To find the thermal and electrical conductivity through the thickness, a similar approach was taken. The model in figure 3.2 was now divided into 9 pieces: 4 corners in which the steel wire spans the whole thickness ($R_{s,c}$), the 4 edges of which half is steel wire ($R_{s,e}$) and half is polymer ($R_{p,e}$), and a polymer block in the middle ($R_{p,b}$). At the edges, the polymer and steel resistances are connected in series. The corners, edges and polymer block in the middle are connected in parallel. This resulted in an equivalent resistive model, shown in figure 3.4.

From figures 3.2 and 3.4 equations for the total thermal and electrical resistances were derived. The equations will be described for thermal conductivity. For electrical conductivity, it suffices to replace k with σ. The equivalent resistive network and the definition of thermal resistance give the following equation:

$$\frac{1}{R_{tot}} = \frac{4}{R_{s,e} + R_{p,e}} + \frac{4}{R_{s,c}} + \frac{1}{R_{p,b}} = k_{eq,z} \frac{2gS^2}{\pi d} \tag{3.5}$$

Again, an elaborate derivation of the equations for $R_{s,e}$, $R_{p,e}$, $R_{s,c}$ and $R_{p,b}$ is given in Appendix A. Solving equation 3.5 for $k_{eq,z}$ (or $\sigma_{eq,z}$) delivers the final result for the through-the-thickness material properties of the susceptor. The input parameters and results of the calculation are again given in table 3.2.

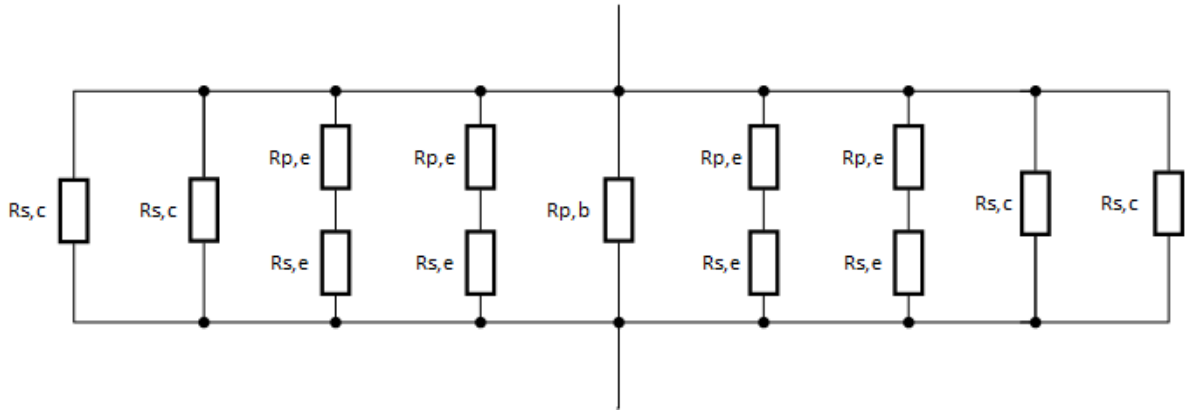


Figure 3.4: Equivalent resistive model through the thickness. Indices: s = steel, p = PEEK, c = corner, e = edge, b = block at the centre of the simplified geometry (figure 3.2)

Specific heat capacity
The rule of mixtures was used to estimate the specific heat capacity (at constant pressure) of the susceptor:

$$c_{p,susceptor} = v_{st} c_{p,st} + v_{pol} c_{p,pol} \tag{3.6}$$

where v_{st} and v_{pol} are the volume fractions of steel and polymer, respectively, while $c_{p,st}$ and $c_{p,pol}$ are the specific heat capacity at constant pressure of steel and polymer, respectively. The input parameters and result can be found in table 3.2. The volume fractions were calculated using the geometric parameters of table 3.1. This calculation is given in Appendix A.

Density
The rule of mixtures was also used to estimate the density:

$$\rho_{susceptor} = v_{st} \rho_{st} + v_{pol} \rho_{pol} \tag{3.7}$$

with values of v_{st} and v_{pol} taken from the calculations in Appendix A. The input densities and resulting density of the susceptor are given in table 3.2.

Relative magnetic permeability, relative electric permittivity and emissivity
The value of relative magnetic permeability for a similar susceptor in an induction heating setup was taken from literature [15]: $\mu_r = 1$.

The relative electric permittivity proved more difficult to find. For stainless steel, the permittivity is infinite, while for PEEK the value is around 3. According to Moser [31], the electric permittivity is of less importance in induction heating problems. Therefore, a value equal to the electric permittivity of composite laminates was taken ($\epsilon_r = 3.7$, [10, 31]). To check the sensitivity of the model to this parameter, it was set to 37, 370 and 37000. This resulted in less than 1% difference in the temperature at probe points in the model in all cases.

The emissivity for radiation heating was also taken equal to the emissivity of the laminate ($\epsilon = 0.95$, [10]). Since the susceptor is only 400 µm thick and is sandwiched between the laminate adherends, very little surface area of the susceptor is available for radiative heat transfer. Therefore, the emissivity of these surfaces barely influences the result of the heating simulation and can be taken equal to the rest of the material.

Material properties
The material data required for the calculations as well as the final results for the required material properties are given in table 3.2. Data for AISI 304 steel was taken from MatWeb [28] and cross-checked [21, 30]. For PEEK, the values were taken from the technical data sheet of Victrex PEEK 450G [40].

Table 3.2: Input material properties and result for susceptor properties

Input parameters

Material property	Symbol	Value	Unit
thermal conductivity steel	k_s	16.2	W/mK
electrical conductivity steel	σ_s	1.3889e6	S/m
specific heat capacity steel	$c_{p,st}$	500	J/kgK
density steel	ρ_{st}	8000	kg/m^3
thermal conductivity PEEK	k_p	0.29	W/mK
electrical conductivity PEEK	σ_p	1e-15	S/m
specific heat capacity PEEK	$c_{p,pol}$	2200	J/kgK
density PEEK	ρ_{pol}	1300	kg/m^3

Results

Material property	Symbol	Value	Unit
thermal conductivity, in-plane	$k_{eq,xy}$	1.42	W/mK
thermal conductivity, through thickness	$k_{eq,z}$	0.75	W/mK
electrical conductivity, in-plane	$\sigma_{eq,xy}$	97654.4	S/m
electrical conductivity, through thickness	$\sigma_{eq,z}$	26933.6	S/m
specific heat capacity	$c_{p,susceptor}$	1963.3	J/kgK
density	$\rho_{susceptor}$	2233	kg/m^3
relative permeability	μ_r	1	-
relative permittivity	ϵ_r	3.7	-
emissivity	ϵ	0.95	-

3.1.2. Laminate material model
The thermal and electrical in-plane conductivity of the laminates were calculated following a method described in literature [22, 27]. Other properties were calculated with the rule of mixtures, found in technical data sheets of the material or found in scientific literature. The laminate used is a $[0/-45/90/-45/45/-45]_s$ laminate of Toray Cetex® TC1200 Standard modulus unidirectional tapes.

Thermal and electrical conductivity
The in-plane conductivity was first calculated on ply level, using the rule of mixtures:

$$k_L = v_f k_{L,f} + v_m k_m \tag{3.8}$$

$$\frac{1}{k_T} = \frac{v_f}{k_{T,f}} + \frac{v_m}{k_m} \tag{3.9}$$

In the above equations, k_L and k_T are the thermal conductivity of the ply in fibre direction and transverse to fibre direction, $k_{L,f}$ and $k_{T,f}$ the thermal conductivity of the fibres in longitudinal and transverse direction, and k_m the thermal conductivity of the polymer matrix. The volume fractions of fibre and polymer matrix material in the composite are represented by v_f and v_m, respectively. Replacing the thermal conductivity k with electrical conductivity σ gives the in-plane ply electrical conductivity.

In a composite lay-up, laminates are made out of plies with different orientations. Therefore, the contribution of each ply and its respective orientation to the global conductivity needs to be calculated. To this end, the following transformation matrix was used [27]:

$$\begin{bmatrix} k_{x,\theta} \\ k_{y,\theta} \end{bmatrix} = \begin{bmatrix} \cos\theta & \sin\theta \\ -\sin\theta & \cos\theta \end{bmatrix} \begin{bmatrix} k_L & 0 \\ 0 & k_T \end{bmatrix} \begin{bmatrix} \cos\theta & -\sin\theta \\ \sin\theta & \cos\theta \end{bmatrix} \tag{3.10}$$

Assuming that each ply is a thermal resistance and all plies are connected in parallel, the following equation can be derived for the total thermal conductivity of the laminate:

$$\frac{1}{R_{tot}} = \sum_{i=1}^{n} \frac{1}{R_i} \Leftrightarrow k_{x,tot} \frac{A_{tot}}{l} = \sum_{i=1}^{n} \left(k_{x,i} \frac{A_i}{l} \right) \Leftrightarrow k_{x,tot} = \sum_{i=1}^{n} \left(k_{x,i} \frac{h_i}{h_{tot}} \right) \tag{3.11}$$

With h_i and h_{tot} the thickness of the ith ply and the total thickness of the laminate, respectively. For $k_{y,tot}$ a similar approach was taken. The same reasoning is also valid for electrical conductivity. Hence, replacing all k with the corresponding σ delivers the result for the total in-plane electrical conductivity.

The out-of plane thermal and electrical conductivity were assumed to be similar to the transverse conductivity in a single ply. The value for transverse thermal conductivity of a ply (k_T) was taken from the work of Holmes and Gillespie [22] and recalculated for the fibre and matrix volume fractions used in this study. For electrical conductivity, a low value of 10 S/m is set for ease of convergence of the model [15]. The exact values for material properties of the laminate adherends are given in table 3.3.

Specific heat capacity
The specific heat capacity was calculated with the rule of mixtures:

$$c_{p,tot} = v_f c_{p,f} + v_m c_{p,m} \tag{3.12}$$

with $c_{p,f}$ the specific heat capacity of the fibres and $c_{p,m}$ the specific heat capacity of the polymer matrix. The volume fractions v_f and v_m were calculated with the weight fractions and density given in the technical datasheets of the materials [20, 40]. The results and input parameters are shown in table 3.3.

Density, relative magnetic permeability, relative electric permittivity and emissivity
The density was taken from the technical data sheet of the composite material used [39]. All other values were taken from the work of Duhovic et al. [10] and Moser [31]. The properties are given in table 3.3.

Table 3.3: Input material properties and result for laminate properties [10, 15, 20, 31, 39, 40]

Input parameters

Material property	Symbol	Value	Unit
thermal conductivity fibre, longitudinal	$k_{L,f}$	6.83	W/mK
thermal conductivity fibre, transverse	$k_{T,f}$	0.372	W/mK
electrical conductivity fibre, longitudinal	$\sigma_{L,f}$	58824	S/m
specific heat capacity fibre	$c_{p,f}$	1129.7	J/kgK
density fibre	ρ_f	1790	kg/m^3
weight fraction fibre	w_f	0.66	-
thermal conductivity matrix (PEEK)	k_m	0.29	W/mK
electrical conductivity matrix (PEEK)	σ_m	1e-15	S/m
specific heat capacity matrix (PEEK)	$c_{p,m}$	2200	J/kgK
density matrix (PEEK)	ρ_m	1300	kg/m^3
weight fraction matrix (PEEK)	w_m	0.36	-

Results

Material property	Symbol	Value	Unit
thermal conductivity, x and y direction	$k_{x,tot}$ and $k_{y,tot}$	2.224	W/mK
thermal conductivity, through-thickness	k_z	0.332	W/mK
electrical conductivity, x and y direction	$\sigma_{x,tot}$ and $\sigma_{y,tot}$	17206.8	S/m
electrical conductivity, through thickness	σ_z	10	S/m
specific heat capacity	$c_{p,tot}$	1573.8	J/kgK
density	ρ_{tot}	1590	kg/m^3
relative permeability	μ_r	1	-
relative permittivity	ϵ_r	3.7	-
emissivity	ϵ	0.95	-

3.1.3. Model geometry and meshing

The model geometry was drawn directly in the COMSOL Multiphysics® software and is shown in figure 3.5. The sample without susceptor consists out of two plates with a width of 25.4 mm and a thickness of 1.5 mm. The length of the sample was set to 50 mm, which is much smaller than the real length of the samples. However, the temperature at this distance from the coil barely changed during the simulation. Shortening the samples thus helps in saving computation time, as less finite elements are needed for this model. The overlap length of the two adherends was set to 12.7 mm. A custom material was inserted in the software, with properties as mentioned in table 3.3. The emissivity was added in a separate 'material' with as only property the surface emissivity. This material was applied to all surfaces exposed to air. Within the sample, 9 probe points were set up in rows of 3: one row at the top of the sample close to the edge, one row in the middle of the sample and one row at the lower edge. In each row, there is one probe point at the coil-facing side, one in the centre of the material at the joint interface and one at the coil-opposing side. Within these probe points, the temperature will be calculated for each time step the model takes.

The coil was measured by hand and modelled as a solid copper wire with a diameter of 5 mm. For initial trials, the coil geometry was reduced to a copper wire along the heart-line of the full coil to save computation time.

The susceptor was modelled as a 400 µm thick plate with a length of 12.7 mm and a width of 25.4 mm, sandwiched in between the two adherends. Again, a custom material was added in the software, with properties according to table 3.2. The surface emissivity property was also added to the surfaces of the susceptor that are exposed to air.

Around the setup, an air domain was modelled. The dimensions of the air domain were chosen to be 20 times the coil diameter. As the intensity of the magnetic field decreases inversely proportionally to the square of the distance from coil, it was assumed that this distance is sufficiently large, such that boundary conditions applied to this air domain do not influence the magnetic field at the joint.

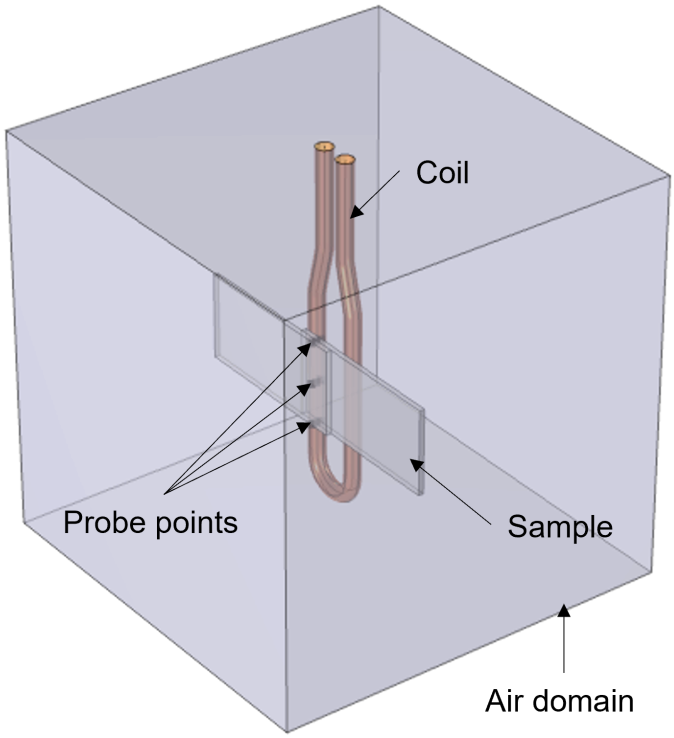


Figure 3.5: Model geometry

A free tetrahedral mesh was applied to all domains. For the sample without susceptor, standard settings were used: a normal-sized, physics-controlled mesh. For the sample with susceptor, the normal size caused

meshing errors within the susceptor. Therefore, a fine mesh was applied to the susceptor, while a normal-sized mesh was applied to other domains. The software automatically provides a transition between the meshes of different size to ensure continuity. Trials were also done with automatic mesh refinement, but this severely increased computation time while giving similar results to the non-refined mesh.

3.1.4. Model physics

COMSOL Multiphysics® has a built-in eletromagnetic heating module, that couples two different physics modules: the magnetic fields interface and the heat transfer in solids interface. In both modules, certain boundary conditions need to be set, after which the coupling between the modules needs to be specified by defining a study. The choices made in modelling the physics will be explained in subsequent paragraphs.

Magnetic fields interface

In the magnetic fields interface, the magnetic field, induced current and subsequent magnetic and electric losses are calculated. To this end, Ampère's law is applied to all domains except for the coil, where a coil domain function is applied. The equations solved in these domains are further detailed in Appendix A.

The coil domain function applied to the coil allows for voltage, current or power excitation. Within the coil the constitutive relations detailed in Appendix A are solved. A "line current" was applied to the line coil, which was used for preliminary simulations. For the full coil geometry however, current excitation failed to converge. Therefore, the current excitation (I) needed to be transformed to a voltage excitation by multiplication with the impedance. Since excitation values given in COMSOL always represent the modulus of a complex number, and the impedance of the coil (Z) is constant for a constant frequency, the corresponding voltage excitation (V) is found as follows:

$$|V| = |Z||I| \tag{3.13}$$

Lastly, a magnetic insulation boundary condition was placed on the edges of the air domain and the initial values of the magnetic vector potential were set to 0 Wb/m.

Heat transfer in solids interface

The heat transfer module was only applied to the heated sample. The coil used in experiments is water-cooled and therefore assumed to be on room temperature throughout the simulation. The equations solved in the sample are again explained in detail in Appendix A.

At both ends of the sample, a thermal insulator boundary condition was applied. To all other vertical edges, the built-in natural convection boundary condition along a vertical wall was applied. To the horizontal edges the corresponding convection boundary conditions were applied (upside and downside). To all edges exposed to air (except at the sample's ends), a surface-to-ambient radiation was applied. At the start of the simulation all domains were set to room temperature (25°C).

Electromagnetic heating (multiphysics)

Since it was assumed that all material properties were independent of temperature, it was not necessary to recalculate the magnetic fields every single step. The excited eddy currents remained the same throughout the simulation. Therefore, a frequency-transient, one-way electromagnetic heating study was selected for the model. The frequency was chosen in the range of 358 to 374 kHz, depending on the coil current. This was done to recreate the conditions of the disassembly experiments. Heating calculations were performed for different times, depending on the experimental data gathered for a specific excitation current. Before the frequency-transient calculations, a coil geometry analysis was performed.

3.1.5. Sensitivity analysis

All material values were either calculated by using approximations or taken from literature, and assumed independent of temperature. During actual experiments however, material properties vary with temperature and may deviate from the results of the calculations. Therefore, it is important to know how small deviations in the material properties influence the heating behaviour in the model. Finding the most influential properties could also help to decide which parameters to change, should the model not correspond to reality.

All relevant material properties were varied by ±10%. The laminate properties were varied in the model without susceptor. It was assumed that a change in the laminate properties would have a similar outcome in the

model with susceptor. The influence of changes in the susceptor material properties was tested within the full model, i.e. with the susceptor sandwiched between two laminate adherends.

3.1.6. Model validation

Data from disassembly experiments was used for model validation. The model was tweaked to fit the data at an excitation current of 300.3 A. For validation, the adjusted model was then used to predict the temperature evolution for the other excitation currents used in disassembly experiments (see table 3.5). The simulated results and experimentally measured temperature evolution curves were plotted together for comparison. The results of this process are shown in chapter 4.

3.1.7. Simulations

Different scenarios were simulated in COMSOL. All simulations were done for a short heating period of 11 s at a frequency between 359 and 374 kHz. The sensitivity of heating with changing position of the sample with respect to the coil was evaluated. The influence of the coupling distance between the sample and the coil was investigated by varying this distance from 2 mm to 4 mm. The influence of eccentricity of the sample with respect to the coil was also investigated by varying the position of the centrepoint of the joint with ± 2 mm and ± 4 mm. Additionally, heating profiles of the coil-facing surface and through the thickness of the sample were evaluated.

3.2. Experimental

Disassembly of fusion bonded joints was tested experimentally. In preparation for the actual disassembly experiments of co-consolidated joints, samples with and without susceptor were manufactured. A reference case using a temperature chamber instead of induction heating was tested to establish possible disassembly forces for the experimental setup and for comparison with disassembly results. Other samples were welded ultrasonically and tested until a satisfactory weld strength was obtained. Then, a disassembly setup was designed and its sensors were calibrated. The actual disassembly experiments were carried out for different loads and excitation currents on the two types of co-consolidated samples and on ultrasonically welded specimens. After fracture, the samples' surfaces and cross-sections were investigated microscopically.

3.2.1. Sample preparation

All samples were made from Toray Cetex® TC1200 carbon fibre/PEEK standard modulus unidirectional tape, laid up in a $[0/-45/90/-45/45/-45]_s$ configuration of 305 mm by 305 mm. During the layup process, layers were fixed on top of each other with a Rinco handheld ultrasonic welder.

To produce co-consolidated plates, two unconsolidated laminates were stacked on top of each other with 0.01 mm thick kapton films in between. The kapton films were coated three times on both sides with Marbocote CE227 release agent, to prevent bonding of the two plates. A 12.7 mm wide gap was left between the two kapton films, to create a co-consolidated joint with the correct overlap length. Figure 3.6 shows the placement of the kapton films as well as the steel mesh for samples with susceptor. Aluminium foil was wrapped around the stack's edges to catch any resin flowing out of the laminate layers.

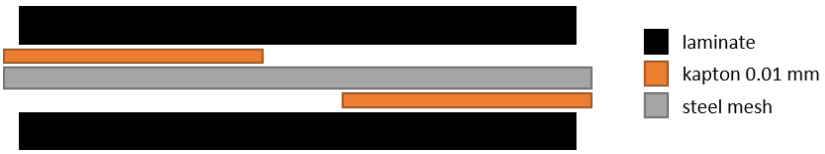


Figure 3.6: Stacked co-consolidated plates with susceptor

Steel mould plates, again coated with Marbocote CE227 release agent, were used together with graphite plates to create a mould as shown in figure 3.7. The graphite plates served to distribute the temperature more uniformly throughout the press stack, creating plates of uniform quality. Kapton films of 0.1 mm thick, coated with Marbocote CE227, were put between the mould and press plates to catch any leaking resin and protect the press plates from damage.

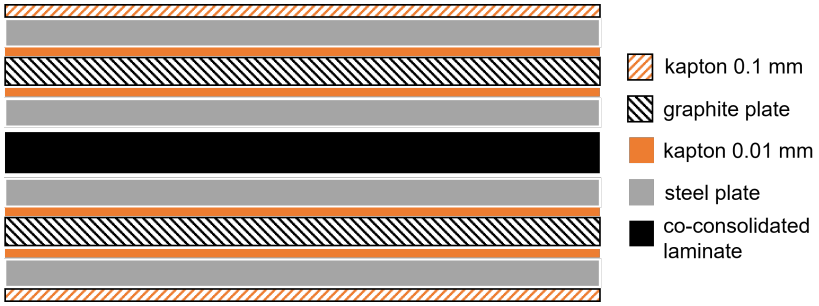
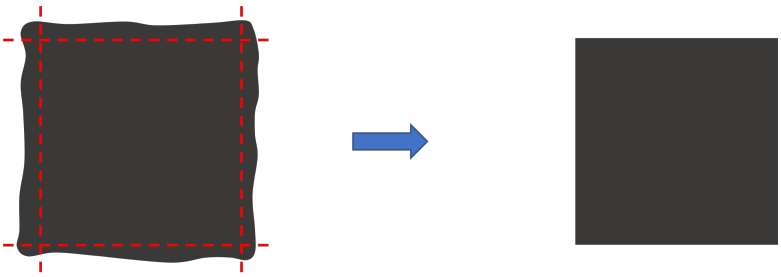


Figure 3.7: Mould lay-out

A Joos 1000 kN hydraulic press was used to consolidate the laminates. A heating rate of 5°C per minute was used to reach a temperature of 385°C. During heating, a pressure of 4 bar was applied. After reaching 385°C, the pressure was kept at 4 bar for 30 minutes, after which it was increased to 10 bar in a time frame of 30 seconds. After 45 minutes dwell time at 10 bar and 385°C, the cooling was started at a rate of 5°C per minute. The pressure was maintained until the press stack was fully cooled down.

After consolidation, the edges of the resulting plate were trimmed using a Carat P-3508 cutting machine with a diamond-coated saw blade (figure 3.8a). Subsequently the excess unbonded parts of the plates were cut away from the joint using a Proth cutting and grinding machine, equipped with a diamond-coated saw blade (figure 3.8b). In the case of susceptorless plates, samples for ultrasonic welding could be cut from these excess parts to minimize waste. For co-consolidated plates with susceptor, the metal mesh left a pattern of PEEK resin on the excess plates' surface, which made them unusable for ultrasonic welding. Both the co-consolidated and reusable excess plates were cut in 25.4 mm wide strips (figure 3.8c).



(a) Trimming the edges along the red dashed lines (top view)



(b) Cutting away excess plate parts along red dashed lines (side view). The orange rectangles represent the 0.01 mm thick kapton film.



(c) Cutting remaining plate into final samples (top view)

Figure 3.8: Cutting procedure for a co-consolidated plate

Aluminium tabs were applied prior to testing. For the reference case, these tabs were necessary to prevent

slippage between the specimen and the grips of a tensile test bench. For disassembly experiments, holes of 12.5 mm diameter were drilled with their centrepoint 15 mm from the sample's edge to allow for mechanical locking of the sample in the test set-up. Here, the aluminium tabs served as a reinforcement of the specimen's ends. The samples' surfaces were sanded, cleaned with isopropyl alcohol and UV-treated for 5 minutes to enhance bonding. The tabs measured 60 mm by 25.4 mm with a thickness of 1 mm for co-consolidated samples and 40 mm by 25.4 mm with a thickness of 3 mm for ultrasonically welded samples. Prior to bonding they were cleaned, sand-blasted and cleaned again with isopropyl alcohol, after which they were glued to the samples' ends with either Scotch-weld 9293 or Loctite EA9394 two-component glue. For the reference case tests, it was necessary to use Loctite EA9394 due to the high temperatures the glue had to sustain within the temperature chamber. For other tests, high temperatures only occurred at the joint itself, far away from the tabs. Therefore, a lower-end glue could be used. To ensure a proper bond line thickness, 3 to 4 wt.% glass beads of 150-250 µm diameter were mixed into the glue. The glue was left to cure for a week. For the reference case however, this curing time could be cut short since samples were pre-heated in a temperature chamber before testing. This gave the glue the chance to cure faster at higher temperatures.

3.2.2. Ultrasonic welding

Samples were welded using a Hermann HiQ Dialog 20 kHz ultrasonic welder. A titanium sonotrode with a rectangular contact area of 30 mm by 16 mm was used (figure 3.9). Welding was performed applying a displacement controlled setup, i.e. the vibration of the sonotrode was stopped when a preset vertical displacement was reached. To clamp the samples, a custom-made welding jig that prevents shifting and bending of the samples during welding was used (figure 3.9). A 0.25 mm thick PEEK film was used as energy director for all samples.

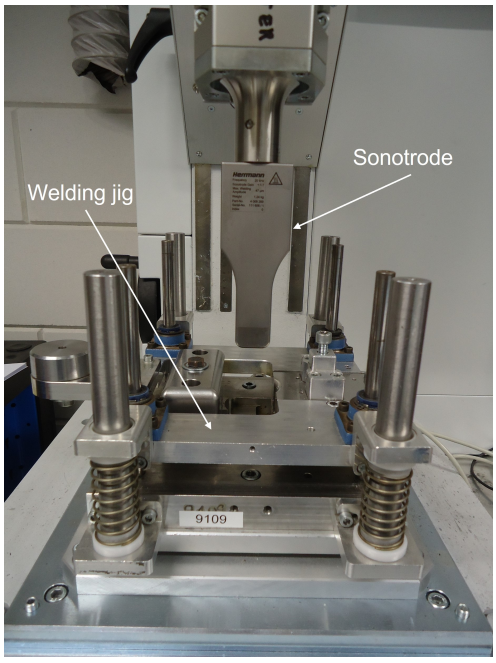


Figure 3.9: Sonotrode and custom-made welding jig

After welding, samples were tested using a Zwick 250 kN universal testing machine with hydraulic clamps. A crosshead displacement rate of 1 mm per minute was applied (based on [2]). The lap-shear strength (LSS) was calculated with the following formula:

$$LSS = \frac{F_{max}}{w_o \cdot l_o} \tag{3.14}$$

With F_{max} the maximum recorded force before fracture, w_o the overlap width and l_o the overlap length of the joint. Due to fibre distortion and squeeze-out, the overlap length and width were difficult to measure. It was assumed that the jig provided an overlap length of 12.7 mm. The width was measured for both adherends at

the location without squeeze-out closest to the joint, as shown in figure 3.10. The overlap width was defined as the smallest width measured in this fashion.

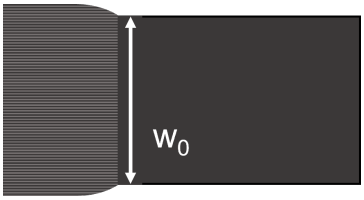


Figure 3.10: Schematic of how overlap width was measured for ultrasonically welded samples

After multiple welding iterations, the welding parameters listed in table 3.4 resulted in satisfactory welds with a lap-shear strength similar to susceptorless co-consolidated joints. Additionally, fracture surfaces of these welds did not show burnt or unmelted areas. Since the purpose of this research is to investigate disassembly rather than investigate ultrasonic welding of the material used, no further research was done to find the optimum welding parameters.

Table 3.4: Final weld parameters used.

Settings	Trigger/weld/hold force [N]	Peak to peak amplitude [µm]	Sonotrode displacement [mm]	Hold time [s]
Final	500	86.2	0.07	4

3.2.3. Reference case

To set reference values for the force necessary for disassembly, single-lap shear tests at different temperatures were performed with co-consolidated samples in a temperature chamber. Both co-consolidated samples with and without susceptor were tested. A Zwick 250 kN universal testing machine equipped with a temperature chamber was used for all tests. The use of the temperature chamber required mechanical wedge clamps instead of hydraulic clamps. Again, a displacement-controlled setup with a displacement rate of 1 mm per minute was applied [2].

Based on research of Koutras et al. [25], which found that the lap shear strength decreased significantly around the glass transition temperature of the resin of a carbon fibre/PPS composite plate, three test temperatures were chosen besides room temperature. With the glass transition temperature of PEEK being 143°C according to the manufacturer's data sheet [39], the test temperature ranges were set to 128-130°C, 148-150°C and 168-170°C. For each temperature five samples with susceptor were tested. For samples without susceptor, initial trials showed no difference in lap shear strength between 128-130°C and 168-170°C. Therefore, no samples without susceptor were tested at 148-150°C. On all other levels, five samples were tested. The temperature chamber used during testing was set to a temperature 5°C higher than the desired test temperature, to ensure the sample reached the required temperature. To clamp a new sample, the chamber needed to be opened, causing a temperature drop. Therefore, it was necessary to leave some time after clamping to allow the temperature chamber to heat up again. To ensure the sample reached the required temperature before testing, a thermocouple was taped to its surface at the joint area. After 5 to 6 minutes, the thermocouple indicated that the test temperature was reached in all cases, after which the test was started.

After fracture occurred, the overlap length and width was measured in order to calculate the lap shear strength with equation 3.14. The overlap area left a clear mark on the co-consolidated samples. Both length and width were measured at the centre of the overlap for both adherends (figure 3.11a). The smallest overlap area was used to calculate the lap shear strength. If the overlap length showed clear variations, two measurements were performed as shown in figure 3.11b and the average value for the overlap length was taken. After the measurements, the fracture surfaces and cross-sections of the joint area of some samples were investigated microscopically, following the procedure described in section 3.2.7.



(a) Overlap length (l_0) and width (w_0) for a co-consolidated sample

(b) Overlap length measured at two locations if non-uniformity

Figure 3.11: Measuring the overlap length and width using the mark left behind after fracture (grey area). If there is a clear non-uniformity in overlap length, the average of two measured values is taken.

3.2.4. Experimental setup

The disassembly test setup should allow to apply a constant, measurable force and induction heating at the same time. It consists of a creep bench, which was available in the lab, an aluminium frame (induction fixture) to hold the induction coil, an induction heating station and measurement equipment. The setup is shown in figure 3.12.

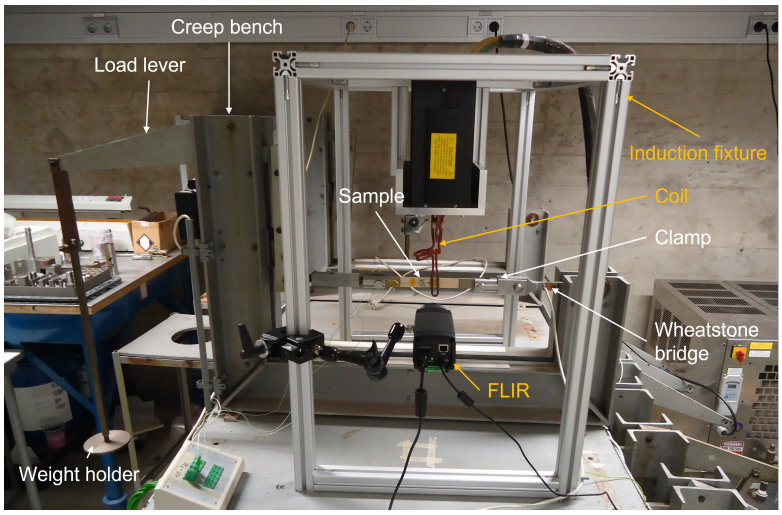


Figure 3.12: Experimental setup. Equipment with a yellow label is mounted on the induction fixture, while white labels are part of the creep bench.

The creep bench consists of a heavy steel frame with a load lever to apply weights. This load lever reinforces the applied weight with a factor of 30, which allows for relatively high loads on the sample. The sample is clamped with pin connections. On the steel dogbone part of the sample holder, strain gauges are applied in a Wheatstone bridge configuration, which allows for monitoring the load applied during the test.

An Ambrell EasyHeat LI8310 water-cooled induction heating setup was used for the experiments. This setup consists of cooling unit, a power supply and a remote work head with the induction coil. A hairpin coil was used. The coil configuration determines the frequency of the magnetic fields induced. In the setup used for this study, the frequency detected was in the range of 358-374 kHz. The EasyHeat was controlled manually, setting the current at different levels for different duration.

To evaluate the temperature of the sample, 2 K-type thermocouples were taped with kapton tape to the coil facing surface and the surface opposite to the coil, both at the centre of the overlap area. A third thermocouple was used to monitor the temperature of the environment far from the coil. Initially, ready-made thermocouples with a wire diameter of 0.2 mm were used (RS pro 363-0250). Later, a switch was made to 0.1 mm wire diameter due to more favourable behaviour in an induction field. The 0.1 mm thermocouples were manufactured manually in the lab. First, the thermocouple wires were stripped from their insulation, after which the

bare ends were twisted together. The ends of the twisted wires were welded using an RS pro L60 thermocouple welder. The lowest power settings were applied in order to prevent evaporation of the thin thermocouple wires. After welding, the weld was checked under a Keyence VR-5000 wide-area 3D measurement system. In addition to the thermocouples, a FLIR A600 series infrared camera was used to record temperatures on the coil-facing side. The camera was fixed at a distance 30 cm from the coil and set to record 5 frames per second.

To record the measurements of the Wheatstone bridge and the thermocouples, a Keithley 2701 Ethernet Multimeter was used at a frequency of 1 Hz. The FLIR infrared camera data was acquired with a dedicated software package, and exported as a temperature matrix per frame. Each matrix contains 1 temperature value per pixel. The temperatures as given by the infrared camera were used as a comparison with the thermocouple measurements, and for qualitative evaluation of the maximum temperature location. For data processing, the average temperature was taken over an area of 5 by 5 pixels, which roughly corresponds to the surface area of the thermocouple's weld. This 'window' can then be applied at different locations to plot the temperature evolution in time at the desired location. When plotting the results of the thermocouple measurements together with the FLIR measurements, this window was applied to the thermocouple area for consistency. Additionally, temperature profiles across the coil-facing surface were plotted for the last frame before fracture occurred. To do this, the temperature was averaged over a line of 1 by 5 pixels. Running this line over the full height of the sample then delivered the desired temperature profile.

3.2.5. Calibration of the setup sensors

Force measurement

First, the load application factor of the creep bench was measured. To this end, a calibrated load cell was mounted in the setup clamps and different weights were placed on the holder, after which the load cell's response was recorded. The weight was gradually increased in steps of 1 kg up to 5 kg, after which it was decreased to the starting point in steps of 1 kg. Subsequently, 5 kg was applied at once to evaluate whether there was a different response. Unfortunately, the range of the load cell was limited and no measurements beyond 5 kg could be taken. These measurements resulted in a mean load application factor of 29.6, i.e. a load of 1 N on the load lever of the creep bench resulted in a load of 29.6 N on the sample.

To continuously evaluate the load during testing, the Wheatstone bridge present on one of the clamps of the creep bench was calibrated. This was done using a Zwick 20 kN tensile test bench, applying loads step-wise, holding each load for 10 seconds. The loads varied from 20 N to 14 kN in steps of 2 kN. The bridge was fed with a voltage of 2.5 V. Each load level was held for 10 seconds. After 5 seconds, two pictures of the values of the force and voltage response were taken to record the values. From these values a slope of the voltage response versus the applied load could be calculated and normalised over the input voltage. The test was repeated three times, one of the resulting curves is shown in figure 3.13. The slope was calculated for each picture series (2 per test). Since all 6 values of the slope were close together, the average value of 24799 N/(mV/V) was taken to measure the force during disassembly tests.

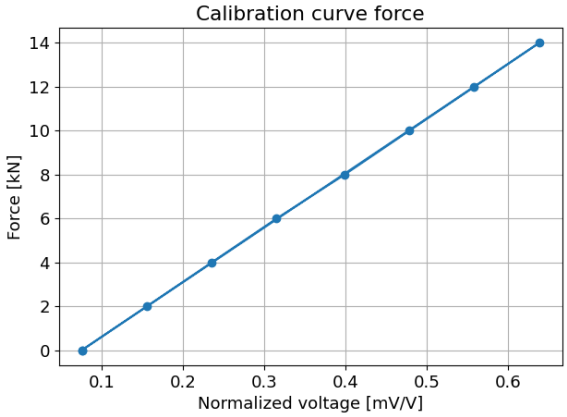


Figure 3.13: Calibration curve of the Wheatstone bridge. The output voltage is normalized over the source voltage.

Temperature measurement
The response of both types of thermocouples to an electromagnetic field was measured by attaching the thermocouples on a glass fibre/epoxy composite sample and applying the same excitation currents as in the eventual disassembly tests. Glass fibre and epoxy are both non-conducting, which implies that the sample itself does not heat up under influence of the electromagnetic field. Therefore, the measured thermocouple response is mainly related to two effects: heating of the thermocouple itself and an induced current in the thermocouple wires [35]. These two effects are errors introduced in the final measurements of carbon fibre/PEEK samples. Unfortunately, it is only possible to evaluate the effect qualitatively, as the magnetic field applied during experiments will be influenced by the presence of the carbon fibre/PEEK sample itself.

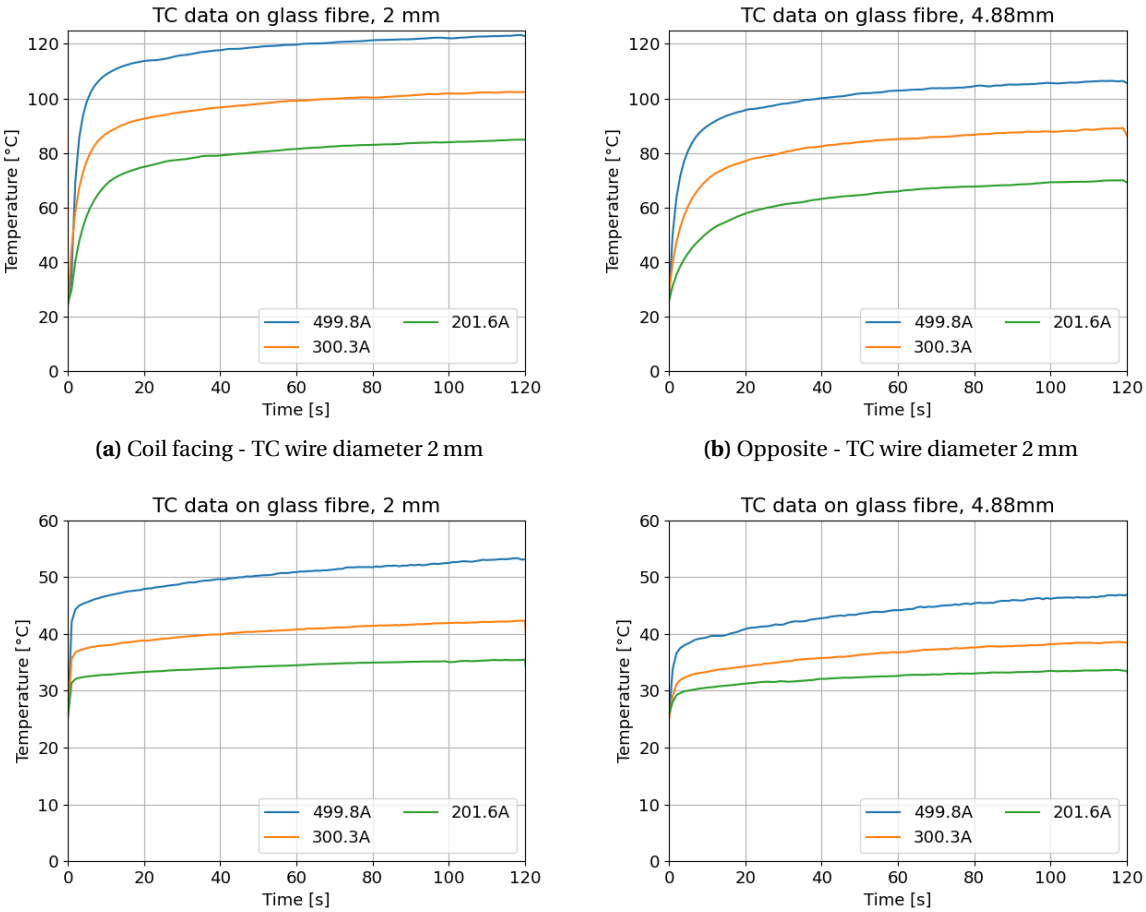
For these tests, a glass fibre/epoxy sample already available in the lab was used. This sample did however not have the same thickness (1.88 mm) as the co-consolidated samples that will be used in disassembly (~3 mm). To properly evaluate the thermocouple behaviour, it was therefore necessary to test two different coil-sample distances for these tests: 2 mm and 3 mm as measured from the coil-facing side to the coil's edge. The first distance was used to evaluate the coil-facing thermocouple's response in an induction field, while the last was used to evaluate the opposite thermocouple's response (4.88 mm and away from the coil). As the thermocouple on the coil-opposing side in disassembly tests is around 5 mm away from the coil, its behaviour is expected to lie close to the last distance measured.

Since the results of these measurements influence all further experimental results, they will be presented here instead of in the subsequent chapter. Figure 3.14 shows plots for thermocouples of different wire diameters and for different coupling distances. Both types of thermocouples behave in a similar fashion: immediately after starting the current excitation there is a jump in temperature, after which the temperature levels off and increases only slowly with time. This slower increase at the end could be attributed to the sample itself slowly heating up due to the heat of the thermocouple, decreasing heat evacuation from the thermocouple.

Two pairs of thermocouples with a wire diameter of 0.1 mm were welded in the lab. Figures 3.14c and 3.14d are representing the response of the last pair of thermocouples used. For the first pair of thermocouples welded in the lab, no proper measurement with the glass fibre sample was done before the wires snapped during a disassembly test. Small differences could be present due to slightly different winding of the thermocouple wires, but overall the trends and magnitude of the temperatures recorded by the first pair of welded thermocouples should be similar to the trends shown in these figures.

Two trends can be distinguished when comparing all subfigures of figure 3.14. Firstly, for thermocouples with narrow wires (1 mm wire diameter) the temperature jump is significantly less big, since less current is generated in these wires. Therefore, disassembly temperatures recorded during the initial measurements with 2 mm wire diameter thermocouples will be presented but not used for statistical analysis in chapter 4. Secondly, the thermocouple further away from the coil shows a less severe reaction to the electromagnetic field for both types of thermocouples. This is due to the rapid decay of the field intensity with distance from the coil. A positive effect of this is that the measurements by the non-coil facing thermocouple in the disassembly experiments should be more reliable. An additional effect that occurs during disassembly experiments of carbon fibre reinforced samples is electromagnetic shielding. According to Lenz's law, the currents generated within the sample create an electromagnetic field opposing the field excited by the induction coil. Therefore, the resulting electromagnetic field at the coil-opposing thermocouple should be significantly smaller, again making the measurement more reliable. This effect is not visible in figure 3.14, since no currents are generated in a glass fibre sample.

The last temperature sensor to check is the FLIR camera. To evaluate whether the camera was calibrated on the material's emissivity, heating measurements were performed with co-consolidated carbon fibre/PEEK samples. To prevent overheating, a low excitation current of 121.8 A and a frequency of 369 kHz was used. After the induction coil is switched off, the error in the thermocouple measurements caused by the magnetic field disappears regardless of the thermocouple type or excitation current used. Therefore, if the FLIR camera detects a temperature equal to the thermocouple temperature during the cooling of the sample, it can be assumed that the camera applies the correct settings. In figure 3.15, the FLIR and thermocouple measurement are indeed equal after the coil is switched off. However, it was noted that this was not always the case. This could possibly be attributed to air bubbles under the kapton tape that was used to fix the thermocouples on the sample. These air bubbles expand upon heating, which could cause a different reflection and hence



(a) Coil facing - TC wire diameter 2 mm

(b) Opposite - TC wire diameter 2 mm

(c) Coil facing - TC wire diameter 1 mm

(d) Opposite - TC wire diameter 1 mm

Figure 3.14: Thermocouple response in induction field

a deviating measurement for the FLIR camera. Therefore, temperature readings of the FLIR should also be interpreted with caution.

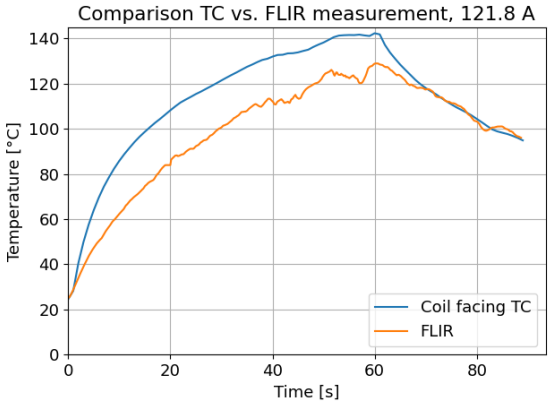


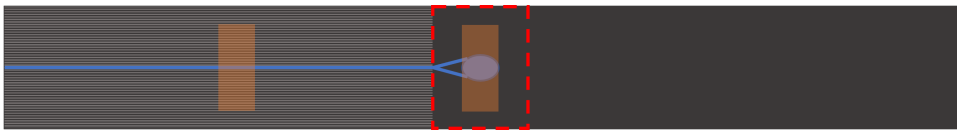
Figure 3.15: FLIR data versus coil-facing thermocouple data (TC wire diameter 2 mm)

3.2.6. Disassembly of co-consolidated joints

All disassembly experiments were performed in a similar way. First, a K-type thermocouple was taped on both the coil-facing and coil-opposing surface with kapton tape. A third thermocouple was fixed further away from the coil on the creep bench to evaluate the room temperature. The placement of the thermocouples is depicted in figure 3.16. The sample was clamped in the creep bench, after which the coil was brought into proximity of the sample, 2 mm from the coil-facing surface. This distance was checked using a 2 mm thick metal spacer. Then, a certain weight was applied to the weight holder and a current was pre-set on the EasyHeat. After recording of the Keithley (thermocouple temperatures and force) and the FLIR camera were started, the coil was turned on until fracture of the sample occurred.



(a) Bottom view. Thermocouples and wires are depicted in blue, the sample in black.



(b) Front view. Thermocouples and wires are depicted in blue, coil-facing adherend in black, opposite adherend with black-and-grey stripes. The dashed red line marks the overlap area, transparent orange rectangles depict the kapton tape used to fix the thermocouples.

Figure 3.16: Positioning of the thermocouples on a sample. A third thermocouple is attached on the creep bench, far away from the coil, to measure room temperature.

Four different weight levels were selected for testing disassembly: 15 kg, 10 kg, 5 kg and 0 kg. For the 0 kg load level, the sample holder (see figure 3.12) was disconnected from the load lever. However, the load lever itself has a weight which is applied to the sample. Therefore, 0 kg still corresponds to a force of around 450 N.

It was attempted to select one excitation current for all weight levels, but after some preliminary trials this turned out to be impossible. The excitation currents required to break samples for lower applied weights resulted in thermal damage, even for higher weight levels. Additionally, samples with susceptor could not withstand excitation currents for susceptorless samples without suffering thermal damage. Therefore, it was decided to select two excitation currents per type of sample from the preliminary trials for co-consolidated samples. The lowest value was chosen to be sufficient to break the sample at the highest weight level, while the highest excitation current was sufficient to break the sample at a weight of 0 kg.

Tests were performed starting from 15 kg and a low excitation current (different for both types of samples, see table 3.5). Subsequently, the weight level was lowered one step and the same excitation current was applied. If a sample failed to break, the excitation current was switched to the higher value. The final weight-excitation current combinations used during testing are shown in table 3.5. All tests were carried out at least twice. Since co-consolidated joints are rather uniform in quality, this amount of tests was deemed sufficient to explain the results.

Table 3.5: Excitation current per weight level for different types of samples

Weight level [kg]	Sample with susceptor Excitation current [A]	Susceptorless sample Excitation current [A]	Welded sample Excitation current [A]
15	201.6	300.3	300.3
10	201.6	300.3	300.3
5	201.6	499.8	499.8
0	300.3	499.8	499.8

Ultrasonically welded samples were disassembled using the same excitation currents as susceptorless co-consolidated samples to allow for comparison of both types of joints (table 3.5). The ultrasonic welding process, however, has more intrinsic variablity than co-consolidation. Therefore, at least three ultrasonically welded samples were tested per load level.

For all samples, fracture surfaces were inspected visually and microscopically to detect any anomalies. The microscopic investigation procedure for fracture surfaces as well as cross-sections of each sample is described in section 3.2.7.

3.2.7. Microscopic investigation

For all disassembly tests, a picture of the fracture surface was taken using a Keyence VR-5000 wide area 3D measurement system. After photographing the fracture surfaces, samples were cut at the broken overlap with a Struers Secotom-10 cutting machine to investigate the cross-section. The cutting procedure is depicted in figure 3.17. In this figure, the grey area represents the fracture surface on the sample (in black). The sample was cut along the red dashed lines. After cutting, pieces 1 to 4 (figure 3.17) were embedded in Epofix polymer with the side indicated by red arrows placed such that it could be microscopically investigated. After 12 hours of curing, the embedded samples were polished using a Struers Tegramin-20 grinding and polishing machine. Microscopic images of the cross-section were taken using a Keyence VK-X laser confocal microscope.

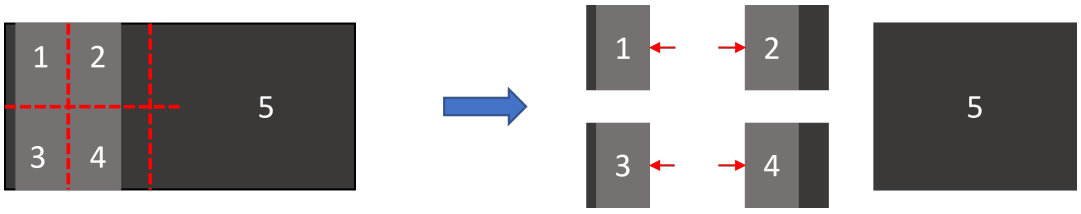


Figure 3.17: Cutting steps for microscopic investigation. The grey area represents the overlap, the black area the remaining sample. Each broken sample was cut into 5 pieces along the red dashed line. The indicated side of pieces 1 to 4 was investigated microscopically, piece 5 was discarded.

4

Results

In this chapter, the validation and results of the model will be addressed first. Subsequently, the experimental results are assessed, starting off with the reference case. The results of the disassembly experiments on co-consolidated and ultrasonically welded samples are then given, after which outcomes of the microscopic analysis are detailed. How these results contribute to answering the research question will be further elaborated upon in chapter 5.

4.1. Model

Prior to analysis of the model results, a sensitivity analysis and validation experiments are carried out. After tweaking the model to better fit experimental results, the influence of the sample position and the heating profile of the coil-facing surface are analysed. The heating profile through the thickness is also analysed, but these results remain highly uncertain since they are very complicated to verify experimentally.

4.1.1. Sensitivity analysis

In order to understand the sensitivity of the predicted temperature to small changes in material properties, a sensitivity analysis was performed. Each material property was varied with ±10%, after which the resulting temperature evolution was compared with the temperature evolution for the calculated material properties. The deviation of the temperature after 10 seconds of simulation for an increase or decrease of 10% of each material property is given in table 4.1. The time period for these simulations was decided only after model validation (see section 4.1.2). The properties μ_r and ϵ were not increased by 10% as the resulting value of these properties did not make physical sense (both are maximum 1). The sensitivity analysis was performed for an excitation current of 300.3 A and a frequency of 361 kHz for all cases.

For a susceptorless sample, in-plane electrical conductivity, heat capacity and density have the biggest influence on the temperature evolution. The latter two properties were calculated using the relatively simple rule of mixtures and material data from manufacturer's data sheets. Their magnitude is also in correspondence with values found in literature [15, 31]. The in-plane electrical conductivity, on the other hand, was more complicated to calculate due to its dependence on the direction of the fibres. As it is difficult to measure experimentally, widely varying values for the electrical conductivity of laminates are found in literature [15, 17, 31]. Therefore, the calculated value is hard to verify. Combined with its big impact on the temperature simulation, this could be a reason to change the electrical conductivity should the model prediction not deliver satisfactory results.

For the sensitivity analysis of susceptor properties, a striking result is the asymmetry in the influence of some properties. The in-plane conductivity barely seems to have an influence when it is increased with 10%, while a decrease in this property has the biggest influence of all susceptor properties. The reverse is true for the density and heat capacity. Simulations for a longer period of time showed that this asymmetry was only present at the start. After 16 seconds, the effect of an increase or decrease in these properties was similar in magnitude: 1.7% for the electrical conductivity and 1.4% for the density and heat capacity (see Appendix B). It is unknown why this asymmetry at the start of the simulation occurred. Nevertheless, it can again be

Table 4.1: Results of the sensitivity analysis. The properties (prop.) in the left column are varied with ± 10%, the resulting deviation of the temperature as compared to the original model is shown in the two right columns.

Laminate property	**Resulting T if prop. +10%**	**Resulting T if prop. -10%**
$\sigma_{in-plane}$	+7.3%	-7.5%
$\sigma_{through-thickness}$	-0.2%	+0.2%
$k_{in-plane}$	+3.3%	-3.6%
$k_{through-thickness}$	-0.8%	+0.9%
c_p	-9.0%	+11.0%
μ_r	-	-2.8%
ρ	-9.0%	+11.0%
ϵ_r	0	0
ϵ	-	+0.3%
Susceptor property	**Resulting T if prop. +10%**	**Resulting T if prop. -10%**
$\sigma_{in-plane}$	+0.06%	-1.37%
$\sigma_{through-thickness}$	0	-0.01%
$k_{in-plane}$	+0.13%	-0.12%
$k_{through-thickness}$	-0.05%	+0.06%
c_p	-1.20%	+0.07%
μ_r	-	-0.45%
ρ	-1.20%	+0.07%
ϵ_r	0	0

concluded that the in-plane conductivity, heat capacity and density are the major material properties that affect the temperature predictions of the model.

4.1.2. Model validation

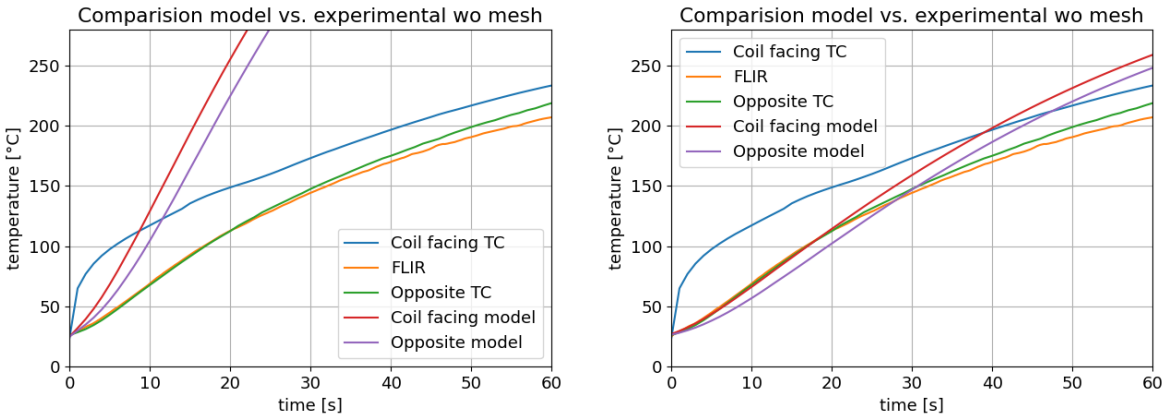
Samples without susceptor

Experimental measurements of the temperature evolution at the sample's surface for samples without susceptor differed significantly from what was predicted using the material parameters calculated in section 3.1.2. As can be seen in figure 4.1a, the model severely overpredicts the heat generation in samples without susceptor. From the sensitivity analysis, it was decided to try changing the in-plane electrical conductivity to find a better correspondence between the simulated and experimental results.

For an in-plane electrical conductivity of 6000 S/m the model prediction corresponds reasonably well with the experimental results. Figure 4.1b shows that for the applied settings, the slope of the temperature increase is similar for simulated and experimental values during the first 20 seconds, except for the measurement of the coil facing thermocouple. The deviation for this measurement can be explained by the thermocouple's response to a magnetic field, as was discussed in section 3.2.5. After 40 seconds, the experimentally measured temperature increase slows down, which can be explained by the change in material properties with increasing temperature. The electrical conductivity of the laminate decreases with increasing temperature and the heat capacity slightly increases [15]. Both effects result in a lower heating rate at higher temperatures. As this was not taken into account in the model, the deviation between experimental and simulated values at higher temperatures is not unexpected.

The main reason for this significantly lower effective conductivity is believed to be found in fibre-to-fibre contact. The material model assumes that all fibres are conducting, but since closed loops and therefore contact between fibres is required, this might not be accurate. In laminates made of unidirectional plies, there are almost certainly portions of fibres that are not in contact with any other fibres, which diminishes the electrical conductivity. Since the model does not account for this effect, the calculated conductivity could be much higher than the effective conductivity in the laminate.

To validate the adjusted model, the temperature evolution was simulated for an excitation current of 499.8 A



(a) $\sigma_{in-plane} = 17206$ S/m

(b) $\sigma_{in-plane} = 6000$ S/m

Figure 4.1: Comparison of the model prediction versus experimental measurements for susceptorless co-consolidated samples tested at 300.3 A

and compared to experimental measurements from the disassembly tests. Figure 4.2 shows that there is a reasonable correspondence between the model prediction and the experimental data for a period of around 12 seconds. After that, the experimentally measured temperature levels off due to the changing material properties. Based on this plot it can be decided that the adjusted model works relatively well for temperature predictions at the thermocouple location for susceptorless samples. More experimental validation with different disassembly parameters would however be helpful to increase confidence in the adjusted material model. Due to time constraints it was not feasible to perform further validation experiments.

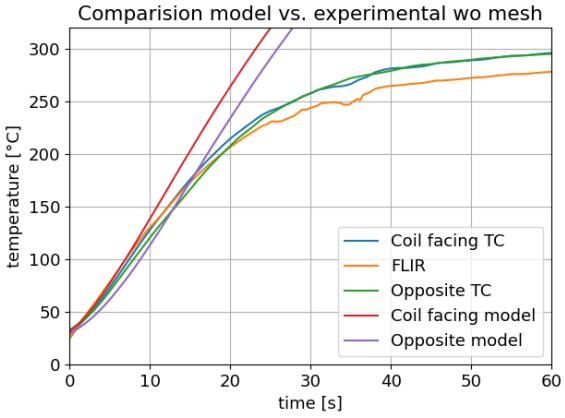
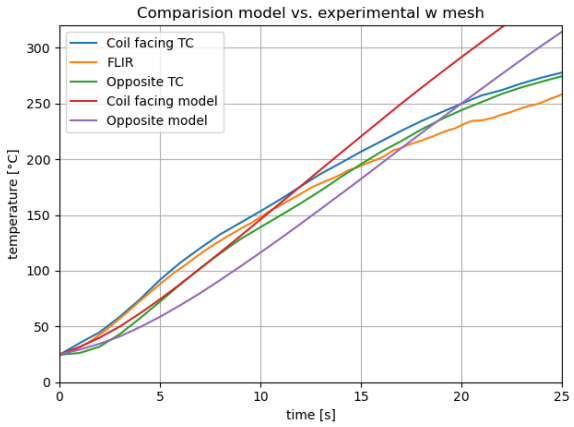


Figure 4.2: Comparison of the model prediction versus experimental measurements for susceptorless co-consolidated samples tested at 499.8 A

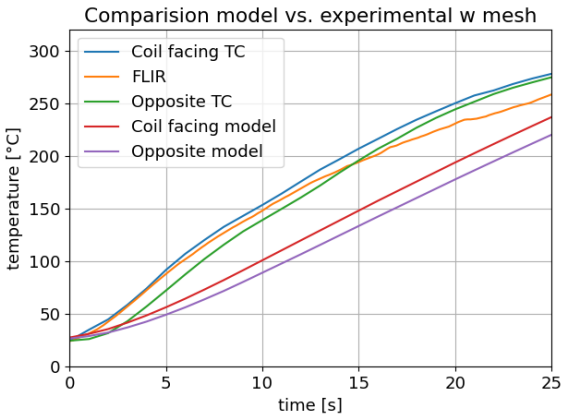
Samples with susceptor

The original conductivity as calculated in sections 3.1.1 and 3.1.2 for samples with susceptor results in a surprisingly good correspondence with experimental values (figure 4.1a). However, it makes little sense to use a different laminate conductivity for the model with susceptor. Moreover, the simulated results underestimate the initial heating quite severely. When the laminate conductivity is corrected to the value of 6000 S/m, as found in the previous section, this underestimation of the temperature is even worse (figure 4.3b). Again, it was tried to change the in-plane conductivity. This time, the conductivity of the metal mesh/PEEK layer was increased to find a closer fit with experimental results of the samples with susceptor.

A reasonable correspondence between experimental results and model predictions for the applied settings



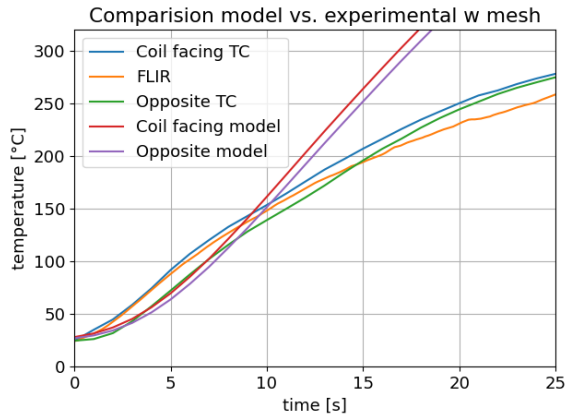
(a) Conductivity of mesh and laminate as calculated



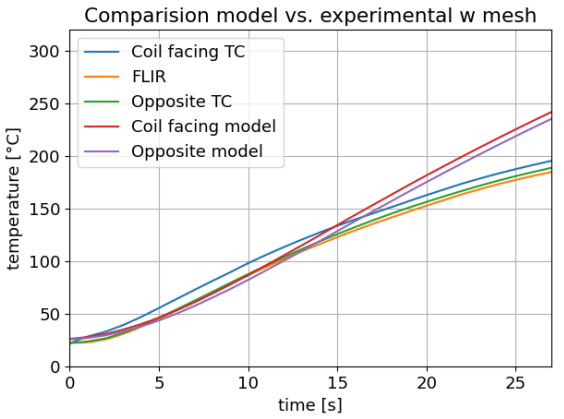
(b) Adjusted laminate conductivity (σ = 6000 S/m)

Figure 4.3: Comparison of the model prediction versus experimental measurements for co-consolidated samples with susceptor, for an excitation current of 300.3 A

was found when the in-plane conductivity of the metal mesh/PEEK layer was increased to 500000 S/m (figure 4.4a). Especially for the first 10 seconds of simulation, the model follows the experimental measurements closely. The simulation was repeated for an excitation current of 201.6 A to validate the model prediction. Figure 4.4b shows an even better correspondence between the model and experiments. At higher temperatures, the experimental curves for both excitation currents level off again due to changes in material properties.



(a) $\sigma_{in-plane,laminate}$ = 6000 S/m - $\sigma_{in-plane,susceptor}$ = 500000 S/m - 300.3 A



(b) $\sigma_{in-plane,laminate}$ = 6000 S/m - $\sigma_{in-plane,susceptor}$ = 500000 S/m - 201.6 A (for validation)

Figure 4.4: Comparison of the model prediction versus experimental measurements for co-consolidated samples with susceptor for adjusted properties

The question arises why the conductivity of the susceptor layer should be increased so immensely. After checking all calculations, no clear reason for this increase was found. Since the conductivity of the susceptor layer is dominated by the stainless steel mesh, the mesh properties were measured in the lab. However, all dimensions were as reported by the manufacturer, and after measuring the resistance of a single wire of the mesh with a multimeter it was found that the electrical conductivity of metal used in the model was correct. Clearly the reason for the deviation between the model and experimental results should be sought elsewhere.

A cross-section of a broken joint was analysed microscopically to investigate the interface more closely. In figure 4.5 the imprint left by the metal mesh can be clearly seen. From this figure, it is clear that fibres are found between the mesh, which invalidates the assumption that only PEEK and metal was present in the

susceptor layer. This has implications for all material properties calculated. Carbon fibres have half the heat capacity of the PEEK polymer and are 1.4 times more dense (table 3.3). This would already result in higher heating rates than predicted in figure 4.3b. It would also increase the electrical conductivity of the susceptor layer, but again, closed fibre loops are required to achieve an increase in the effective conductivity. Inspecting figure 4.5 more closely allows to identify another effect of the mesh imprint: a local increase in fibre density, which affects the first two layers adjacent to the joint interface. Therefore, more contact between the fibres in these layers is expected, leading to more closed loops and thus more electrical conductivity close to the interface. Additionally, the fibre-to-metal contact between the composite and the metal mesh enables current flow between those components. All these effects combined could explain the large deviation between the simulated and experimental results in figure 4.3b.

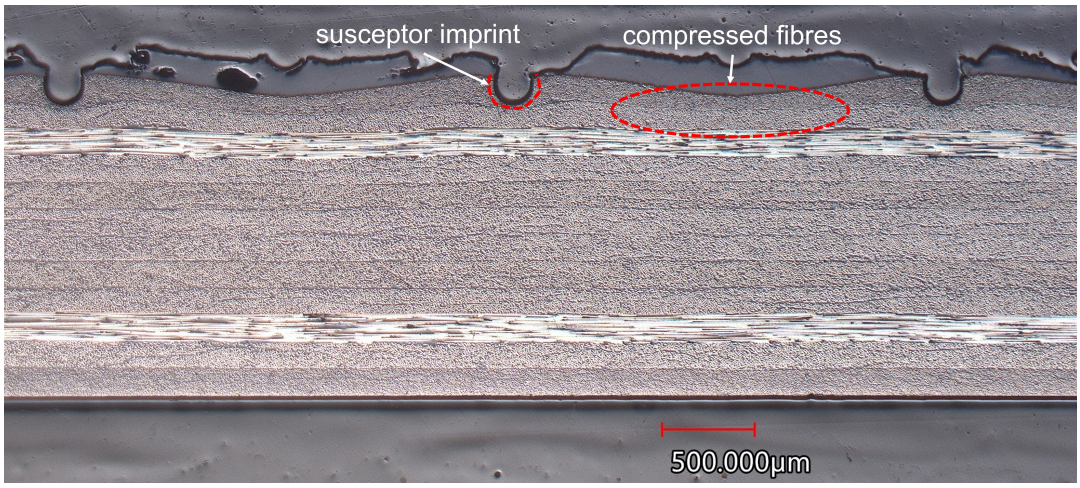


Figure 4.5: Microscopical image of the cross-section of a sample with susceptor. The mesh imprint and the compressed laminate layers are indicated in the picture. Note that the mesh imprint itself also causes local fibre compression.

The findings of the microscopic analysis cast doubt on the validity of the adjusted model, despite the reasonably good fit that was achieved in figure 4.4. As was explained in previous paragraph, all material properties are affected by the presence of carbon fibres in between the susceptor. Only varying the conductivity is therefore inaccurate. Moreover, the model geometry might not be the best choice: the susceptor layer was modelled as a 0.4 mm thick layer sandwiched in between the composite laminate adherends. This approach assumes that the susceptor is not pressed into the laminate, which is clearly not true (see figure 4.5). Additionally, the first two laminate layers adjacent to the susceptor could have different material properties as compared to the rest of the laminate due to the local compression of fibres. It could therefore be more useful to develop a multi-layered model to accommodate for the changes in material properties throughout the thickness of the sample. Since this work could be a master thesis in itself, it was decided to keep working with the fitted model of figure 4.4. This implies that any results derived from this model should be interpreted with care to not draw wrong conclusions.

4.1.3. Model results

The model with adapted electrical conductivity was used to determine the influence of sample positioning on heating and to investigate the heating profile. Only qualitative analyses were performed due to the uncertainty about the accuracy of the model. As most experimental data was gathered for the coil-facing surface, plots were made for the coil-facing side. An excitation current of 300.3 A was used for the model. Results are shown for a period of 11 seconds, as this appeared to be the range for which the model corresponded to experimental findings. All results are plotted for the thermocouple locations (see figure 3.16).

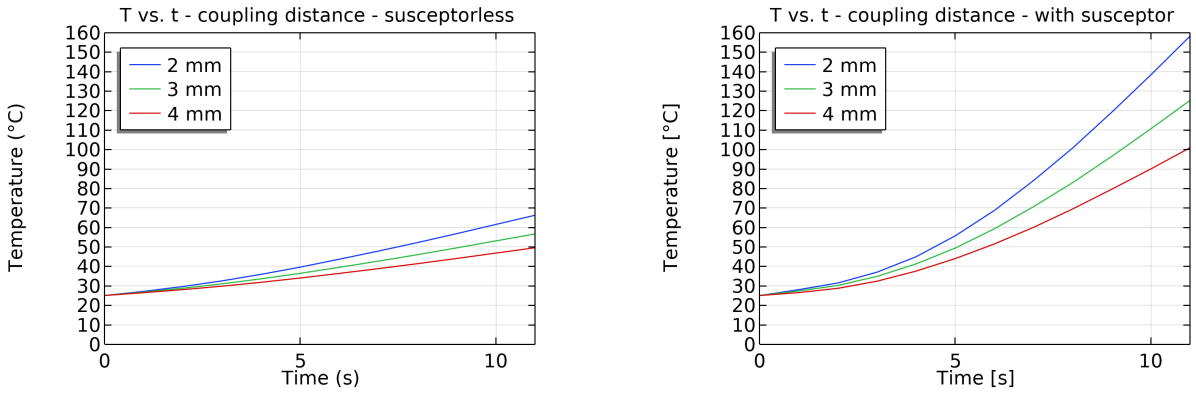
Influence of sample position on temperature evolution

To investigate the influence of the sample position, the distance between coil and sample (coupling distance) was varied and eccentricities with respect to the coil were applied separately.

First, the coupling distance was varied step-wise: coupling distances of 2 mm, 3 mm and 4 mm were used. As visible in figures 4.6a and 4.6b, even a small difference in coupling distance can result in a relatively large difference in the joint temperature. According to the law of Biot-Savart, the magnetic field intensity decreases severely with increasing distance from the coil:

$$\mathbf{H} = \frac{I}{4\pi} \oint \frac{d\mathbf{s} \times \mathbf{r_{cp}}}{r_{cp}^3} \tag{4.1}$$

where I is the excitation current, $d\mathbf{s}$ is a curve element of the conductor and r_{cp} is the distance to the coil. Since the dissipated power is proportional to the square of the magnetic field intensity [31], it is expected that even slight variations in coupling distances can have a large influence on the temperature reached within the heated sample.



(a) Susceptorless sample

(b) Sample with susceptor

Figure 4.6: Influence of the coupling distance on the temperature evolution

Subsequently, the coupling distance was fixed at 2 mm and the eccentricity was varied in from -4 mm to 4 mm in steps of 2 mm. Figure 4.7 shows the eccentricities of -4 mm and 4 mm as well as the origin for clarification.

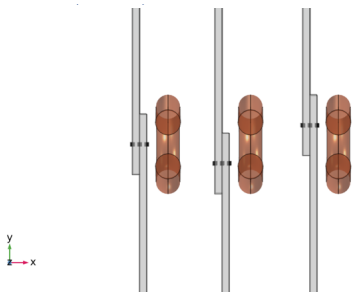
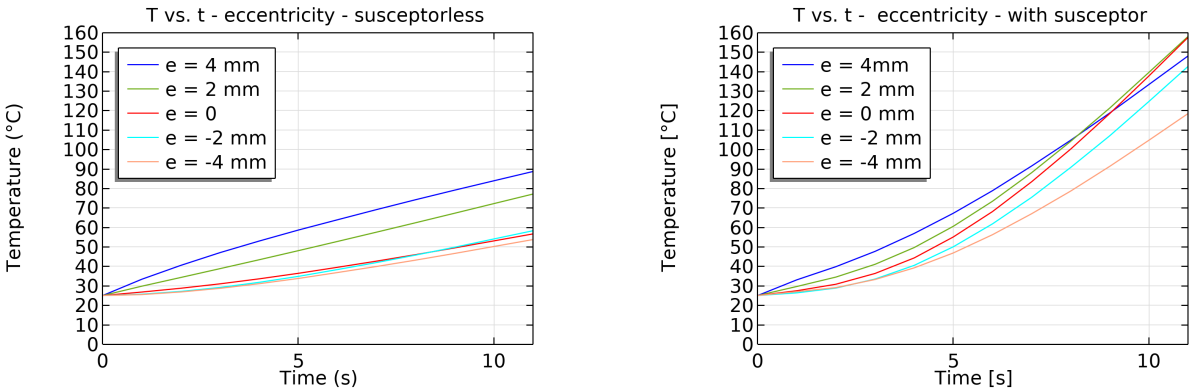


Figure 4.7: Eccentricity, left: e = 0, middle: e = -4 mm, right: e = 4 mm

The influence of eccentricity on the temperature at the joint interface is shown in figures 4.8a and 4.8b. Two trends become clear: a negative eccentricity has a different influence on the temperature evolution than a positive eccentricity, and the influence of eccentricity is different for samples with susceptor as compared to susceptorless samples.

A negative eccentricity (figure 4.7) causes the adherend that is furthest away from the coil to be more centered with respect to the coil. This means that less material is close to the coil, which results in slower heating and lower temperatures for both types of samples. For positive eccentricities, different trends can be seen. A positive eccentricity increases the heat development at the susceptorless sample's coil-facing surface, as more laminate material is closer to the coil. For a sample with susceptor, this also holds true when heating



(a) Susceptorless sample

(b) Sample with susceptor

Figure 4.8: Influence of the eccentricity on the temperature evolution

starts. However, the difference quickly diminishes. An eccentricity of 4 mm even results in lower temperatures than no eccentricity at 11 seconds. Possibly this can be attributed to the fact that the heat development in the susceptor itself is dominant. Both positive and negative eccentricities cause the susceptor to be less well-centered with the coil, which could negatively affect heating.

Figures 4.6 and 4.8 clearly show the dependence of the temperature evolution on positioning of the sample with respect to the coil. It would therefore be necessary to closely control positioning of the sample during experiments. When designing the setup, it was chosen to use a fixed frame to lock the position of the coil. This was supposed to eliminate the possibility for eccentricities. However, it was not taken into account that there would be variations in dimensions of the samples. Hence, the whole frame needed to be moved slightly when an eccentricity was apparent. This could have caused scatter in the experimental measurements. The coupling distance was easier to check: whenever a sample was clamped, a 2 mm thick metal plate was inserted between the coil and sample surface to ensure a consistent coupling distance.

Heating profile of the coil-facing surface

The heating profile of a susceptorless sample is shown in figure 4.9. Heat development seems more severe at the sample's edges. The preferential heating of the edges – known as the edge effect – is caused by an abrupt constraint in the electric paths, forcing the current to follow the edge. This locally increases the current density, which results in higher losses and therefore more heating at the edge [18]. For the simulation of samples with susceptor the high electrical conductivity of the susceptor caused unrealistically high temperature at the edges. It was therefore chosen to disregard this result.

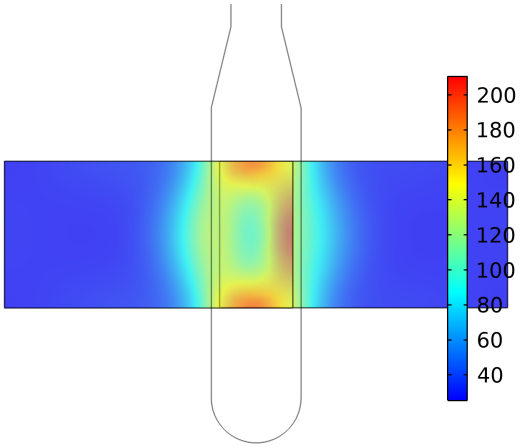
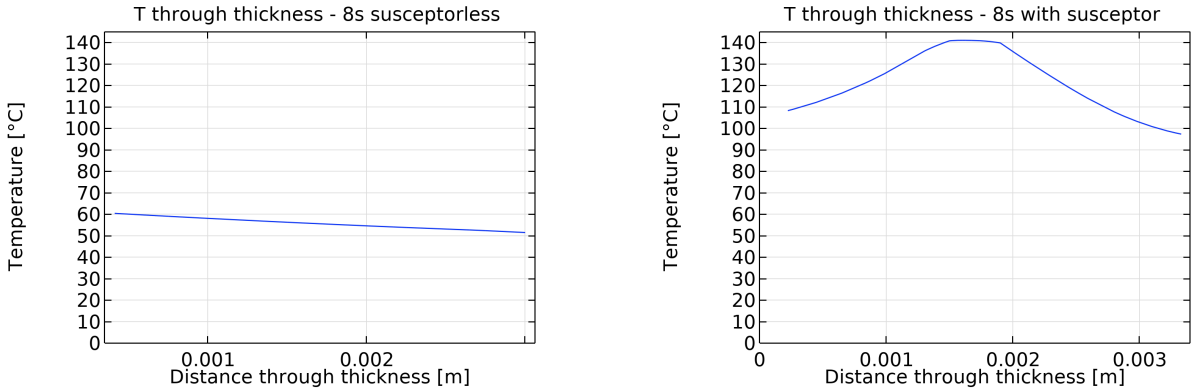


Figure 4.9: Heating profile at 20 s for susceptorless sample

Heating profile through the thickness

Figures 4.10a and 4.10b show the heating profiles through the thickness at 8 seconds for a susceptorless sample and a sample with susceptor, respectively. For the susceptorless sample, the maximum temperature occurs at the sample's coil-facing surface. This preferential heating of the surface is not unexpected, as the magnetic field intensity quickly decays with increasing distance from the coil. For a sample with susceptor, the heating mainly occurs within the susceptor layer. However, this was not the case for the original conductivity calculated in section 3.1.1. Since the conductivity was changed to fit the model curves to the experimental curves and it is hard to measure temperature or conductivity at the interface, care should be taken when interpreting these results.



(a) Susceptorless sample

(b) Sample with susceptor

Figure 4.10: Heating profile through the thickness at 8 seconds of heating time

4.2. Experimental

In this section, all experimental results will be addressed. The results of the reference and the search for satisfactory weld parameters for ultrasonic welding are described first. Subsequently, the results of the disassembly experiments, the fracture surfaces and the microscopic images of the cross-sections will be investigated.

4.2.1. Reference case

The resulting single lap shear strengths for the reference case are plotted and statistically analysed in order to identify trends. Furthermore, the fracture surface and microscopic cross-section are described for samples tested at the highest temperature (168-170°C).

Test results

The test results of co-consolidated samples are shown in figure 4.11. Numerical results are given in table 4.2.

Table 4.2: Lap shear strength results for co-consolidated samples

Co-consolidated samples with susceptor

Value	25°C	128-130°C	148-150°C	168-170°C
Mean LSS [MPa]	36.17	26.94	25.63	20.11
St. dev. LSS [MPa]	1.37	4.79	2.50	2.42

Susceptorless co-consolidated samples

Value	25°C	128-130°C	148-150°C	168-170°C
Mean LSS [MPa]	40.70	29.74	-	28.28
St. dev. LSS [MPa]	2.75	1.69	-	2.83

To analyze trends, one-sided Welch t-tests were performed. The testing procedure and detailed results are further specified in Appendix C. The statistically significant trends are discussed in this paragraph. Sam-

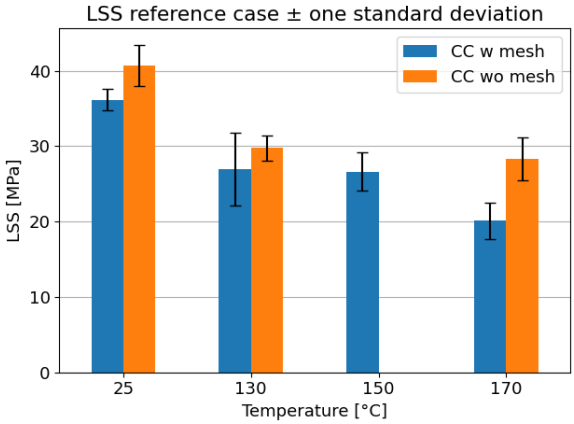
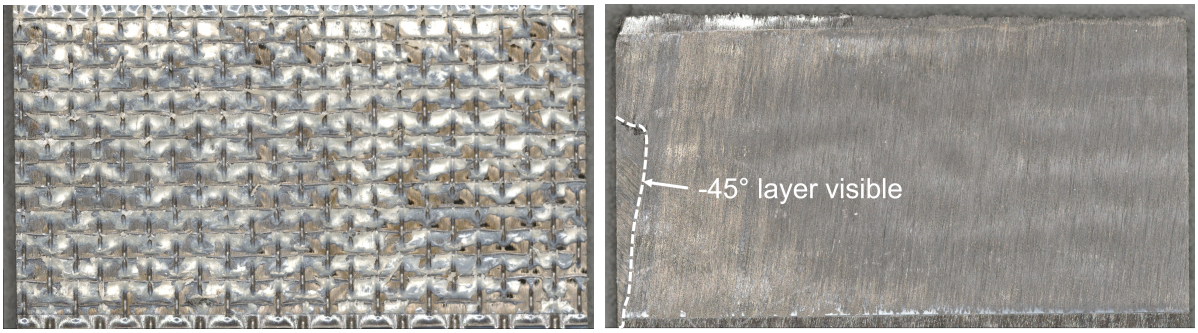


Figure 4.11: Mean lap shear strength at different temperatures for co-consolidated samples

ples with susceptor (blue bars) show a clear decrease in strength from room temperature to 128-130°C and from 150°C to 170°C. Between 128-130°C and 148-150°C there is no significant difference. For susceptorless samples (orange bars), there is also a clear decrease in strength between room temperature and 128-130°C. Between 128-130°C and 168-170°C, however, no significant difference was detected. The last trends visible are the differences between co-consolidated samples with and without susceptor. For all cases, susceptorless samples appear to have a higher strength than their counterparts with susceptor. Only at 128-130°C, the wide standard deviation of co-consolidated samples with susceptor prevented the confirmation of this trend by t-tests: no difference in lap shear strength was detected at this level.

Fracture surfaces and microscopy

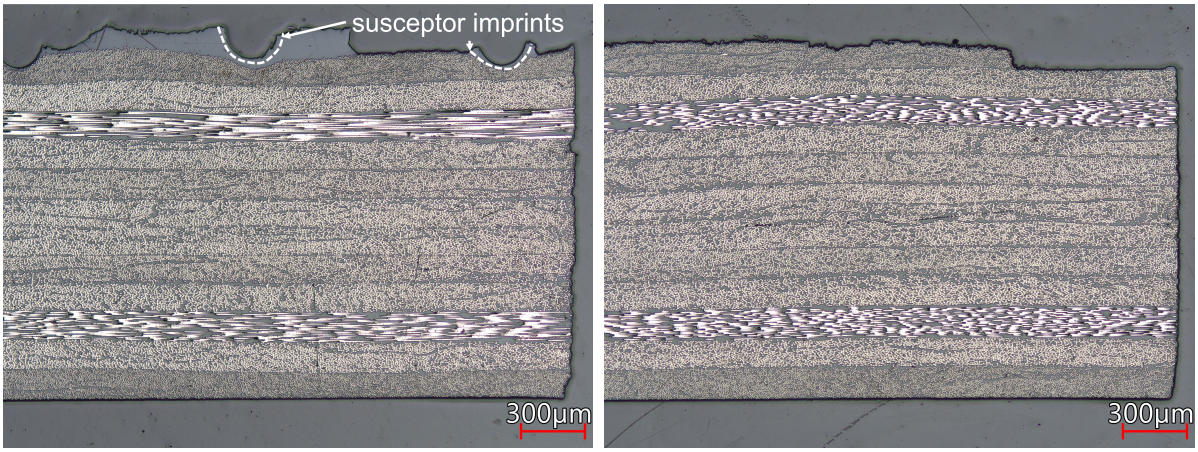
The fracture surfaces for a sample with and without susceptor tested at 168-170°C are shown in figure 4.12a and 4.12b, respectively. For the sample with susceptor, the imprint of the stainless steel mesh is clearly visible. Some PEEK polymer remnants are found all over the surface in the form of white spots. In between those spots the carbon fibres of the composite are visible. For the sample without susceptor, a rather smooth fracture surface can be seen. At the edge on the left of the picture, the first layer was broken off and a -45° layer is visible.



(a) Sample with susceptor **(b)** Susceptorless sample

Figure 4.12: Fracture surfaces of reference case samples tested at 168-170°C

The microscopic cross-sections are depicted in figure 4.13. If thermal damage were present, voids and delaminations would be visible as black marks on the pictures. No such features can be identified in figure 4.29. The susceptor imprint, however, is clearly visible in figure 4.13a.



(a) Sample with susceptor **(b)** Susceptorless sample

Figure 4.13: Microscopic images of the cross-section for reference case samples tested at 168-170°C

4.2.2. Ultrasonic welding

Initial trials were conducted based on the research of de Bruin et al. [7]. However, the parameters used in this study were optimised for a cross-ply layup of unidirectional carbon fibre/PEEK plies. The change in layup changed the stiffness of the adherends, which resulted in burnt samples for the initial parameters used (table 4.3).

The weld force was halved to prevent burning of samples. Multiple sonotrode displacements were tested, but eventually a sonotrode displacement of 0.07 mm seemed to give satisfactory results, both regarding single lap shear strength and fracture surfaces. Testing of five samples at room temperature resulted in a mean lap shear strength of 41.3 MPa with a standard deviation of 2.7 MPa. The fracture surface given in figure 4.14 shows some fibre distortion due to resin squeeze-out at the edges, but this is acceptable for laminates made of unidirectional tape.

Table 4.3: Initial and final weld parameters

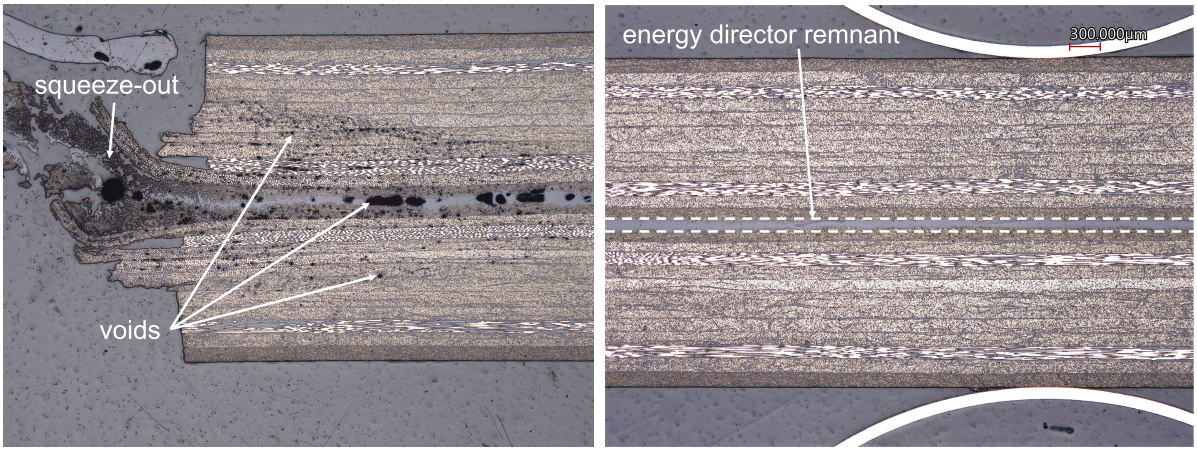
Settings	Trigger/weld/hold force [N]	Peak to peak amplitude [µm]	Sonotrode displacement [mm]	Hold time [s]
Initial	1000	86.2	0.12	4
Final	500	86.2	0.07	4



Figure 4.14: Fracture surface of an ultrasonically welded sample

The lap shear strength reached for the final settings was similar to that of co-consolidated samples without susceptor (see table 4.2). Additionally, fracture surfaces of samples welded with these settings did not show any burnt or unwelded areas. Since the aim of this study is to investigate disassembly rather than optimization of ultrasonic welding, it was decided to use these parameters for all subsequent samples.

Microscopic pictures of the cross-section of an ultrasonically welded sample are shown in figure 4.15. At the edge of the weld (figure 4.15a), squeeze-out and voids are clearly visible. Apparently quite some damage is already inflicted during welding itself, which makes it harder to detect damage inflicted during disassembly. No such voids are visible at the centre of the joint (figure 4.15b). Here, the energy director remnant at the joint interface is clearly distinguishable.



(a) Edge weld **(b)** Centre weld, ED remnant visible between dashed lines

Figure 4.15: Microscopic images of the cross-section for an ultrasonically welded sample

4.2.3. Disassembly

The results of the disassembly experiments will be described in three steps. First, the disassembly process will be evaluated, by investigating trends of different disassembly parameters at break. The temperatures at break, disassembly time and reduction in lap shear strength will be assessed more closely. Temperature evolution with time and temperature profiles across the sample surface will also be described. Secondly, the fracture surfaces of disassembled samples will be examined to identify possible damage left by the induction heating. Lastly, microscopic pictures of the cross-section of disassembled samples will be analysed.

Disassembly process

The recorded experimental values for all disassembled samples are shown individually in table 4.4. The sample name "CC" refers to co-consolidated, while "USW" refers to an ultrasonically welded specimen. For all samples, it is indicated whether a susceptor was present at the joint interface ("Mesh"). Subsequently, the excitation current (I), disassembly time (t) and recorded temperatures are shown. Here, T_{TC1} refers to the temperature of the coil-facing thermocouple, T_{FLIR} to the temperature recorded by the infrared camera and T_{TC2} was recorded by the thermocouple opposite to the coil. The lap shear strength (LSS) was recorded and it was calculated what fraction of the lap shear strength of the reference case at room temperature remained ($f_{LSS\text{-}RT}$). The last column indicates whether damage was present on the cross-sections of the sample. In the subsequent paragraphs, some more explanation about the symbols and codes used in the table will be given.

Some sample names are bold and italic, indicating that this sample was reheated. Either the sample was used on a low current level for preliminary testing, or the first test attempt went wrong and was interrupted. The first heating cycle could have affected the crystallinity in the sample, which could then in turn affect its behaviour in induction heating. However, since the heating behaviour is predominantly determined by the fibres and results of these samples were similar to other experimental values, it was decided to include them in the analysis.

Some of the temperatures depicted in the table have one or two asterisks next to their numeric value (* or **). One asterisk indicates that a K-type thermocouple with 0.2 mm wire diameter was used. For all other measurements, 0.1 mm wire diameter was used. However, at some point during measurements the first thermocouples with a 0.1 mm wire diameter broke upon fracture of a sample. New thermocouples with 0.1 mm wire diameter were therefore manufactured. The measurements acquired by these new thermocouples are indicated with a double asterisk (**).

Table 4.4: Results of the disassembly experiments. Bold and italic sample names indicate reheating. One asterisk (*) signifies a 0.2 mm wire diameter of the thermocouple, two asterisks (**) mark a measurement with the second pair of 0.1 mm wire diameter thermocouples.

Weight level 15 kg

Sample	Mesh	I [A]	t [s]	T_{TC1} [°C]	T_{FLIR} [°C]	T_{TC2} [°C]	LSS [MPa]	$f_{LSS\text{-}RT}$ [%]	Damage
CC-1	Yes	201.6	32	211.4	197.8	204.1	13.8	38.1	No
CC-2	No	300.3	86	236.9*	212*	253*	14.5	35.6	No
CC-3	No	300.3	70	221.1*	207.2*	225.2*	15.3	37.6	No
CC-4	No	300.3	76	270.0	249.7	257.5	16.2	39.8	No
CC-5	No	300.3	48	248.1**	246.4**	255.7**	15.3	37.7	Yes
USW-1	No	300.3	33	158.7*	146.9*	164.8*	15.0	36.2	Yes
USW-2	No	300.3	41	242.9	226.6	221.0	15.1	36.6	Yes
USW-3	No	300.3	81	265.6	241.14	246.9	15.4	37.2	Yes
USW-4	No	300.3	37	-	232.1	209.5	16.0	38.7	Yes
USW-5	No	300.3	74	251.5	246.3	244.7	15.6	37.7	Yes

Weight level 10 kg

Sample	Mesh	I [A]	t [s]	T_{TC1} [°C]	T_{FLIR} [°C]	T_{TC2} [°C]	LSS [MPa]	$f_{LSS\text{-}RT}$ [%]	Damage
CC-6	Yes	201.6	31	192.1*	182.9*	181.9*	10.5	29.1	No
CC-7	Yes	201.6	52	211.0*	-	226.9*	10.1	27.9	No
CC-8	Yes	201.6	28	222.0	211	217.3	9.2	25.5	Yes
CC-9	Yes	201.6	48	233.0	218.8	217.3	11.2	31.0	No
CC-10	No	300.3	64	240.0*	218.6*	228.1*	10.9	26.9	Yes
CC-11	No	300.3	67	-	249.9	263.9	11.5	28.3	Yes
CC-12	No	300.3	97	273.9**	261.7**	271.9**	10.3	25.4	Yes
CC-13	No	300.3	172	277.9**	254.3**	277.8**	10.9	26.8	Yes
USW-6	No	300.3	158	245.0*	226.9*	242.1*	10.2	24.8	Yes
USW-7	No	300.3	-	289.0	275.5	263.4	-	-	Yes
USW-8	No	300.3	-	291.0	278.8	278.7	-	-	Yes
USW-9	No	300.3	224	295.1	270.4	288.4	10.5	25.5	Yes

Weight level 5 kg

Sample	Mesh	I [A]	t [s]	T_{TC1} [°C]	T_{FLIR} [°C]	T_{TC2} [°C]	LSS [MPa]	$f_{LSS\text{-}RT}$ [%]	Damage
CC-14	Yes	201.6	52	206.0*	189.0*	219.0*	4.9	13.4	Yes
CC-15	Yes	201.6	57	-	-	262.5	5.4	14.9	Yes
CC-16	Yes	201.6	53	-	-	256.8	6.5	18.0	No
CC-17	No	499.8	26	254.9*	237.9*	223.3*	6.1	14.9	Yes
CC-18	No	499.8	30	270.8	255	276.2	6.1	15.1	Yes
CC-19	No	499.8	30	282.4	268.1	284.0	6.1	15.1	Yes
USW-10	No	499.8	57	283.1*	248.9*	260.0	5.6	13.6	Yes
USW-11	No	499.8	40	318.5	293.2	274.2	6.0	14.5	Yes
USW-12	No	499.8	44	302.7	283	280.3	6.0	14.6	Yes
USW-13	No	499.8	31	292	284.5	287.9	6.0	14.6	Yes

Weight level 0 kg

Sample	Mesh	I [A]	t [s]	T_{TC1} [°C]	T_{FLIR} [°C]	T_{TC2} [°C]	LSS [MPa]	$f_{LSS\text{-}RT}$ [%]	Damage
CC-20	Yes	300.3	24	228.6*	225.1*	239.2*	1.0	2.8	Yes
CC-21	Yes	300.3	22	-	-	271.2	1.5	4.1	Yes
CC-22	Yes	300.3	26	281.4	269.6	278.8	1.5	4.2	Yes
CC-23	No	499.8	46	283.5	264.6	270.8	1.2	3.0	Yes
CC-24	No	499.8	45	-	285.9	298.5	1.6	3.8	Yes
CC-25	No	499.8	80	303.4	285.3	296.9	1.5	3.8	Yes
CC-26	No	499.8	60	-**	269.8**	294.7**	1.5	3.7	Yes
USW-14	No	499.8	-	331.7*	314.6*	272*	-	-	Yes
USW-15	No	499.8	182	326.2	277.8	278.5*	1.3	3.1	Yes
USW-16	No	499.8	76	328.8	318.2	300.5	1.4	3.4	Yes
USW-17	No	499.8	-	346.6	306.9	293.5	-	-	Yes
USW-18	No	499.8	143	326.1	319.4	289.3	1.7	4.2	Yes

Within the experimental values recorded, some values are missing in the table and replaced by a dash (-). A dash solely in the T_{TC1} column indicates that TC1 showed erratic behaviour, with the temperature suddenly levelling off or jumping to unrealistic values at the start. The former is probably caused by loss of contact with the sample's surface, the latter by incorrect positioning of the thermocouple. Missing values in both the T_{TC1} and T_{FLIR} column indicate that the kapton tape of the coil-facing thermocouple fully released, invalidating both measurements at the thermocouple location. Dashes in the last two columns indicate that the sample did not break within four minutes of induction heating. For these samples, the temperatures depicted in the table are the maximum temperatures recorded by each sensor (for the camera: maximum temperature in the thermocouple region). This failure to break at certain weight-excitation current combination occurs particularly often for ultrasonically welded samples. To enable comparison with susceptorless co-consolidated samples and because damage was already found on the cross-sections and surfaces of these samples, it was decided to not increase the excitation current to ensure fracture.

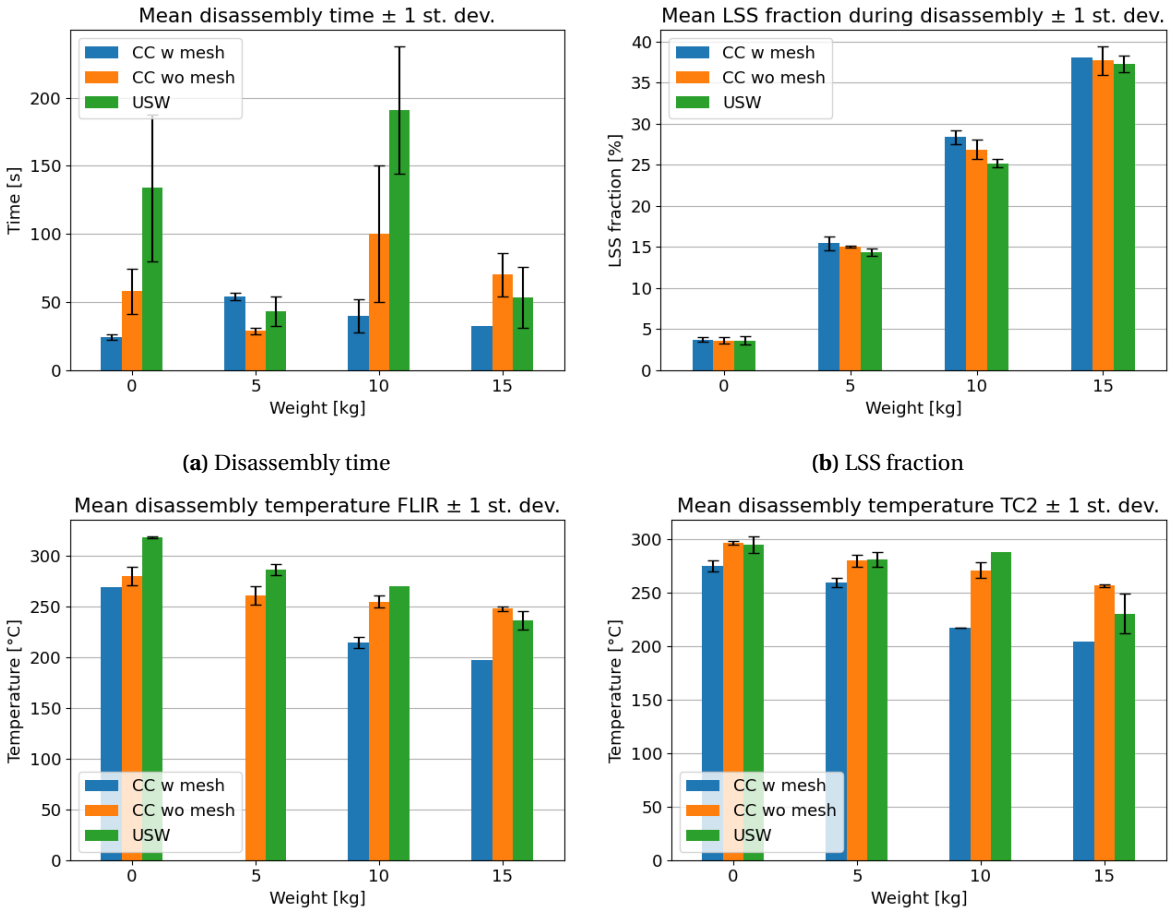
The last thing to notice in the table is that only one sample with susceptor was tested at 15 kg. One more sample was tested at this level, but the test resulted in unexpectedly low values for time and temperature. This was attributed to a manufacturing error: the plate from which these samples were cut had a small warpage, which resulted in an incorrect cut during manufacturing of the sample. This led to a notch in the sample, close to the joint, which decreased the strength significantly. Since up to then no damage was found in the 10 kg case for samples with susceptor, it was decided to use the remaining samples without this manufacturing error on the lower weight levels.

The results of table 4.4 were further processed to identify trends. Bar charts of the mean value are shown in figure 4.16. The error bars indicate the standard deviation on these averages. Samples that did not break were excluded from the analysis. For the temperature charts, only the values recorded by thermocouples with a 0.1 mm wire diameter were used. Hence, some disassembly parameters only have one data point for analysis. These parameters do not have a standard deviation plotted on the bar chart. To properly identify trends, multiple t-tests were performed. Since the sample size of different bars varied, a Welch t-test was chosen. It should be noted that the sample size is rather small for statistical analysis, and therefore the trends identified should be treated with caution. Again, the testing procedure and results are further detailed in Appendix C. All trends described in subsequent paragraphs were confirmed by the t-tests with a confidence level of at least 90%, unless specified otherwise.

Figure 4.16a clearly shows some trends in the difference in disassembly time between samples types and weight levels. For each weight level except 15 kg, ultrasonically welded samples took longer to disassemble than co-consolidated samples without susceptor. At 15 kg ultrasonically welded samples were disassembled faster than their co-consolidated (susceptorless) counterparts, but this was only significant for a confidence level of 80%. For 10 kg and 0 kg, susceptorless co-consolidated samples took more time than samples with susceptor. At 5 kg, the increase in excitation current (from 300.3 A to 499.8 A) for susceptorless samples inverts this trend. When comparing weight levels, it is clear that all types of samples require more time for disassembly at lower weight levels for the same excitation current. For susceptorless co-consolidated samples this trend was however not statistically significant between 15 kg and 10 kg. For co-consolidated samples with susceptor no analysis could be performed between 15 kg and 10 kg since only one sample with susceptor was successfully tested at 15 kg.

In figure 4.16b, the mean fraction of lap shear strength at room temperature that remains at a certain weight level is shown. Since this parameter is directly related to the applied force, which is set beforehand, statistical analysis makes little sense. The small differences between types of samples stem from the difference in room temperature lap shear strength (table 4.2) and small differences in overlap area. These differences in overlap area, which occur during manufacturing, were the reason that it was chosen to use the lap shear strength rather than disassembly force in the plot and table.

The mean disassembly temperature of the coil-facing side as recorded by the infrared camera is depicted in figure 4.16c. It was decided to use the FLIR measurements rather than those of TC1 because less values are missing. Additionally, the FLIR camera is not influenced by the strong electromagnetic field at the coil-facing surface, although there are other uncertainties involved (see chapter 5). No successful measurement was obtained with the camera for samples with susceptor at 15 kg, hence the missing blue bar. Susceptorless samples reach a lower surface temperature on the coil-facing side than ultrasonically welded samples at



(a) Disassembly time

(b) LSS fraction

(c) FLIR temperature

(d) Opposite thermocouple temperature

Figure 4.16: Mean and standard deviation of different disassembly parameters

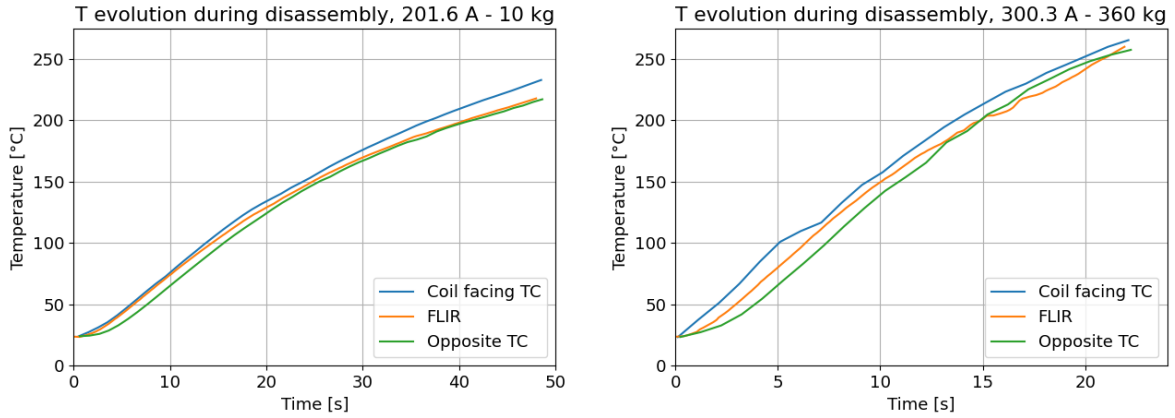
the highest current level (0 and 5 kg). At 10 kg, this analysis was not possible for welded samples (only one measurement available) and at 15 kg, this trend is reversed for unclear reasons. Comparing co-consolidated samples was only possible at 10 kg. It is clear that at this weight level, co-consolidated samples with mesh reach a significantly lower surface temperature at the thermocouple location than susceptorless samples. Comparison between weight levels shows that decreasing the weight level generally leads to an increased surface temperature reached upon disassembly, except for susceptorless co-consolidated samples between 10 and 5 kg. However, this could be attributed to the increased excitation current between those levels.

The last plot of figure 4.16, figure 4.16d, shows the mean and standard deviation of the temperature as recorded by the thermocouple on the side opposite to the coil (TC2). Susceptorless co-consolidated samples reach a higher temperature at TC2 than their counterparts with susceptor on all levels, although no analysis was possible at 15 kg. On the other hand, no significant difference between the temperatures of ultrasonically welded samples and susceptorless co-consolidated samples at 5 kg and 0 kg were detected. For all types of samples, a higher temperature at the coil-opposing side is reached with decreasing weight level. This was tested for ultrasonically welded samples between 5 kg and 0 kg, for co-consolidated samples with susceptor from 10 kg to 5 kg and 5 kg to 0 kg and for susceptorless co-consolidated samples for all steps.

Another interesting element of the disassembly process is the temperature evolution with time. This is shown for all types of samples at the different excitation current levels in figures 4.17 to 4.19. For susceptorless samples – both co-consolidated and welded – the temperature levels off after a certain time due to the change in material properties of the composite laminates. Carbon fibres' electrical conductivity decreases, which results in a decrease in excited current and subsequent decrease in heating. The metal mesh of samples with

susceptor partially counteracts this effect. Additionally, the heat development in this type of samples is much faster for the same excitation current (see figure 4.17b versus 4.18a). Even at 0 kg, the sample with susceptor breaks before any levelling of the temperature can occur.

Some peculiarities of the temperature evolution deserve more explanation. In subfigures 4.18a, the measurement of the coil facing thermocouple seems to jump quickly to a high temperature. The graph was recorded with the latest set of thermocouples (double asterisk in table 4.4). This thermocouple could be more sensitive to an electromagnetic field because it used longer wires and the wires were less tightly wound together at the weld.

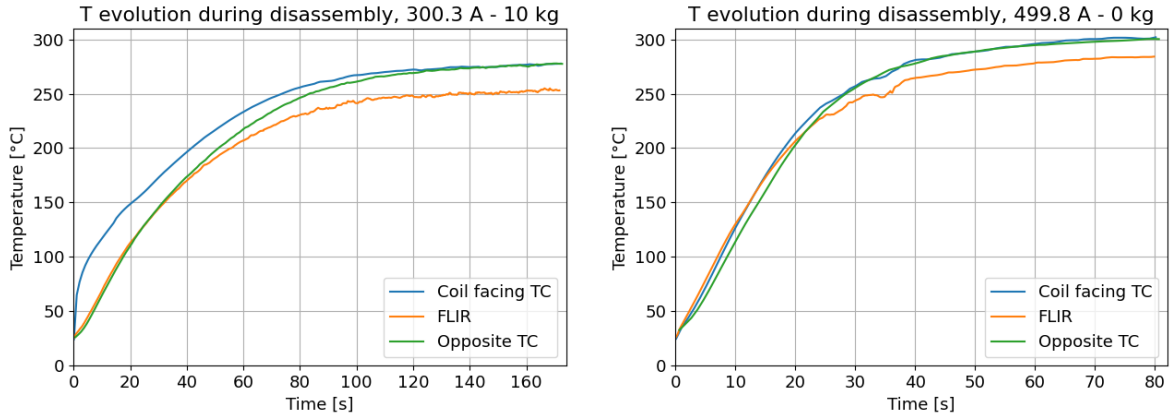


(a) 201.6 A - 10 kg - with susceptor

(b) 300.3 A - 0 kg - with susceptor

Figure 4.17: Evolution of temperature vs. time during disassembly for co-consolidated samples with susceptor (TC wire diameter 1 mm)

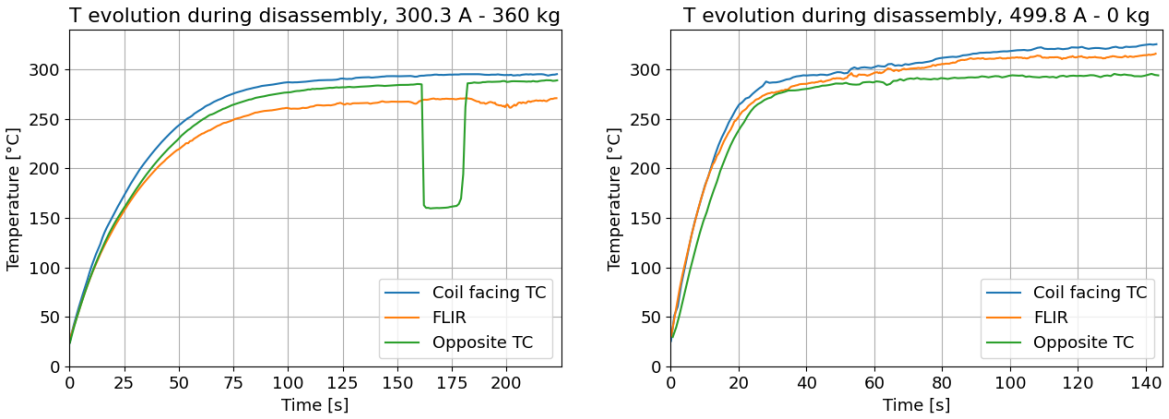
Another peculiarity that is especially visible in figures 4.18a, 4.18b and 4.19a is that the infrared camera levels off at a lower temperature than the thermocouples. This could be attributed to two causes: the infrared camera has no error induced by the induction field and the kapton tape used to fix the thermocouples on the sample could influence measurements. Under this kapton tape, at the location of the thermocouple, an air bubble is unavoidable. Upon heating, this air bubble expands, causing a different reflection which influences the infrared measurement.



(a) 300.3 A - 10 kg

(b) 499.8 A - 0 kg

Figure 4.18: Evolution of temperature vs. time during disassembly for the co-consolidated samples without susceptor (TC wire diameter 1 mm)



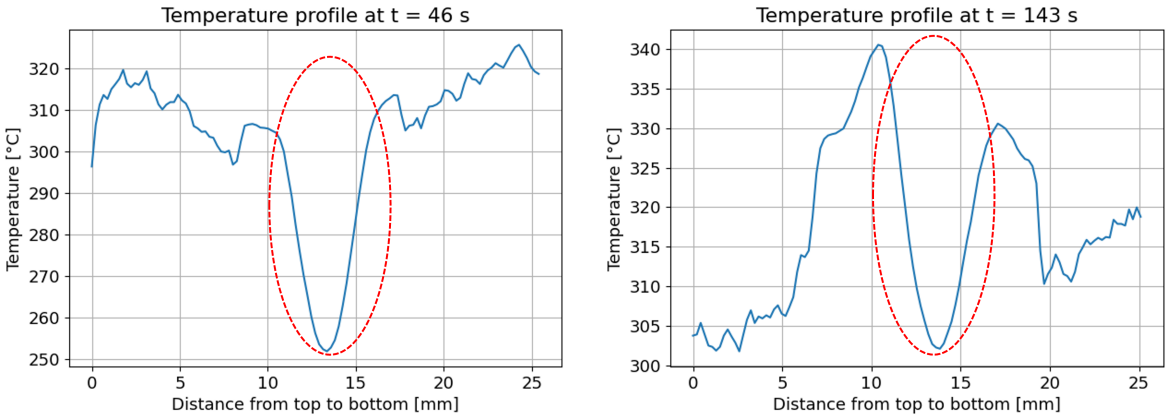
(a) 300.3 A - 10 kg

(b) 499.8 A - 0 kg

Figure 4.19: Evolution of temperature vs. time during disassembly for ultrasonically welded samples (TC wire diameter 1 mm)

The last remark to be made about temperature evolution concerns subfigure 4.19a. In that figure, the thermocouple opposing the coil suddenly recorded a lower temperature value for about 15 seconds, to then return to a similar level as recorded before. It is unknown why this happened, but in the subsequent test run, the thermocouple wire snapped upon fracture of the sample. Possibly the sensor was damaged already, resulting in the faulty measurement. Since the temperature measurement at fracture was again at the same level as before this erratic behaviour, it was decided to keep using this experiment in analyses.

To conclude the results of the disassembly process, figure 4.20 shows the temperature profile across the coil-facing surface as recorded by the infrared camera. For co-consolidated samples, the edge effect as predicted by the model is visible (figure 4.20a), both for samples with and without susceptor: the temperature decreases gradually to the centre of the surface. At the centre, marked with a red dashed ellipse, a sudden dip in the temperature is visible. This dip is probably caused by an air bubble present under the kapton tape. For ultrasonically welded samples, however, there seems to be no edge effect. Here, the start of the kapton tape is actually characterized by a sudden increase in temperature. A clear dip in temperature, again caused by an air bubble, is indicated in this figure.



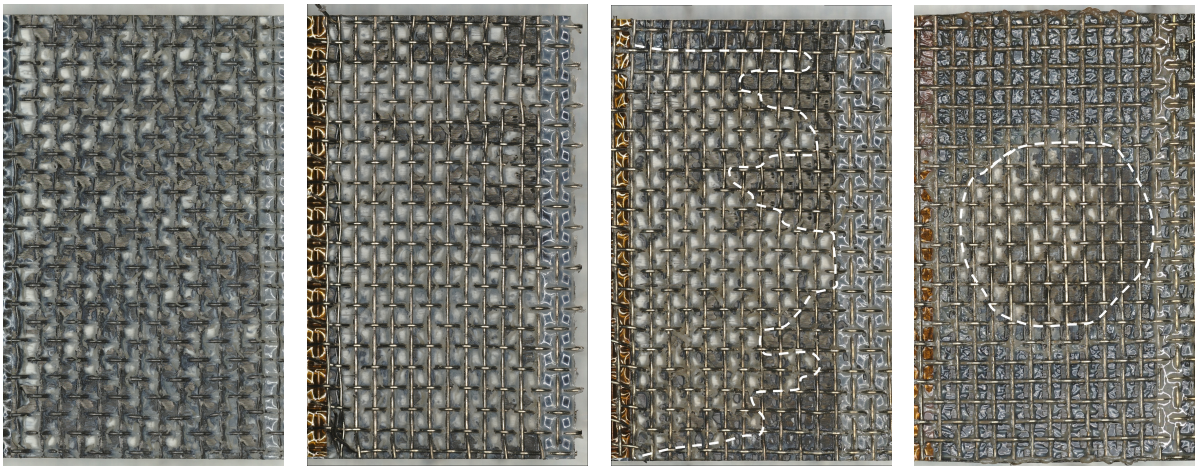
(a) 499.8 A - 0 kg - without susceptor

(b) 499.8 A - 0 kg - ultrasonically welded

Figure 4.20: Temperature profile across the coil-facing surface. The temperature dip caused by an air bubble under the kapton tape is marked with a red dashed line.

Fracture surfaces

The fracture surfaces of co-consolidated samples with susceptor are depicted in figure 4.21. It is interesting to note that from left to right, the amount of opaque white PEEK spots between the mesh diminishes. At 10 kg, they appear uniformly over the surface (figure 4.21b). One load level lower, the white spots disappear at the edges and for 0 kg, they only appear in a circle at the centre of the fracture surface.



(a) 15 kg - 201.6 A **(b)** 10 kg - 201.6 A **(c)** 5 kg - 201.6 A **(d)** 0 kg - 300.3 A

Figure 4.21: Fracture surfaces of co-consolidated samples with susceptor for different weight-excitation current combinations. In figure (c) and (d), white dashed lines mark the area in which white PEEK spots appear. In figure (a) and (b) these spots appear all over the surface.

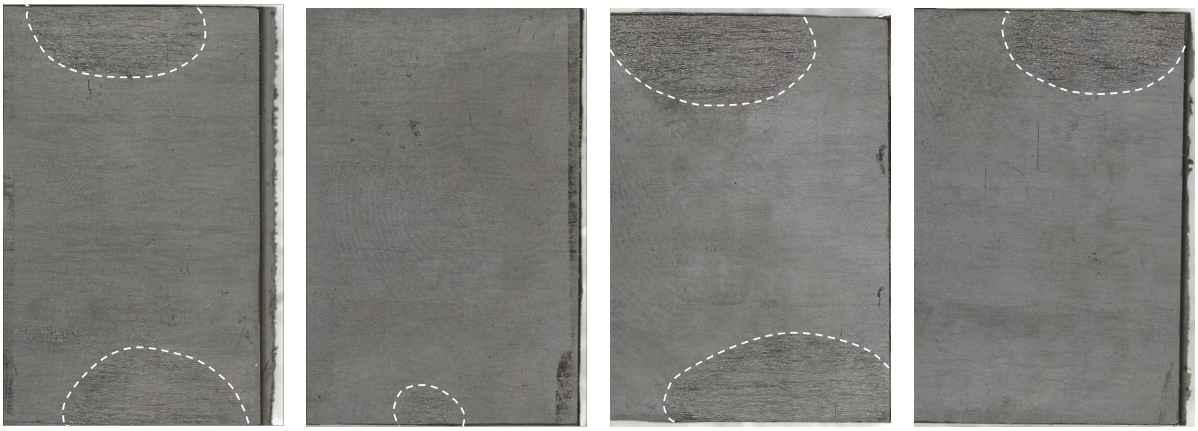
Figure 4.22 shows the fracture surfaces at different weight levels for susceptorless co-consolidated samples. The first two surfaces reveal little to no damage at all. From 5 kg onward, a different texture on the surface can be identified. The areas marked with a white dashed line reflect light differently than the middle of the fracture surface. On both the coil-facing and coil-opposing sample surface, similar spots were detected (figure 4.23). On the coil-facing surface, two large spots could be identified from 5 kg onward. On the opposing surface, only one spot was visible, bigger in size for a lower weight.



(a) 15 kg - 300.3 A **(b)** 10 kg - 300.3 A **(c)** 5 kg - 499.8 A **(d)** 0 kg - 499.8 A

Figure 4.22: Fracture surfaces of co-consolidated samples without susceptor for different weight-excitation current combinations. The white dashed lines mark areas with a different reflection.

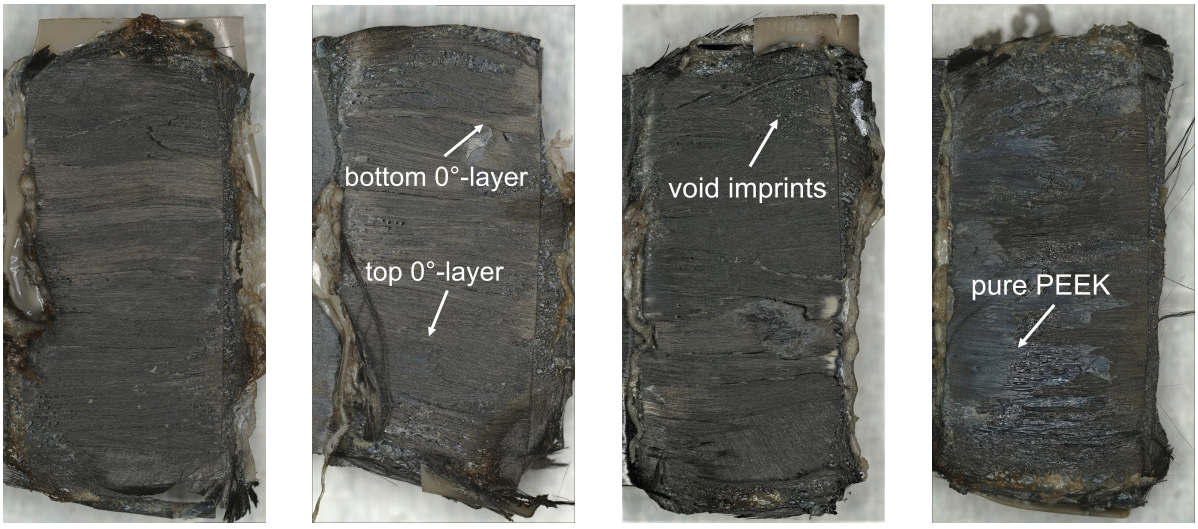
The fracture surfaces of ultrasonically welded samples are given in figure 4.24. Due to the nature of the welding process of narrow coupons, fibre distortion can be seen for all weight levels. It is hard to identify differ-



(a) 5 kg - 499.8 A - coil facing **(b)** 5 kg - 499.8 A - opposite **(c)** 0 kg - 499.8 A - coil facing **(d)** 0 kg - 499.8 A - opposite

Figure 4.23: Sample surfaces of co-consolidated samples without susceptor for 5 kg and 0 kg. The white dashed lines mark areas that reflect light differently.

ences in the surfaces. All surfaces show fracture in different layers: both 0°-layers near the fracture surface can be seen at the same time. This is especially clear in figure 4.24b, where the different textures in the picture are caused by two different layers that are visible. Void imprints are also visible in all cases, but it is likely that these voids were already formed during welding. The 0 kg case (figure 4.24d) has traces of pure PEEK polymer at the interface itself. On the coil-facing adherend, spots that reflect light differently could again be identified, while on the coil-opposing surface no such spots were detected. Figure 4.25 shows an area with different reflection for an unbroken sample.



(a) 15 kg - 300.3 A **(b)** 10 kg - 300.3 A **(c)** 5 kg - 499.8 A **(d)** 0 kg - 499.8 A

Figure 4.24: Fracture surfaces of ultrasonically welded samples for different weight-excitation current combinations. Pure PEEK only occurs in subfigure (d). Other features indicated are visible in all figures, but only shown in one.

Microscopic images of cross-section

Images of the cross-section of all disassembled samples were taken with a Keyence confocal microscope. Only one sample per joint type per weight level will be shown in this report. Pictures of other samples can be found in Appendix D.

If thermal damage occurred during disassembly, the damage was always most profound at the edges of the sample due to the edge effect. For co-consolidated samples the evolution of damage is therefore best shown

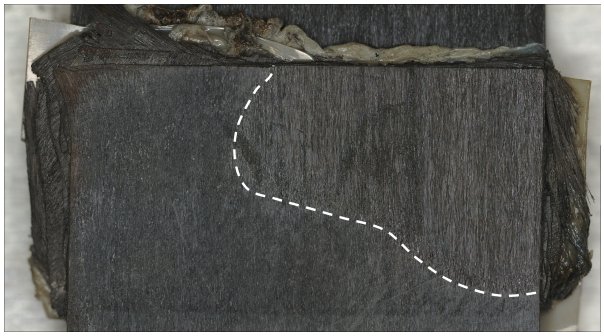
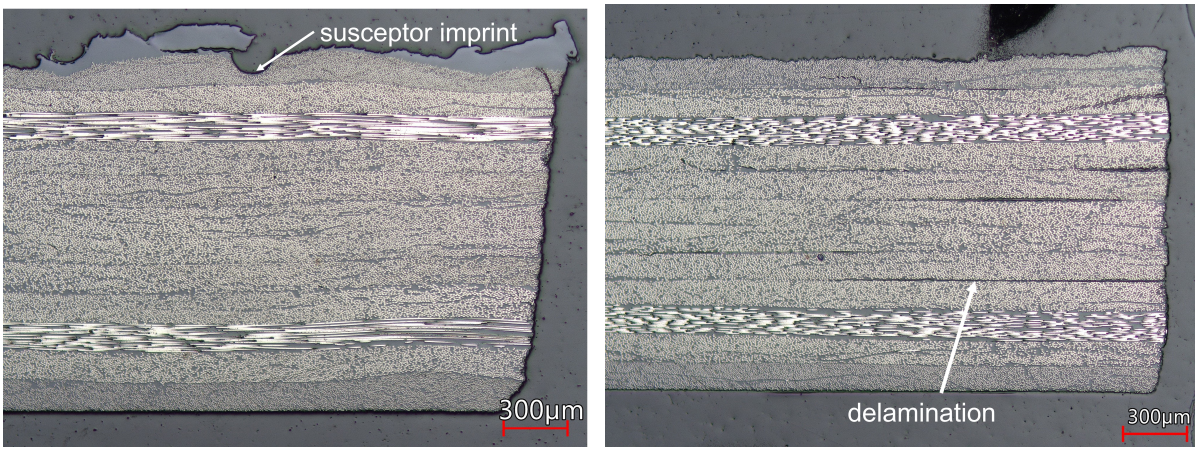


Figure 4.25: Spot with different light reflection (indicated with white dashed line) on the coil-facing adherend of an unbroken sample tested at 0 kg - 499.8 A

by depicting the edge of a sample for different weight-excitation current combinations, as will be done with the help of figures 4.26 to 4.29. A wider area will also be shown to compare damage throughout the sample (figure 4.31). The damage evolution for ultrasonically welded samples is also shown by depicting wider areas of the cross-section (figure 4.32). The welding process of narrow composite laminates made of unidirectional tapes with a large sonotrode causes fibre distortion and, more importantly, thermal damage at the edges of the coupon. This thermal damage makes it impossible to detect damage inflicted during disassembly by only looking at the edges.

Co-consolidated samples with susceptor show no damage after disassembly at 15 kg (~4.8 kN), except for the fracture line itself and the imprint left by the susceptor (figure 4.26a). For samples without susceptor, only one edge of one sample showed delaminations (see figure 4.26b and table 4.4). All other cases were completely undamaged.

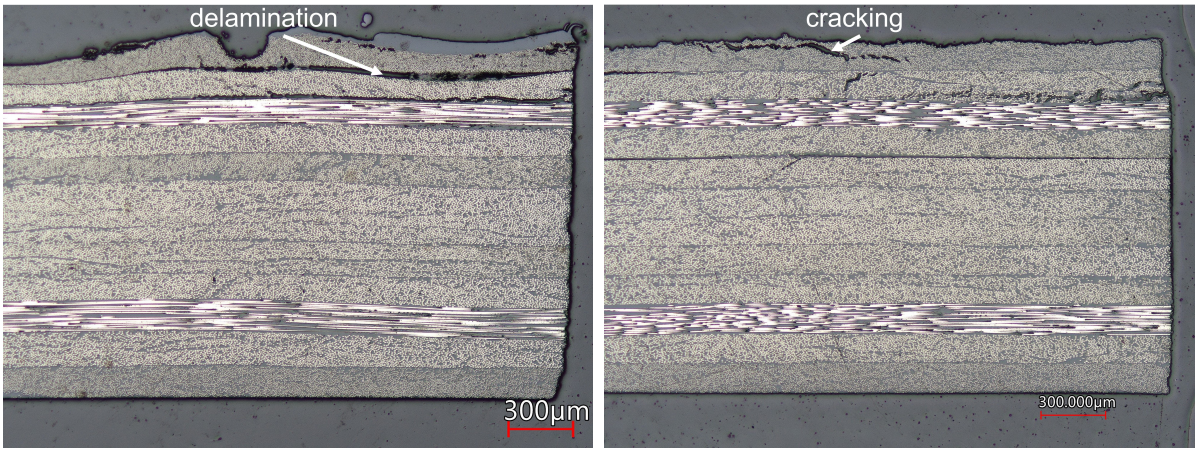


(a) 201.6 A, with susceptor **(b)** 300.3 A without susceptor

Figure 4.26: Edge of the cross-section of a disassembled sample for 15 kg

At 10 kg (~3.3 kN), some damage inflicted during disassembly is visible for both types of samples. The sample with susceptor (figure 4.27a) suffered delaminations between the first three layers at the joint interface. There was only one sample with susceptor at this load level which showed any damage (table 4.4). All other samples with susceptor were undamaged. The damaged sample had a longer overlap, which could possibly have aggravated the edge effect. The susceptorless sample shown in figure 4.27b again shows delaminations. Some cracking in the first two layers near the interface is also visible. All susceptorless samples disassembled at this weight level showed comparable damage.

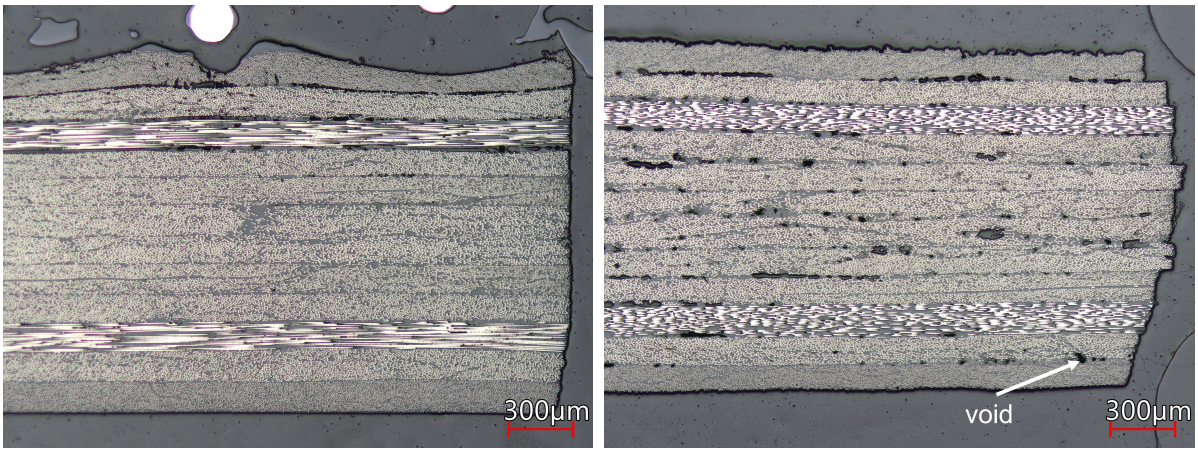
One weight level lower, at 5 kg (~1.8 kN), the damage in both types of samples is more extensive. Figure 4.28a shows similar damage to figure 4.27a, but damage has penetrated into the laminate and even between



(a) 201.6 A, with susceptor **(b)** 300.3 A, without susceptor

Figure 4.27: Edge of the cross-section of a disassembled sample for 10 kg

the fourth and fifth layer some voids are visible. Now, all but one sample with susceptor showed damage originating from the disassembly process, ranging from delaminations to voids throughout the thickness. Thermally inflicted voids also occur throughout the thickness of the susceptorless sample (figure 4.28b), and at some places voids line up to form a delamination between layers. The damage is much more extensive due to the increased excitation current. However, a sample that failed to break at 5 kg with an excitation current of 300.3 A already showed some voids throughout the thickness (figure 4.30). The more extensive damage is therefore not solely caused by the current increase.

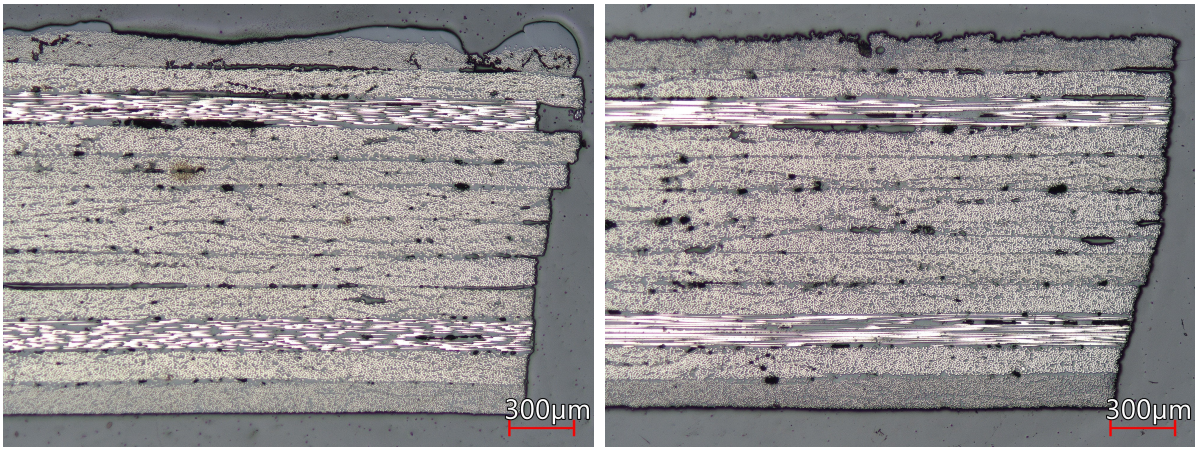


(a) 201.6 A, with susceptor **(b)** 499.8 A, without susceptor

Figure 4.28: Edge of the cross-section of a disassembled sample for 5 kg

On the lowest weight level (0 kg or 450 N), damage is extensive for both types of samples and occurs throughout the thickness of the sample. Both voids and delaminations are visible. A big difference with the previous load level is visible for the sample with susceptor (figure 4.29a) due to the increased excitation current amplitude, while for the susceptorless sample there is almost no noticeable difference.

The full half of a cross-section of both types of samples is shown in figure 4.31. Cuts were made at the centre of the joint, and can be identified as the straight edges on the left-hand side of the pictures. For both samples, the damage primarily occurs at the edge and diminishes towards the centre of the joint. There is a difference in the way this damage fades. For a susceptorless sample, the damage diminishes uniformly throughout the thickness (figure 4.31b): the last damage appears both close to the interface and at the sample's surface. For the sample with susceptor, the closer to the joint interface the later damage disappears (figure 4.31a).



(a) 300.3 A, with susceptor **(b)** 499.8 A, without susceptor

Figure 4.29: Edge of the cross-section of a disassembled sample for 0 kg

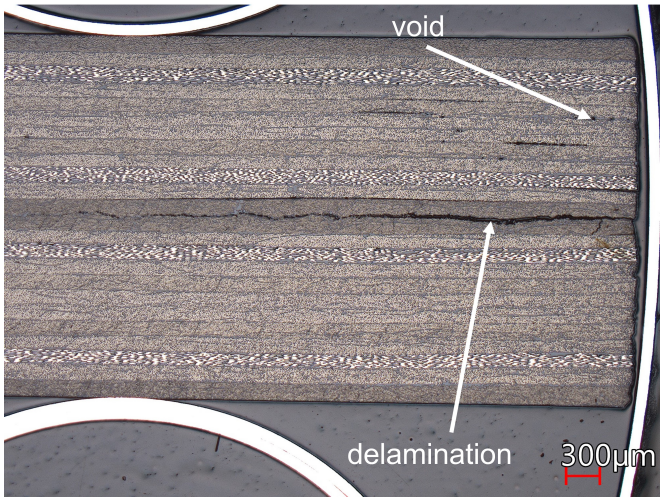
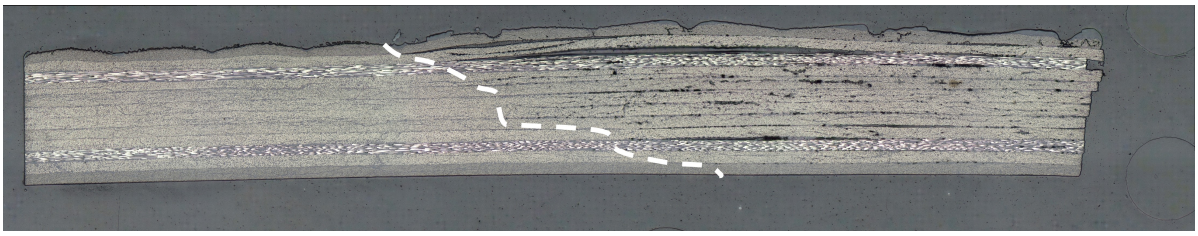
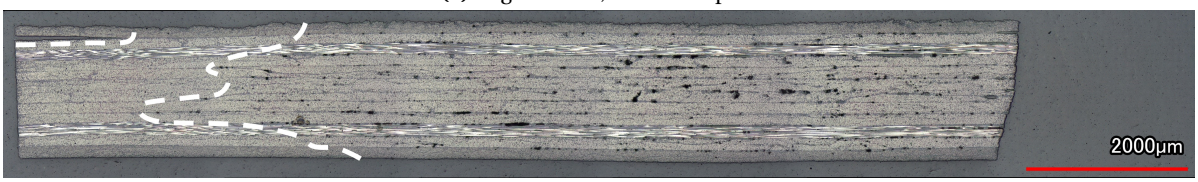


Figure 4.30: Unbroken susceptorless sample, tested at 300.3 A and 5 kg



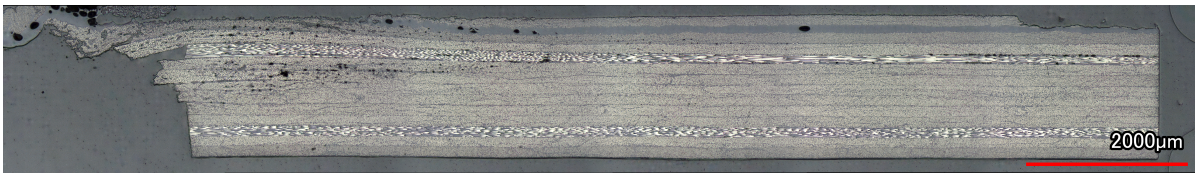
(a) 0 kg - 300.3 A, with susceptor



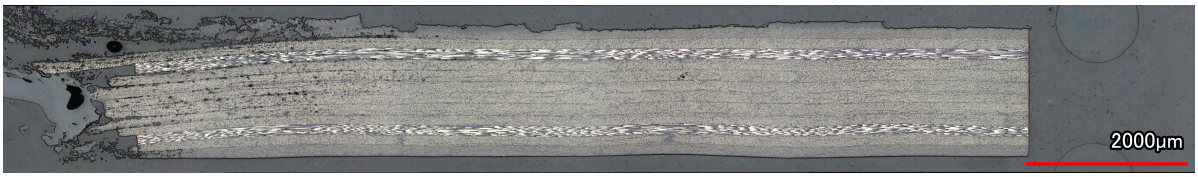
(b) 0 kg - 499.8 A without susceptor

Figure 4.31: Full cross-section of both types of co-consolidated samples. The white dashed lines mark the border of the damaged area.

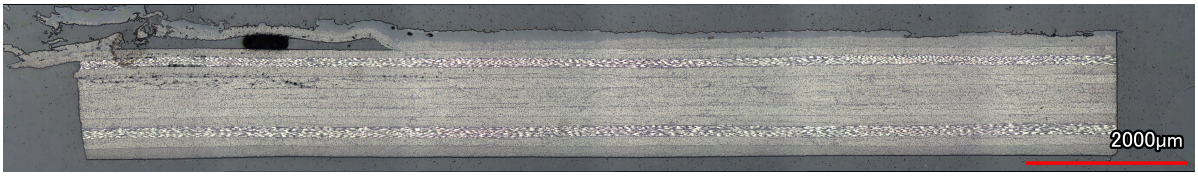
Ultrasonically welded samples are already damaged at the edges due to the welding process itself. It is therefore of little use to compare the edges of the sample. A full picture of half the cross-section of samples disassembled 15 kg and 10 kg as well as for a sample fractured at room temperature is visible in figure 4.32. For all these samples, damage occurs mainly at the edge. There is no apparent difference between the cross-sections of the disassembly experiments and the cross-section of the test at room temperature.



(a) Room temperature test



(b) 15 kg - 300.3 A

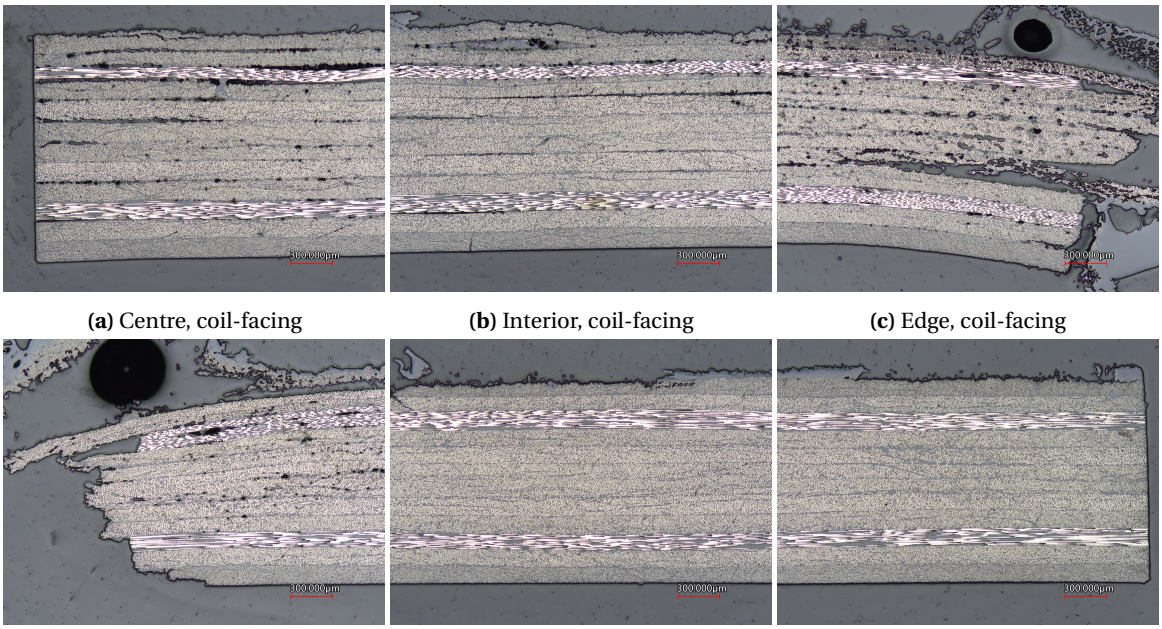


(c) 10 kg - 300.3 A

Figure 4.32: Full cross-section of ultrasonically welded samples disassembled at different weight-excitation current combinations

At lower weight levels, the excitation current was increased to 499.8 A. Now, damage starts to become visible. Since the compilation of the full image of the cross section went wrong for the sample disassembled at 5 kg, three separate pictures from the edge, interior and centre are given in figure 4.33. For proper comparison, the same was done for the sample disassembled at 0 kg (figure 4.35). Some parts of the full cross-sections are therefore not shown, but the three images combined give a good overview.

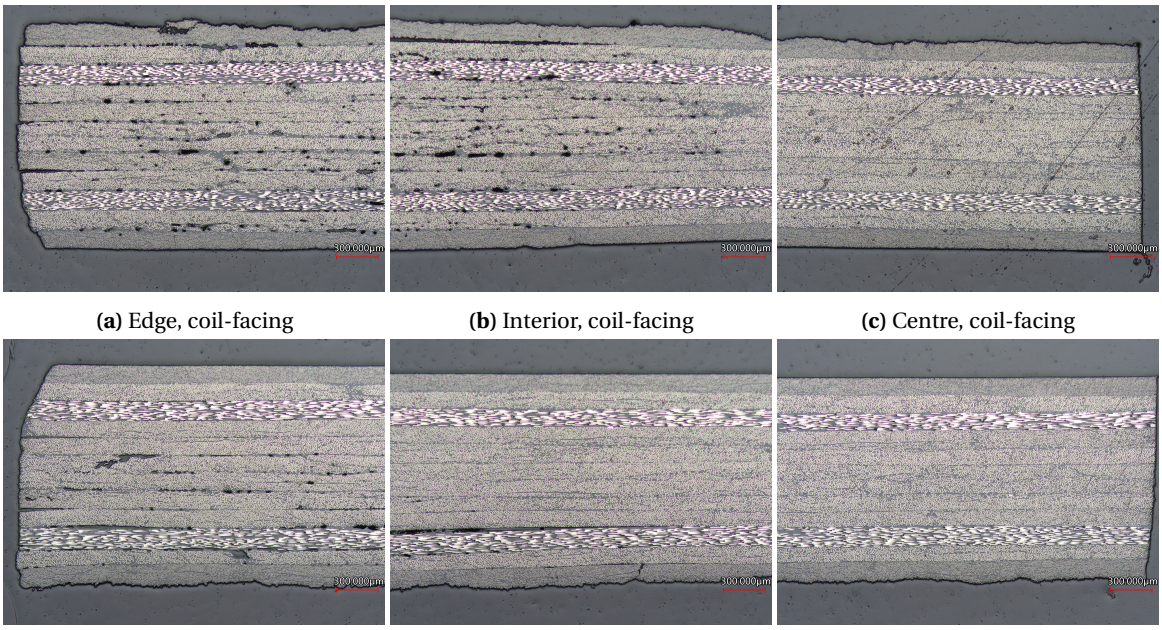
At 5 kg, there are now differences in damage between the coil-facing and coil-opposing adherend. While the coil-facing adherend is clearly damaged, the coil-opposing adherend of the same sample was relatively unscathed (figure 4.33). This contrasts with susceptorless co-consolidated samples disassembled at the same weight and excitation current level. Figure 4.34 clearly shows that for this type of specimen, the coil-opposing adherend is damaged as well. For the ultrasonically welded sample disassembled at 0 kg and 499.8 A, damage occurs on both the coil-facing and coil-opposing adherend (figure 4.35).



(a) Centre, coil-facing **(b)** Interior, coil-facing **(c)** Edge, coil-facing

(d) Edge, coil-opposing **(e)** Interior, coil-opposing **(f)** Centre, coil-opposing

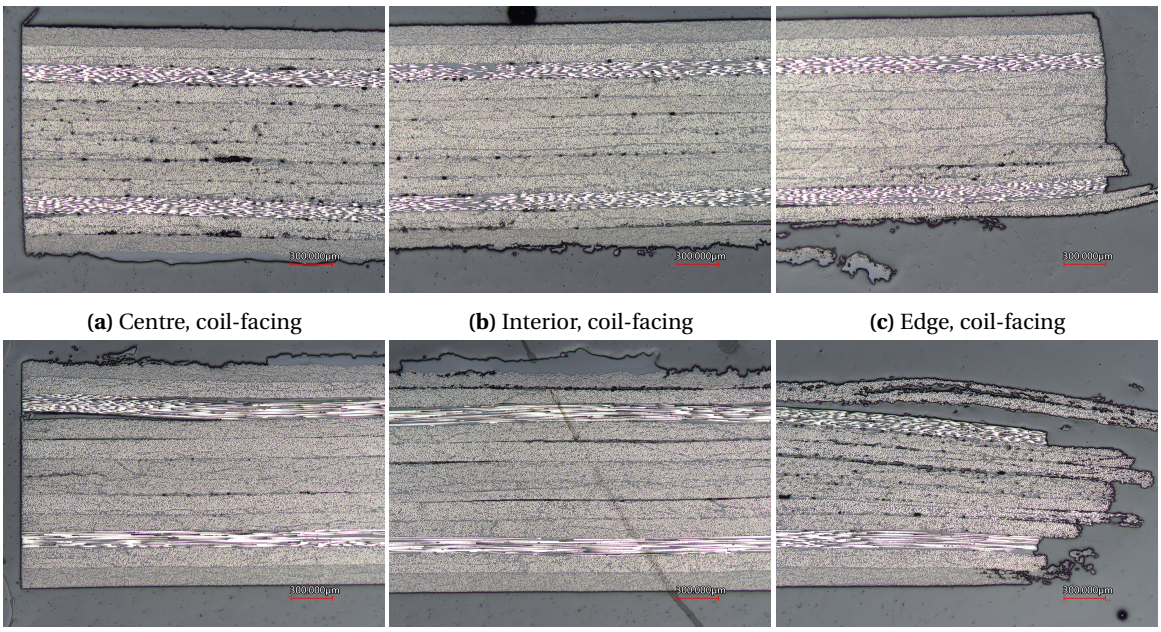
Figure 4.33: Cross-sections of an ultrasonically welded sample disassembled at 5 kg and 499.8 A



(a) Edge, coil-facing **(b)** Interior, coil-facing **(c)** Centre, coil-facing

(d) Edge, coil-opposing **(e)** Interior, coil-opposing **(f)** Centre, coil-opposing

Figure 4.34: Cross-sections of a co-consolidated sample without susceptor disassembled at 5 kg and 499.8 A



(a) Centre, coil-facing **(b)** Interior, coil-facing **(c)** Edge, coil-facing

(d) Centre, coil-opposing **(e)** Interior, coil-opposing **(f)** Edge, coil-opposing

Figure 4.35: Cross-sections of an ultrasonically welded sample disassembled at 0 kg and 499.8 A

5

Discussion

In this chapter, the results gathered and outlined in chapter 4 will be interpreted in order to answer the research questions. The research question along with its sub-questions are repeated here for good understanding:

How can induction heating be used to lower the required force for disassembly of fusion bonded thermoplastic composite joints, while minimizing damage to the joined parts inflicted during disassembly?

To help solve this question, multiple sub-questions can be formulated:

1. What is the effect of a metal mesh susceptor on the disassembly process and disassembly-related damage?
   (a) How effectively can the susceptor focus heating?
   (b) How are the disassembly characteristics, such as time and temperature, affected by the presence of the susceptor when applying a fixed excitation current and disassembly force?
   (c) What is the effect of the susceptor on the type and extent of damage?
2. How does the type of fusion bonding process (ultrasonic welding versus co-consolidation) affect the disassembly process and disassembly-related damage?
   (a) How are the disassembly characteristics, such as time and temperature, affected by the type of fusion bonded joint when applying a fixed excitation current and disassembly force?
   (b) What is the effect of the type of fusion bonded joint on the type and extent of damage?

Some comments about the validity of results gathered will be formulated after answering these questions. Lastly, ideas on how to proceed with investigations of this disassembly method will be proposed.

5.1. Influence of the susceptor on disassembly of co-consolidated joints

The first aspect that was investigated was disassembly of co-consolidated joints. A susceptor was included in some samples. Theoretically, this susceptor should focus heating at the interface, which could facilitate the disassembly process and affect damage patterns. In this section, it will be evaluated whether this indeed occurred.

5.1.1. Heat focusing

Prior to experiments, it was attempted to assess the effectiveness of the metal mesh susceptor in focusing heat at the interface by building a model. With the material parameters as calculated in chapter 3, it appeared that this effectiveness was rather limited. However, model validation showed that the assumptions made during these calculations were incorrect. After adjusting the electrical conductivity of both the susceptor layer and the composite laminate to fit the surface temperature evolution as recorded during disassembly experiments,

the model seemed to predict good heat focusing by the metal mesh susceptor (see figure 4.10a and 4.10b). It is however questionable how accurate this prediction is. As discussed in section 4.1.2, increasing only the electrical conductivity in the susceptor layer might not give results that resemble reality. It is however very difficult to validate the temperature evolution through the thickness of the sample experimentally, as thermocouples included in the susceptor layer would influence induction heating of the interface itself.

It was tried to confirm heat focusing by the susceptor with the experimental data available. To this end, individual results of the reference case and disassembly experiments were plotted together in a scatterplot (figure 5.1), depicting lap shear strength (normalized over the lap shear strength at room temperature) versus the temperature at fracture. During reference testing, samples were heated up uniformly in a temperature chamber. In contrast, induction heating during disassembly should result in non-uniform heating. For samples with susceptor, successful heat concentration would imply that the interface is at a higher temperature than the sample's coil-facing surface. It should therefore break at lower surface temperatures than reference case samples. If the trendlines of the reference case shown in figure 5.1 are extrapolated to higher temperatures, this behaviour is indeed visible. For co-consolidated samples without susceptor, however, the effect is even more outspoken. The different temperature ranges of the reference case and the disassembly experiments also makes direct comparison complicated, as the decrease in strength of polymers with increasing temperature is not necessarily linear [25]. Therefore, no conclusions about heat focusing can be drawn from figure 5.1.

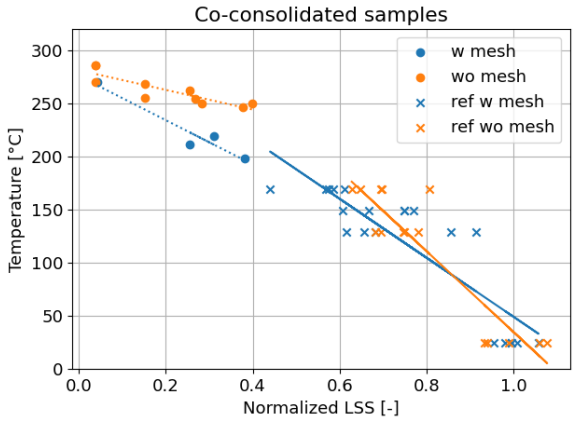


Figure 5.1: Comparison of reference case experiments with disassembly experiments. The lap shear strength (LSS) is normalized with the mean lap shear strength at room temperature for each sample type. Disassembly temperatures depicted were recorded by the FLIR camera.

An additional problem to confirm heat focusing by the susceptor is the limited amount of temperature data for the coil-facing surface that was acquired during disassembly. Figure 4.16c seems to suggest that the mean coil-facing temperatures of samples with susceptor are lower than their susceptorless counterparts. However, only at 10 kg two measurements were successful. Other weight levels have only one or even no data points. It is therefore hard to conclude anything about the effectiveness of the susceptor directly from the raw experimental data. The model results confirm heat focusing by the susceptor, but it is unsure how accurate these predictions are. Some qualitative proof of heat focusing by the susceptor was found when experimental data and damage patterns were processed further. This will be addressed in sections 5.1.2 and 5.1.3.

5.1.2. Influence of the susceptor on the disassembly characteristics

From the first experiments onward, it was clear that samples with susceptor heated up much more easily than susceptorless samples. As a consequence, a lower excitation current was needed to disassemble samples with susceptor. Trials with the same excitation current as for susceptorless samples resulted in thermal damage, even at the highest weight level.

Direct comparison of the required disassembly time is complicated by the fact that samples with susceptor cannot withstand excitation currents used for susceptorless samples without suffering damage. If it is tried

to compare co-consolidated samples with and without susceptor from figure 4.16a, no unambiguous conclusion can be drawn due to the result at 5 kg. This is the only case for which samples with susceptor took longer to disassemble, but the excitation current for these samples is almost 300 A lower.

A much more fair comparison can be made when the excitation current is taken into account. To this end, disassembly energy per unit of coil impedance ($I^2 \cdot t$) is calculated and plotted in figure 5.2. In this figure, it is clearly visible that co-consolidated samples with susceptor need considerably less energy input than their susceptorless counterparts. All trends were again analysed and confirmed with t-tests (Appendix C). The grey shaded area of figure 5.2 marks the energy-weight combinations for which damage occurred. However, there were outliers in both directions: one sample with susceptor tested at 5 kg was undamaged, while a sample of the same type tested at 10 kg and a susceptorless sample tested at 15 kg were damaged (see table 4.4).

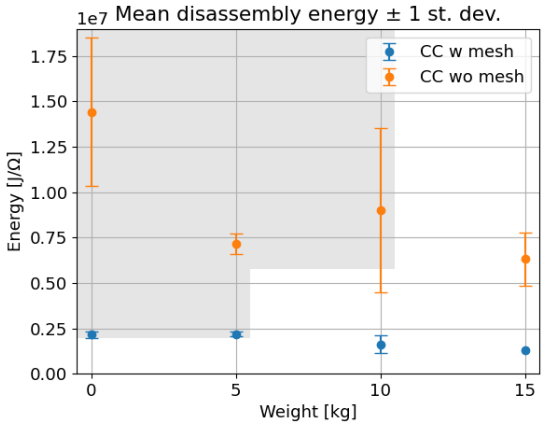


Figure 5.2: Comparison of disassembly energy per unit of coil impedance for co-consolidated samples with and without susceptor. The grey shaded area marks the energy-weight combinations which resulted in thermal damage.

Significantly less energy is required for disassembly of co-consolidated joints with susceptor, which could indicate that the energy for this case is used much more efficiently. This could imply that the susceptor focuses the energy, and therefore heating, at the joint interface, locally weakening the joint up to the point of fracture. However, it should be taken into account that the reference case results (table 4.2) proved that joints with a susceptor embedded at the interface are weaker from the start, which also diminishes the energy required for disassembly.

Another difference between the two types of co-consolidated joints regarding disassembly energy, but also regarding disassembly time (figure 4.16a), is the much smaller standard deviations of samples with susceptor. Apparently, the susceptor diminishes scatter in disassembly energy and time, which could make disassembly of joints with susceptor a more predictable process.

From the temperature measurements taken during disassembly, it becomes apparent that the surfaces of samples with susceptor reach less high temperatures than susceptorless samples (figures 4.16c and 4.16d). For the coil-facing side, however, few measurements are available for samples with susceptor. At the coil-opposing side, more measurements are available and samples with susceptor reach a lower temperature for all cases. This could be attributed to the lower excitation current required.

The temperature evolution at the sample surfaces (figure 4.17 and 4.18) also show clear differences. For susceptorless samples, the temperature levels off due to the changes in the laminate's properties (decreasing electrical conductivity and increasing heat capacity). For samples with susceptor, the metal mesh either compensates this change in laminate properties or causes fracture before this phenomenon can happen. It can be seen that the susceptor causes accelerated heating of the sample, especially when comparing figures with the same excitation current (figure 4.17b versus figure 4.18a). Since susceptorless samples take almost one minute longer to reach the same temperature as samples with susceptor, it can be concluded that the sus-

ceptor generates heat much faster than the composite material. This could point towards successful heat concentration.

From all these results, joints with susceptor overall seem to perform better regarding disassembly. They require less energy, lower excitation currents can (and should) be used and less scatter in disassembly time occurs. An important note to make, however, is that the reference case pointed out that a joint with susceptor is weaker at room temperature. This can possibly be attributed to bad bonding of PEEK polymer to the metal mesh, which would cause stress concentrations at this interface. Moreover, it could negatively impact the fatigue life of these joints [9]. The fatigue behaviour was not researched for this thesis.

5.1.3. Influence of the susceptor on damage patterns

Samples' surfaces and fracture surfaces were inspected immediately after disassembly. For samples with susceptor, it was noted that the amount of white PEEK spots on the fracture surface decreases when the weight level decreases (figure 4.21). The whiteness of these PEEK spots could be caused by crystalline regions within the polymer, which diffract light differently than amorphous material. In that case, the disappearance of these spots could be attributed to local melting. Upon melting, the crystals in the polymer disappear, rendering the polymer amorphous and therefore transparent. When the sample breaks, the surfaces are exposed to air and cool down quickly, preventing recrystallization. Figure 4.21d clearly shows that melting occurs first at all edges.

The fracture surfaces of susceptorless samples showed spots with different light reflection on low weight levels (5 kg and 0 kg, figure 4.22), where fibres are better distinguishable from each other. Again, it is believed that these marks are created by a changing opacity of the PEEK polymer when local melting occurs. The marks only appear at two of the four edges of the overlap (figure 4.22d). This could imply that heat at the other two edges can be evacuated through the rest of the laminate material. The markings differ from the pattern visible for a co-consolidated sample with susceptor (figure 4.21d). The susceptor causes melting at all four edges of the overlap, close to where the metal mesh stops. This could indicate that the mesh heats up more significantly than the laminate, which makes it impossible for all heat to be evacuated through the laminate material.

At low weight levels (5 kg and 0 kg), the coil-facing and coil-opposing surfaces of susceptorless also showed spots with a different light reflection (figure 4.23), comparable to the spots visible on the fracture surfaces (figure 4.22). Again, these spots could be attributed to local melting at the edges. The pattern differs from the model prediction seen in figure 4.9, which predicted that the vertical edges on the right side of each subfigure of figure 4.23 would reach the same temperature as the upper and lower sides. Possibly the orientation of the top layer (0°) helped to quickly evacuate heat from the surface of this edge.

For samples with susceptor, only the coil-facing surface showed a spot with different light reflection at 0 kg, similar to the coil-opposing side of susceptorless samples at the same weight level (figure 4.23d). Due to the lower excitation current used for the tests with susceptor, it appears that the surfaces of these samples are less marked.

The cross-sections of both types of joints showed two kinds of damage: voids and delaminations. The voids can be attributed to volatiles and moisture entrapped in the laminate. These impurities expand upon heating, especially when the melting temperature is reached [34]. The delaminations are probably either caused by the application of the disassembly force on the weakened polymer interfaces or by the lining up of voids in between the laminate layers.

There is no real distinction between damage types of samples with and without susceptor. The damage distribution, however, does show differences. In figure 4.31, a wider cross-section of both types of co-consolidated samples was shown. Figure 4.31a shows that when moving from the cross-section's right edge to the left, the damage disappears first at the coil-facing surface and last at the interface of the sample with susceptor. The sample without susceptor shows a more random damage pattern (figure 4.31b). This difference could point towards successful heat concentration by the susceptor.

Another difference between samples with and without susceptor is the weight levels at which damage occurred. This was shown in figure 5.2 and table 4.4. At 10 kg, only one sample with susceptor was damaged.

For susceptorless samples, damage was found on all cross-sections. It is worth noting that in principle, a lower excitation current could be used for samples with susceptor, but it was chosen to use the same excitation current for as many weight levels as possible to simplify comparison of the results. A lower excitation current would probably cause even less damage than recorded in this study. Therefore, it seems that joints with embedded susceptor perform slightly better, meaning they suffer less damage at lower weight levels and therefore could reach larger reductions in disassembly force. This would be even more clear if an appropriate excitation current was applied.

Despite the seemingly better performance of samples with susceptor when it comes to damage, there are some disadvantages for processing after disassembly. An imprint left by the metal mesh is clearly visible in all cross-sections, which could hinder reuse of undamaged samples. Additionally, for most samples the mesh remained stuck within PEEK polymer at one of the two fracture surfaces. For reprocessing an extra step could be required to remove the mesh from that adherend.

5.2. Influence of fusion bonding process type

After disassembly of co-consolidated joints, disassembly of a different kind of fusion bonded joints was tested. The proposed method was tried for ultrasonically welded joints. Due to differences in joint layout, differences in the disassembly process were identified. The damage inflicted during disassembly was also compared, despite difficulties because of damage caused by welding of the joints.

5.2.1. Influence of the joint type on the disassembly characteristics

In general, the disassembly process of ultrasonically welded samples appeared less straightforward than for co-consolidated samples. For most weight levels, considerably more time was required for disassembly (figure 4.16a) and a higher surface temperature was reached at the coil-facing side (figure 4.16c). Only the mean value of the 15 kg weight level differs for unknown reasons. At the coil-opposing side, temperatures similar to the temperatures of susceptorless co-consolidated samples were recorded at fracture (figure 4.16d). The more difficult disassembly is emphasized by the fact that at 10 kg and 0 kg, almost half of the samples tested failed to break within 4 minutes, despite high temperatures being reached (table 4.4).

The disassembly energy for ultrasonically welded samples is plotted together with the energy required for susceptorless co-consolidated samples in figure 5.3. This time, no indication is given on damaged samples (as was done for figure 5.2). For most samples it was uncertain whether damage occurred during welding or disassembly. Figure 5.3 shows that the energy required to disassemble ultrasonically welded samples is significantly higher at all weight levels except for 15 kg. For 0 kg and 5 kg, the standard deviations are also wider, indicating more scatter. Important to mention is that samples that failed to break (at 0 kg and 10 kg) are excluded from this plot. Including these samples would further heighten the average energy values at these weight levels.

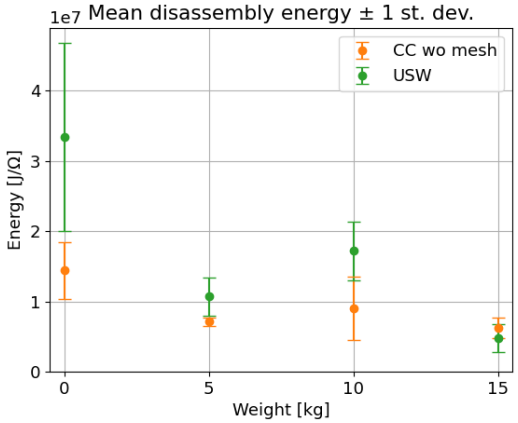


Figure 5.3: Comparison of disassembly energy per unit of coil impedance for co-consolidated samples without susceptor and ultrasonically welded samples

The higher energy required could be attributed to a more difficult heating process of the interface, caused by the pure polymer PEEK layer (originating from the energy director) that remains at the joint interface after welding. This layer acts as an electrical insulator, preventing currents from crossing the joint interface. Moreover, no heat is generated within this layer. The heating of the energy director remnant therefore relies solely on thermal conduction. The thermal conduction of PEEK is also very low, which could cause the interface to heat up more slowly. Therefore, it can be postulated that the joint is weakened less by induction heating than for co-consolidated joints. Combined with the variability in quality induced by the welding process, this could explain the failure to disassemble some of the samples at certain weight-excitation current combinations.

The temperature evolution registered on the sample surfaces (figure 4.19) is rather similar to that of co-consolidated samples without susceptor. Higher surface temperatures are reached faster, which is seemingly in contradiction with the theory that the interface heats up more slowly than for susceptorless co-consolidated samples. However, if less currents are generated due to the insulating PEEK layer at the interface, it could be that less electromagnetic shielding occurs. This would influence the thermocouple measurements. The high temperatures visible in figure 4.19 need to be maintained for a longer period of time before fracture occurs (compared to figure 4.18), which could indicate that more time is required to soften the pure PEEK polymer layer sufficiently for fracture.

Another difference in temperature recordings can be found in the infrared camera measurements across the coil-facing surface (figure 4.20). For a co-consolidated sample, the edge effect is visible: the temperatures are higher at the edges and decrease towards the centre of the surface. For ultrasonically welded samples, the trend is the opposite. The edges are at a lower temperature than the centre of the surface. This could be caused by the fibre squeeze-out, which can evacuate heat from the edges and increases the surface available for convection cooling. This could also impact the temperature inside the laminate. Fibres that are partially squeezed out could conduct heat from the inside of the laminate towards the surrounding air, which could have a cooling effect on the interior of the laminate. Moreover, fibres that are squeezed out at the interface do not contribute to the heating of that interface, which could again hamper heat development locally.

Additional effects that could make disassembly of ultrasonically welded joints harder were searched in the mechanical properties of the joint. The room temperature tests did however not reveal a statistically significant difference between the lap shear strength of welded and susceptorless co-consolidated samples. It is therefore believed that the more difficult disassembly is attributed mainly to differences in heating at the interface itself. It was not possible to verify this hypothesis experimentally, as thermocouples inserted at the interface would disturb local induction heating effects and therefore influence the heating itself.

5.2.2. Influence of the joint type on damage patterns

The same damage types as for co-consolidated samples were found for the ultrasonically welded samples: voids and delaminations. However, it was more difficult to compare fracture surfaces and cross-sections of different weight levels due to the nature of the welding process itself. Welding of small coupons with a sonotrode that has a similar width as the coupon itself results in thermal damage and fibre and resin squeeze-out at the edges. It also results in distorted fibres, void imprints and sometimes small burnt areas on the fracture surfaces. It is therefore hard to tell what damage is caused by disassembly and what damage is caused by ultrasonic welding.

The fracture surfaces of ultrasonically welded samples disassembled at different load levels all have similar features, except for the 0 kg load case (figure 4.24). For that case, the fracture surface more clearly shows pure PEEK remnants, indicating fracture within the energy director rather than between the energy director and the composite layers or between composite layers themselves. If the disassembly process indeed caused fracture purely at the interface, this could be very beneficial for reuse of the adherends. However, this also requires no damage to be found throughout the thickness of the samples.

Damage was found on all cross-sections of ultrasonically welded samples. For 15 kg and 10 kg, the damage was comparable to damage found in the room temperature case (figure 4.32). Samples disassembled at 5 kg and 0 kg did however show more extensive damage than the room temperature case, possibly because of the switch to the higher excitation current (499.8 A instead of 300.3 A).

At 5 kg voids and delaminations are visible throughout the whole cross-section of the coil-facing adherend, while the coil-opposing adherend only shows damage comparable to the room temperature case (4.32a). The resemblance could indicate that damage on the coil-opposing adherend was already created during welding. If none of this damage was created during disassembly, this contrasts with susceptorless co-consolidated samples disassembled at 5 kg. For these samples, the coil-opposing adherend also showed damage inflicted during disassembly (4.34). Due to the absence of an insulating layer at the interface, the excited currents in the coil-facing adherends can travel through both adherends of the co-consolidated joints. This could in turn have caused damage in both adherends. For welded samples, the eddy currents generated in the coil-facing adherend can not travel to the coil-opposing adherend. Only locally excited eddy currents, which are smaller due to the larger coupling distance, can cause damage. This could explain the difference in damage between the two types of fusion bonded joints. It is however important to note that it is not entirely sure that all damage visible in figure 4.33d was caused during welding.

At 0 kg, both the coil-facing and coil-opposing adherend showed damage. The longer heating times allowed for more heat generation in the coil-opposing adherend as well, and heat transfer throughout the full sample could have played a larger role. Both effects result in a higher temperature in the coil-opposing adherend, which causes the thermal damage visible in figure 4.35.

5.3. Answering the main research question

From the answers to the sub-questions presented above, the main research question can now be answered. It appears that induction heating is very successful in lowering the required force: the minimum force that could be applied by the experimental setup was reached for all sample types. This came however at the expense of thermal damage in the samples below a certain weight level. For both types of co-consolidated samples, induction heating could lower the lap shear strength to around 37% of the original lap shear strength without inflicting thermal damage, except for one outlier for susceptorless samples. For samples with susceptor, it could be possible to go to lower load levels when adjusting the excitation current to a lower value. This was however not done to facilitate comparison between load levels. Ultrasonically welded samples were more complicated to disassemble aided by induction heating, possibly because excited current and therefore heating is obstructed by the insulating pure PEEK energy director remnant at the joint interface. Additionally, more time could be required to soften this extra polymer layer. To properly analyse damage inflicted during disassembly, it would be necessary to investigate different types of welded samples, such as larger coupons with welds far from the edge. That way, damage on the edges inflicted during welding would be eliminated, facilitating detection of damage inflicted during disassembly.

5.4. Validity of results

In this section, some thoughts about the validity of the results will be addressed. First, sources of scatter in the experimental data will be described, together with their influence on the trends and conclusions found in this research. Subsequently, some suggestions on practical applications and how to make experiments more closely related to these potential applications will be made.

5.4.1. Sources of uncertainty in measurements

Two main sources of uncertainty in the trends discovered for the disassembly process can be identified: the first source relates to uncertainty in the measurements, the second source stems from the way samples were manufactured. A smaller source of scatter is the positioning of the sample with respect to the coil. Lastly, there is some uncertainty on the damage reported in this study, as this can be a very local phenomenon.

In chapter 3 it was proven that the induction field influences the K-type thermocouple measurements. These thermocouples were used because of their availability in the lab. If the excitation current would have stayed the same for all cases, this would be a minor issue, but this was practically impossible due to the requirements of the different types of samples. Changing the excitation current changes its effect on the thermocouples, and it is therefore difficult to directly compare the recorded temperatures. Since the FLIR infrared camera confirmed most trends, comparisons were still made across different current settings. However, even the FLIR measurements pose a reason for concern, as was described in the results (chapter 4): the air bubble expanding under the kapton tape could locally influence the reflection of heat towards the camera and therefore influence temperature measurements. Using E-type thermocouples, as is done in industry, could be

beneficial to obtain more accurate temperature measurements.

The second source of scatter comes from manufacturing of the samples. As was reported in chapter 4, it is difficult to control the overlap area of the co-consolidated samples with the manufacturing procedure that was used. This was taken into account when describing trends, but trends would be much clearer if the overlap were to be the same. Co-consolidating plates with a bigger overlap and subsequently machining them to the correct size might produce more equal samples. For ultrasonically welded samples, the scatter is intrinsically bigger, even though the fixture used creates a more or less standard overlap. The manufacturing scatter was addressed by testing multiple samples per weight level. Damage patterns were only shown for one sample per type per weight level in the report, but pictures of other samples can be found in Appendix D.

Another, smaller source of uncertainty stems from the disassembly process itself. The model made in COMSOL revealed that the induction heating process was very sensitive to the sample position with respect to the induction coil. The frame that was built to hold the induction coil was completely rigid and did not allow for movement of the coil without moving the frame itself. Beforehand it was assumed that this would help reducing scatter due to positioning, but due to scatter in specimen sizes the whole frame needed to be moved for some samples. All positioning was done using a metal spacer to ensure the correct coupling distance, but eccentricity of the sample was less straightforward to control and could therefore introduce small errors. In figure 4.8, the model prediction showed that the temperature deviated 40°C after only 11 seconds for an eccentricity of 4 mm for samples without susceptor and -4 mm for a sample with susceptor. As the overlap did not always go up to the adherend's edge due to the manufacturing procedure, eccentricity could be one of the causes of some scatter in disassembly time. A setup with a mechanism that allows for fine tuning of the coil position would decrease the effects of possible mispositioning, while a machining procedure as described in the previous paragraph would solve the issue of variations in overlap position.

The last uncertainty originates from the way damage was investigated. A cross-section of broken samples was made, in such a way that the critical edges according to the model were cut in half. Nevertheless, damage is only investigated in this cross-section, and large areas of the adherends remain hidden in these pictures. For samples with visible surface damage, it was made sure that this damage was included in the cross-section, but for other, now reportedly undamaged samples, small voids and delaminations could be present for different cross-sections.

5.4.2. Practical applications

This research focused on simple, flat, single-lap joints. In aircraft, many joints are much more complicated than what was tested for this study. Brackets, stringers and clips are nowadays produced from thermoplastic composites for the most recent commercial aircraft [7], and welding of these parts to the fuselage would present numerous benefits (as stated in chapter 2). However, these parts would be welded with either multiple spot welds or a longer, welded seam, which could follow a curved path.

To resemble real-life disassembly, single lap shear tests might not be the best option. In figure 5.4, a simple sketch of the disassembly of an L-shaped stiffener fusion bonded to a composite plate is shown. To effectively disassemble this continuous connection, it would be necessary to move the coil slowly along the length of the connection. Meanwhile, it seems most logical to pull the stringer directly away from the plate. This would however induce peel stresses rather than shear stresses. Therefore, it could be more realistic to use a peeling force to disassemble integrated parts. Moreover, fusion bonded joints are less resistant to peel stresses than to shear stresses. When testing this type of joints in peel, what is essentially tested is the through-the-thickness strength of the composite adherends. This strength is much lower for laminate materials, as no fibres are reinforcing the thickness. The shear loads used in this research are therefore larger than what would be required as a peeling force. Disassembly in peel might thus be easier for real-life applications.

In figure 5.4, the coil is sketched beneath the plate to avoid collision with the stringer when this stringer is pulled away from the plate. This layout entails different boundary conditions than the conditions present in the tests of this study. The edge effect would be less severe in this case, which could be beneficial: most damage found in this study seemed to be related to this edge effect. Furthermore, there are many aircraft parts in which the weld would not go up to the edge of the sample. It could therefore be interesting to investigate joints in which the weld or fusion bonded zone is further away from the edge of the sample.

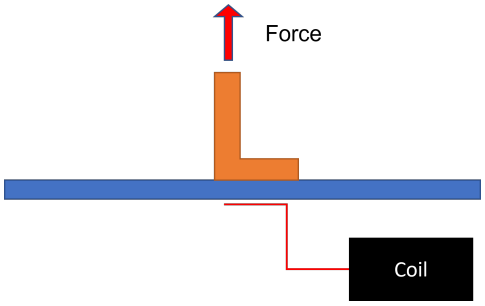


Figure 5.4: Example of possible application: the disassembly of an L-shaped stringer fusion bonded to a plate

It is also a possibility that the plate in figure 5.4 would be a curved fuselage panel. In that case, the coil design as sketched in the figure and used in this study would create non-uniform heating due to a non-uniform coupling distance. Different coil designs might be required. However, it would be very impractical to have many different coils for many different aircraft parts.

One last remark about practical applications concerns the susceptor. The specific susceptor used in this study simplified the disassembly, but also weakened the joint at room temperature and might influence fatigue life. This raises two possibilities. The first one is to change the type of susceptor, for instance to a carbon fibre mesh with higher fibre density than the laminate itself. This could be beneficial for reuse or recycling, as no foreign material is included in the laminate. However, such a susceptor could also be less effective in heat focusing, especially in carbon-fibre reinforced laminates that already have a high fibre volume content. A second option is to further develop the process for joints that have an embedded metal mesh anyway, such as resistance welded joints.

6

Conclusions & recommendations

This study investigated disassembly of fusion bonded joints aided by induction heating through an induction heating model and disassembly experiments. Single lap shear testing while applying induction heating showed that through this method, the disassembly force could be lowered significantly. Beyond a reduction of 37% of the original lap shear strength, induction heating induced thermal damage in most of the disassembled coupons, mainly due to overheating of the sample's edges. More detailed conclusions are listed below, following the same structure as the sub-questions of the main research question:

1. The inclusion of a metal mesh susceptor in co-consolidated joints proved to be beneficial for disassembly. Damage patterns and the model built pointed towards successful heat concentration, although quantification was not possible. A lower excitation current was required for disassembly. The process was generally faster, used less energy and reached less high surface temperatures upon fracture. However, the susceptor also weakened the joint at room temperature.

   At low load levels, both thermally induced voids and delaminations were found for both samples with and without susceptor, although in a slightly different pattern. For samples with susceptor, damage deeper into the laminate first appeared near the interface, while for susceptorless samples it appeared simultaneously throughout the thickness. This could point toward successful heat concentration.

   The concentration of heat caused by the susceptor could be used to lower the excitation current applied beyond what was tried in this study, which would in turn cause less thermal damage in samples with susceptor. However, the susceptor leaves a clear imprint in the fracture surface and the metal mesh often remained stuck in the PEEK polymer on one adherend. This could complicate post-processing of disassembled samples.

2. Disassembly of ultrasonically welded joints appeared to be more challenging. This was mainly attributed to the pure PEEK energy director remnants at the joint interface, which formed a barrier for excited currents and therefore frustrated heating locally. Additionally, the need to soften this extra layer of pure polymer could have caused the longer disassembly times. For some load-excitation current combinations, half of the samples did not break within the specified time of four minutes.

   The damage patterns in ultrasonically welded samples were more complicated to evaluate, as the ultrasonic welding process used in this study already caused thermal damage at the coupon's edges. Only for the highest excitation current used, clear damage was inflicted during disassembly.

The validity of these conclusions was shortly evaluated by assessing some possible sources of error and scatter. It was noted that temperature measurements in an induction field were rather complicated to carry out, as the induction field influenced the thermocouple's measurements. Additionally, scatter was introduced

during manufacturing, in the form of variations in the overlap area for all types of joints. Using better manufacturing and sensing equipment could benefit a more accurate confirmation of the trends discovered in this study.

To conclude this research, some ideas about potential applications revealed possibilities for further research. These recommendations are listed below:

- For more complex parts, such as stringers, clips, or stiffeners, disassembly with induction heating could be tried by applying peel forces rather than shear forces. Fusion bonded joints are generally weaker in peel and application of a peel force might be more practical for real-life disassembly.
- As damage mainly occurred due to the edge effect, changing boundary conditions by testing bigger plates with joints further from the edge might induce completely different damage patterns or even no damage at all for lower loads.
- Different types of susceptors could be investigated. The inclusion of a susceptor benefited the disassembly process, but the specific susceptor used in this study also weakened the joint at room temperature. Carbon fibre susceptors, such as thin-ply laminates or woven meshes with a higher fibre volume content than the adherends, might reduce this negative effect at room temperature. However, these solutions might also be less effective in focusing heat within a carbon fibre reinforced laminate with high fibre volume content.
- Alternatively, the method investigated in this study could be developed further by focusing on joints that already have an embedded metal mesh, such as resistance welded joints.

A

Model equations

A more extensive derivation of some model parameters will be given in this appendix. The thermal and electrical conductivity as well as the volume fractions of the susceptor layer will be addressed. Subsequently, the equations solved by COMSOL in the different physics domains will be further detailed.

A.1. Susceptor material model derivation

A.1.1. Thermal and electrical conductivity

In-plane

From figure 3.2, the following equations can be derived for the equivalent in-plane resistive network (figure 3.3) [42]:

$$R_{s1} = \frac{\frac{gd}{2}}{k_s \frac{\pi d}{4g} S} = \frac{2g^2}{\pi k_s S} \tag{A.1}$$

$$R_{p1} = \frac{S - 2\frac{gd}{2}}{k_p S \frac{\pi d}{4g}} = \frac{4gS - 4g^2 d}{\pi k_p S d} \tag{A.2}$$

$$R_{s2} = \frac{S}{k_s \frac{\pi d}{4g} \frac{gd}{2}} = \frac{8S}{\pi k_s d^2} \tag{A.3}$$

$$R_{p2} = \frac{S}{k_p \frac{\pi d}{4g} (S - 2\frac{gd}{2})} = \frac{4gS}{\pi k_p (S - gd) d} \tag{A.4}$$

$$\frac{1}{R_{tot}} = \frac{1}{2R_{s1} + R_{p1}} + \frac{2}{R_{s2}} + \frac{1}{R_{p2}} \tag{A.5}$$

And:

$$\frac{1}{R_{tot}} = k_{eq,xy} \frac{2\frac{\pi d}{4g} S}{S} = k_{eq,xy} \frac{\pi d}{2g} \tag{A.6}$$

Equating equations A.5 and A.6 and solving for $k_{eq,xy}$ delivers the value for the equivalent thermal conductivity. For electrical conductivity, it suffices to change all k with σ.

Through-the-thickness

From figure 3.2 and figure 3.4, equations for the through-the-thickness resistances can be derived:

$$\frac{1}{R_{tot}} = \frac{4}{R_{s,e} + R_{p,e}} + \frac{4}{R_{s,c}} + \frac{1}{R_{p,b}} \tag{A.7}$$

$$\frac{1}{R_{tot}} = k_{eq,z} \frac{S^2}{\frac{2\pi d}{4g}} = k_{eq,z} \frac{2gS^2}{\pi d} \tag{A.8}$$

with:

$$R_{s,c} = \frac{\frac{2\pi d}{4g}}{k_s\left(\frac{gd}{2}\right)^2} = \frac{2\pi d}{k_s g^3 d^2} \tag{A.9}$$

$$R_{s,e} = \frac{\frac{\pi d}{4g}}{k_s\left(S-2\frac{gd}{2}\right)\frac{gd}{2}} = \frac{\pi d}{2k_s(S-gd)g^2 d} \tag{A.10}$$

$$R_{p,e} = \frac{\frac{\pi d}{4g}}{k_p\left(S-2\frac{gd}{2}\right)\frac{gd}{2}} = \frac{\pi d}{2k_p(S-gd)g^2 d} \tag{A.11}$$

$$R_{p,b} = \frac{\frac{2\pi d}{4g}}{k_p\left(S-2\frac{gd}{2}\right)^2} = \frac{\pi d}{2k_p g\left(S-gd\right)^2} \tag{A.12}$$

$$\tag{A.13}$$

Solving equations A.7 and A.8 for $k_{eq,z}$ (or $\sigma_{eq,z}$) delivers a result for the desired material properties.

A.1.2. Volume fractions of steel and polymer

The volume fractions of steel and polymer in the susceptor material model can be derived from the geometrical properties given in table 3.1 (remember that $g = \frac{\pi}{4}$):

$$V_{tot} = S^2 * 2\frac{\pi d}{4g} \tag{A.14}$$

$$V_{st} = 4 * \frac{\pi d}{4g} * \frac{gd}{2} * S \tag{A.15}$$

$$v_{st} = \frac{V_{st}}{V_{tot}} = \frac{dg}{S} \tag{A.16}$$

$$v_{pol} = 1 - v_{st} \tag{A.17}$$

A.2. Equations of the model physics

A.2.1. Magnetic fields interface

In the magnetic fields interface, the following equations are solved to calculate the magnetic field, induced current and subsequent magnetic and electric losses:

$$\mathbf{E} = -j\omega\mathbf{A} \tag{A.18}$$

$$\nabla \times \mathbf{H} = \mathbf{J} \tag{A.19}$$

$$\mathbf{B} = \nabla \times \mathbf{A} \tag{A.20}$$

$$\mathbf{J} = \sigma\mathbf{E} + j\omega\mathbf{D} \tag{A.21}$$

Together with the following constitutive relations:

$$\mathbf{B} = \mu_0\mu_r\mathbf{H} \tag{A.22}$$

$$\mathbf{J_c} = \sigma\mathbf{E} \tag{A.23}$$

$$\mathbf{D} = \epsilon_0\epsilon_r\mathbf{E} \tag{A.24}$$

In the above equations, $\mathbf{E}$ is the electric field, j the imaginary unit, ω the angular frequency of the field, $\mathbf{A}$ the magnetic vector potential, $\mathbf{H}$ the magnetizing field, $\mathbf{B}$ the magnetic field, $\mathbf{J}$ the current density, σ the conductivity of the material and $\mathbf{D}$ the electric displacement field. In the constitutive relations (A.22 to A.24) μ_0 is the magnetic permeability of vacuum and ϵ_0 the electric permittivity of vacuum, while μ_r and ϵ_r are the relative magnetic permeability and electric permittivity of the material, respectively. $\mathbf{J_c}$ is the conductive current density, or the current density minus the externally generated current density.

A.2.2. Heat transfer in solids interface

In the heat transfer in solids interface, the following equations are solved within the sample domain:

$$\rho c_p \frac{\partial T}{\partial t} + \rho c_p \mathbf{u} \cdot \nabla T + \nabla \cdot \mathbf{q} = Q + Q_{ted} \tag{A.25}$$

$$\mathbf{q} = -k \nabla T \tag{A.26}$$

In equations A.25 and A.26, ρ and c_p are the density and specific heat capacity of the material, T is the temperature and t the time, $\mathbf{u}$ is the fluid velocity vector, $\mathbf{q}$ the conductive heat flux, Q the heat of a heat source, Q_{ted} the thermoelastic damping and k the thermal conductivity of the material.

B

Sensitivity analysis

In this appendix, the temperature evolution for the original model and for variations of c_p and $\sigma_{in-plane}$ of the susceptor layer will be given for a time period of 20 seconds. The variations of these properties appeared to have an asymmetric influence in table 4.1 (together with ρ, but this has the exact same influence as c_p). However, this asymmetry disappeared for longer simulation times, as can be seen from the tables below.

Table B.1: Influence of variations of $\sigma_{in-plane}$ for 20 s simulation time

Original model		$\sigma_{\textbf{in-plane}} + \textbf{10\%}$		$\sigma_{\textbf{in-plane}} - \textbf{10\%}$	
t (s)	**T (°C)**	**T (°C)**	**difference (%)**	**T (°C)**	**difference (%)**
0	25.001	25.001	0.00	25.001	0.00
1	31.546	31.54	-0.02	31.551	0.02
2	39.973	39.969	-0.01	39.973	0.00
3	49.896	49.948	0.10	49.834	-0.12
4	61.686	61.365	-0.52	61.466	-0.36
5	74.355	73.73	-0.84	73.927	-0.58
6	87.876	87.007	-0.99	87.188	-0.78
7	101.89	101.04	-0.83	100.91	-0.96
8	116.41	115.8	-0.52	115.1	-1.13
9	131.16	130.86	-0.23	129.51	-1.26
10	145.98	146.07	0.06	143.98	-1.37
11	160.89	161.55	0.41	158.52	-1.47
12	175.86	177.3	0.82	173.12	-1.56
13	190.89	192.84	1.02	187.79	-1.62
14	205.76	208.3	1.23	202.29	-1.69
15	220.53	223.78	1.47	216.69	-1.74
16	235.25	239.27	1.71	231.04	-1.79
17	249.91	254.29	1.75	245.34	-1.83
18	264.11	269.06	1.87	259.2	-1.86
19	278.04	283.62	2.01	272.8	-1.88
20	291.72	297.96	2.14	286.17	-1.90

Table B.2: Influence of variations of c_p for 20 s simulation time

Original model		$\mathbf{c_p + 10\%}$		$\mathbf{c_p - 10\%}$	
t (s)	**T (°C)**	**T (°C)**	**difference (%)**	**T (°C)**	**difference (%)**
0	25.001	25.001	0.00	25.001	0.00
1	31.546	31.52	-0.08	31.576	0.10
2	39.973	39.902	-0.18	40.052	0.20
3	49.896	49.735	-0.32	50.072	0.35
4	61.686	61.368	-0.52	61.518	-0.27
5	74.355	73.846	-0.68	73.899	-0.61
6	87.876	87.146	-0.83	87.177	-0.80
7	101.89	100.92	-0.95	101.2	-0.68
8	116.41	115.19	-1.05	115.92	-0.42
9	131.16	129.68	-1.13	130.93	-0.18
10	145.98	144.23	-1.20	146.08	0.07
11	160.89	158.88	-1.25	161.48	0.37
12	175.86	173.59	-1.29	177.14	0.73
13	190.89	188.37	-1.32	192.59	0.89
14	205.76	202.99	-1.35	207.94	1.06
15	220.53	217.52	-1.36	223.31	1.26
16	235.25	232	-1.38	238.67	1.45
17	249.91	246.43	-1.39	253.57	1.46
18	264.11	260.42	-1.40	268.22	1.56
19	278.04	274.16	-1.40	282.65	1.66
20	291.72	287.66	-1.39	296.86	1.76

C

Welch's T-test

In this appendix, the testing procedure and results of the t-tests performed on the disassembly results will be detailed. The formulas, nomenclature and procedure are taken directly from the course book of Taerwe and De Belie [38].

According to Welch, the variable

$$Z = \frac{\overline{X} - \overline{Y} - \Delta}{\sqrt{S_X^2/n_X + S_Y^2/n_Y}} \tag{C.1}$$

approximately follows a t-distribution with ν degrees of freedom:

$$\frac{1}{\nu} = \frac{c^2}{\nu_X} + \frac{(1-c)^2}{\nu_y} \tag{C.2}$$

With:

$$c = \frac{S_X^2/n_X}{S_X^2/n_X + S_Y^2/n_Y} \tag{C.3}$$

$$\nu_X = n_X - 1 \tag{C.4}$$

$$\nu_Y = n_Y - 1 \tag{C.5}$$

In the above equations, the following symbols represent the following values:

- $\overline{X}$: average value of variable X
- $\overline{Y}$: average value of variable Y
- Δ: arbitrary number (depending on what needs to be tested)
- S_X: sample standard deviation of variable X
- S_Y: sample standard deviation of variable Y
- n_X: number of samples for variable X
- n_Y: number of samples for variable Y
- ν: number of degrees of freedom, rounded to the closest integer

To test the difference between two averages, the following assumptions are made:

- the variables are independent
- the variables are normally distributed

Δ is set to zero and the test depicted in table C.1 is performed.

Table C.1: T-test procedure

Hypotheses	**H_0 accepted if...**
$H_0 : \overline{X} = \overline{Y};\ H_1 : \overline{X} \neq \overline{Y}$	$-t_{\nu;1-\alpha/2} \cdot S^* \leq \overline{X} - \overline{Y} \leq t_{\nu;1-\alpha/2} \cdot S^*$
$H_0 : \overline{X} = \overline{Y};\ H_1 : \overline{X} < \overline{Y}$	$\overline{X} - \overline{Y} \geq -t_{\nu;1-\alpha} \cdot S^*$
$H_0 : \overline{X} = \overline{Y};\ H_1 : \overline{X} > \overline{Y}$	$\overline{X} - \overline{Y} \leq t_{\nu;1-\alpha} \cdot S^*$

Where

$$S^* = \sqrt{S_X^2/n_X + S_Y^2/n_Y} \tag{C.6}$$

and the t-value with the correct degree of freedom and the desired significance level α (confidence level equals $1-\alpha$) is taken from figure C.1.

Degrees of freedom (ν)	**Amount of area in one tail (α)**							
	0.0005	**0.001**	**0.005**	**0.010**	**0.025**	**0.050**	**0.100**	**0.200**
1	636.6192	318.3088	63.65674	31.82052	12.70620	6.313752	3.077684	1.376382
2	31.59905	22.32712	9.924843	6.964557	4.302653	2.919986	1.885618	1.060660
3	12.92398	10.21453	5.840909	4.540703	3.182446	2.353363	1.637744	0.978472
4	8.610302	7.173182	4.604095	3.746947	2.776445	2.131847	1.533206	0.940965
5	6.868827	5.893430	4.032143	3.364930	2.570582	2.015048	1.475884	0.919544
6	5.958816	5.207626	3.707428	3.142668	2.446912	1.943180	1.439756	0.905703
7	5.407883	4.785290	3.499483	2.997952	2.364624	1.894579	1.414924	0.896030
8	5.041305	4.500791	3.355387	2.896459	2.306004	1.859548	1.396815	0.888890
9	4.780913	4.296806	3.249836	2.821438	2.262157	1.833113	1.383029	0.883404
10	4.586894	4.143700	3.169273	2.763769	2.228139	1.812461	1.372184	0.879058
11	4.436979	4.024701	3.105807	2.718079	2.200985	1.795885	1.363430	0.875530
12	4.317791	3.929633	3.054540	2.680998	2.178813	1.782288	1.356217	0.872609
13	4.220832	3.851982	3.012276	2.650309	2.160369	1.770933	1.350171	0.870152
14	4.140454	3.787390	2.976843	2.624494	2.144787	1.761310	1.345030	0.868055
15	4.072765	3.732834	2.946713	2.602480	2.131450	1.753050	1.340606	0.866245
16	4.014996	3.686155	2.920782	2.583487	2.119905	1.745884	1.336757	0.864667
17	3.965126	3.645767	2.898231	2.566934	2.109816	1.739607	1.333379	0.863279

Figure C.1: T-distribution table [24]

A statistically significant difference is found when the null hypothesis H_0 is rejected and the alternative hypothesis H_1 is valid. Higher confidence levels (i.e. lower α), result in a wider range in which H_0 gets accepted. Less degrees of freedom have a similar effect. Both these effects can be seen from figure C.1, in which the t-values increase drastically with decreasing α and/or ν.

T-tests were performed to determine the significance of trends seen in figures 4.11, 4.16a, 4.16c, 4.16d, 5.2 and 5.3. The result of these tests is the confidence level with which the apparent trend was confirmed. These

results are listed in tables C.2 to C.6. In the tables, CC-w refers to a co-consolidated sample with suscptor, CC-wo to one without susceptor, USW to ultrasonically welded samples and RT to room temperature. A dash in the "Confidence" column indicates that the trend specified in the first column of the tabel could not be confirmed for a confidence level of at least 80%.

Table C.2: T-test results for trends in the reference case lap shear strength. A dash indicates that the trend specified in the left column was not significant for a confidence above 80%.

Lap shear strength reference case

Trend between sample types	**Confidence [%]**
CC-wo-RT > CC-w-RT	99
CC-wo-130°C > CC-w-130°C	80
CC-wo-170°C > CC-w-170°C	99
CC-wo-RT ≠ USW-RT	-

Trend between temperature levels	**Confidence [%]**
CC-wo-RT > CC-wo-130°C	99
CC-wo-130°C ≠ CC-wo-170°C	-
CC-w-RT > CC-w-130°C	99
CC-w-130°C ≠ CC-w-150°C	-
CC-w-150°C > CC-w-170°C	99

Table C.3: T-test results for trends in the disassembly time

Disassembly time

Trend between sample types	**Confidence [%]**
CC-wo-10kg > CC-w-10kg	90
CC-wo-5kg > CC-w-5kg	99
CC-wo-0kg > CC-w-0kg	95
CC-wo-15kg > USW-15kg	80
USW-10kg > CC-wo-10kg	90
USW-5kg > CC-wo-5kg	95
USW-0kg > CC-wo-0kg	90

Trend between weight levels	**Confidence [%]**
CC-wo-10kg > CC-wo-15kg	80
CC-wo-10kg > CC-wo-5kg	95
CC-wo-0kg > CC-wo-5kg	95
CC-w-5kg > CC-w-10kg	90
CC-w-5kg > CC-w-0kg	99
USW-10kg > USW-15kg	90
USW-10kg > USW-5kg	90
USW-0kg > USW-5kg	90

Table C.4: T-test results for trends in the FLIR temperature at fracture. A dash indicates that the trend specified in the left column was not significant for a confidence above 80%.

FLIR temperature at fracture

Trend between sample types	Confidence [%]
CC-wo-10kg > CC-w-10kg	99
CC-wo-15kg > USW-15kg	95
USW-5kg > CC-wo-5kg	90
USW-0kg > CC-wo-0kg	95

Trend between weight levels	Confidence [%]
CC-wo-10kg > CC-wo-15kg	90
CC-wo-5kg ≠ CC-wo-10kg	-
CC-wo-0kg > CC-wo-5kg	90
USW-0kg > USW-5kg	90

Table C.5: T-test results for trends in the TC2 temperature at fracture. A dash indicates that the trend specified in the left column was not significant for a confidence above 80%.

TC2 temperature at fracture

Trend between sample types	Confidence [%]
CC-wo-10kg > CC-w-10kg	99
CC-wo-5kg > CC-w-5kg	95
CC-wo-0kg > CC-w-0kg	90
CC-wo-15kg > USW-15kg	95
USW-5kg ≠ CC-wo-5kg	-
USW-0kg ≠ CC-wo-0kg	-

Trend between weight levels	Confidence [%]
CC-wo-10kg > CC-wo-15kg	95
CC-wo-5kg > CC-wo-10kg	90
CC-wo-0kg > CC-wo-5kg	90
CC-w-5kg > CC-w-10kg	95
CC-w-0kg > CC-w-5kg	95
USW-0kg > USW-5kg	90

Table C.6: T-test results for trends in the disassembly energy. A dash indicates that the trend specified in the left column was not significant for a confidence above 80%.

Disassembly energy

Trend between sample types	**Confidence [%]**
CC-wo-10kg > CC-w-10kg	99
CC-wo-5kg > CC-w-5kg	99
CC-wo-0kg > CC-w-0kg	99
CC-wo-15kg > USW-15kg	80
USW-10kg > CC-wo-10kg	95
USW-5kg > CC-wo-5kg	95
USW-0kg > CC-wo-0kg	90

Trend between weight levels	**Confidence [%]**
CC-wo-10kg > CC-wo-15kg	80
CC-wo-10kg > CC-wo-5kg	80
CC-wo-0kg > CC-wo-5kg	95
CC-w-5kg > CC-w-10kg	90
CC-w-5kg ≠ CC-w-0kg	-
USW-10kg > USW-15kg	99
USW-10kg > USW-5kg	95
USW-0kg > USW-5kg	90

D

Microscopy and damage

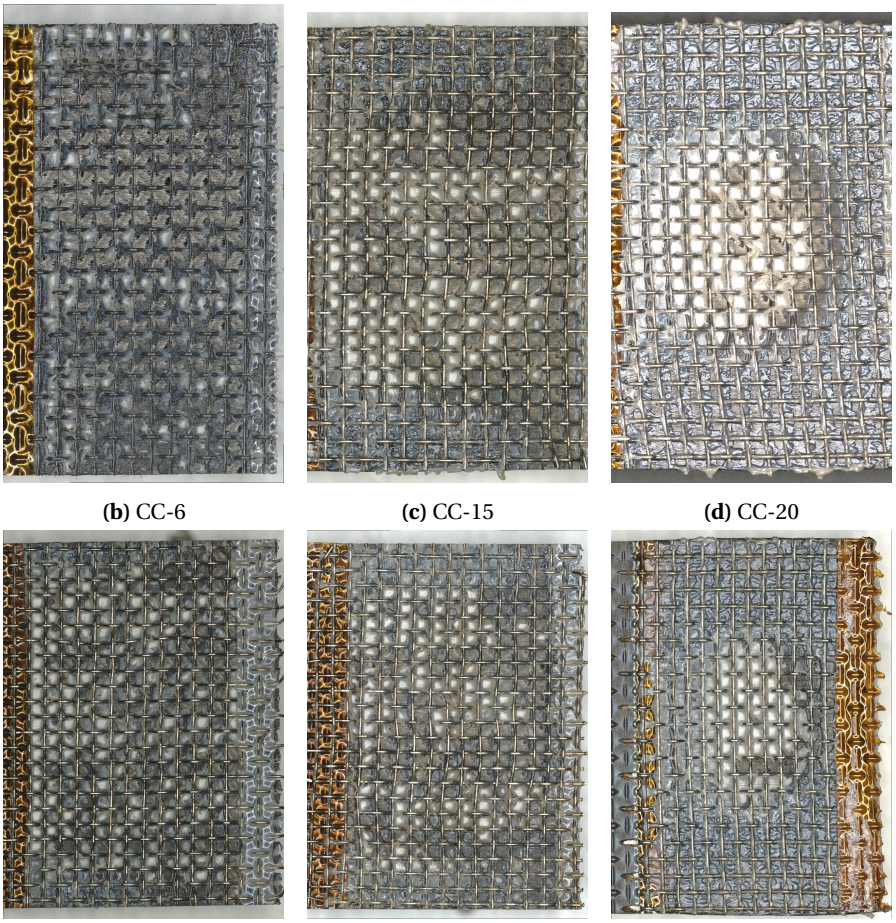
In the thesis report, fracture surfaces and cross-sections of one sample per weight level are shown. In this appendix, 2 more samples per weight level will be depicted when possible.

D.1. Fracture surfaces

Samples of which fracture surfaces are already depicted in the report are listed in table D.1. The other fracture surfaces will be shown in a similar fashion as in the report, i.e. in series that show the evolution with changing weight levels. For co-consolidated samples with susceptor, no more fracture surfaces at 15 kg were available since only one sample was tested at this level. For ultrasonically welded samples, only one more sample at 10 kg was available. The missing weight levels are indicated in the figure. All sample names in figure captions and in table D.1 are referring to the names used in table 4.4.

Table D.1: Sample names of fracture surfaces shown in report

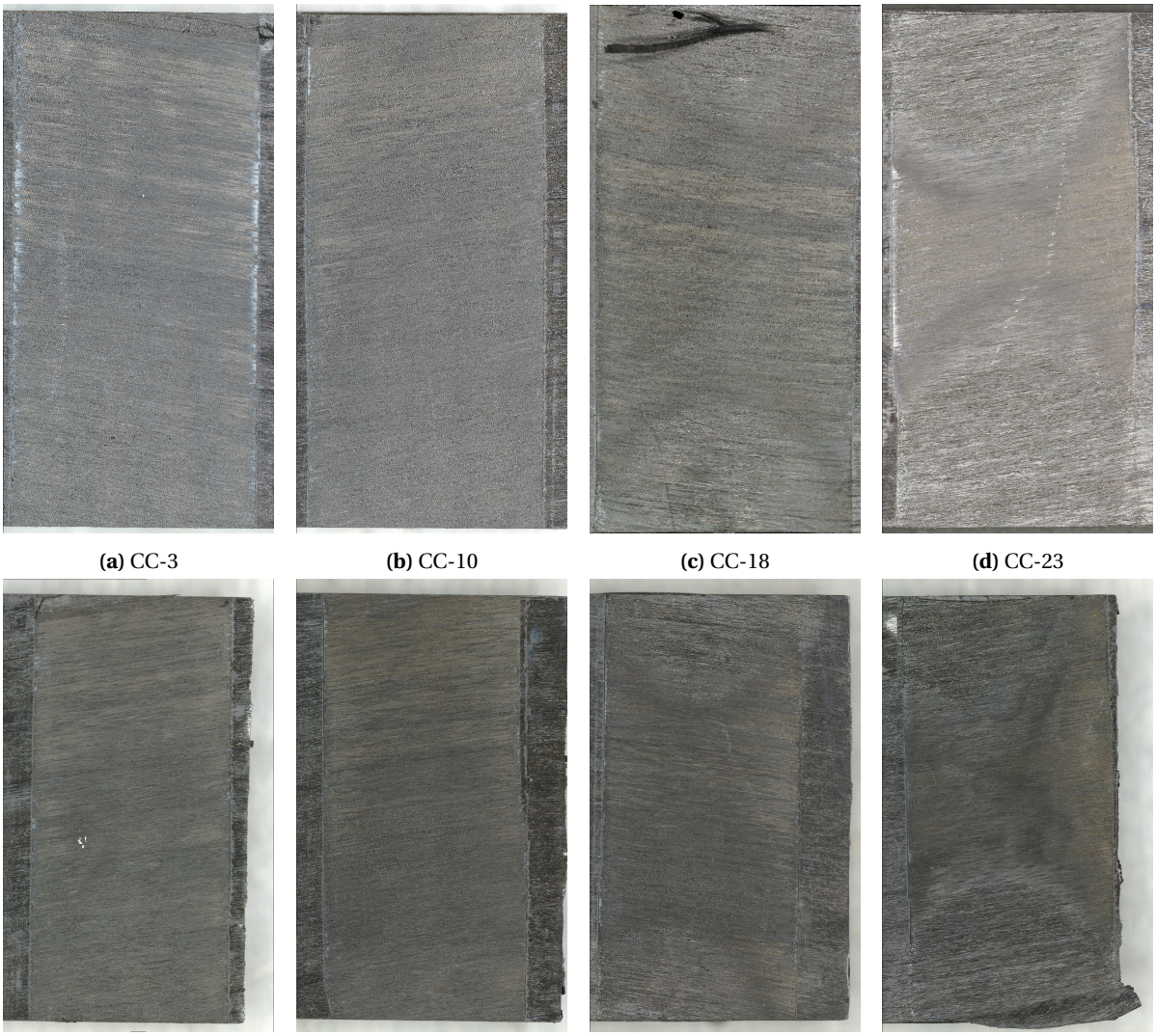
	15 kg	**10 kg**	**5 kg**	**0 kg**
with mesh	CC-1	CC-9	CC-16	CC-22
without mesh	CC-5	CC-12	CC-19	CC-26
welded	USW-3	USW-9	USW-11	USW-15



(a) 15 kg missing **(b)** CC-6 **(c)** CC-15 **(d)** CC-20

(e) 15 kg missing **(f)** CC-8 **(g)** CC-14 **(h)** CC-21

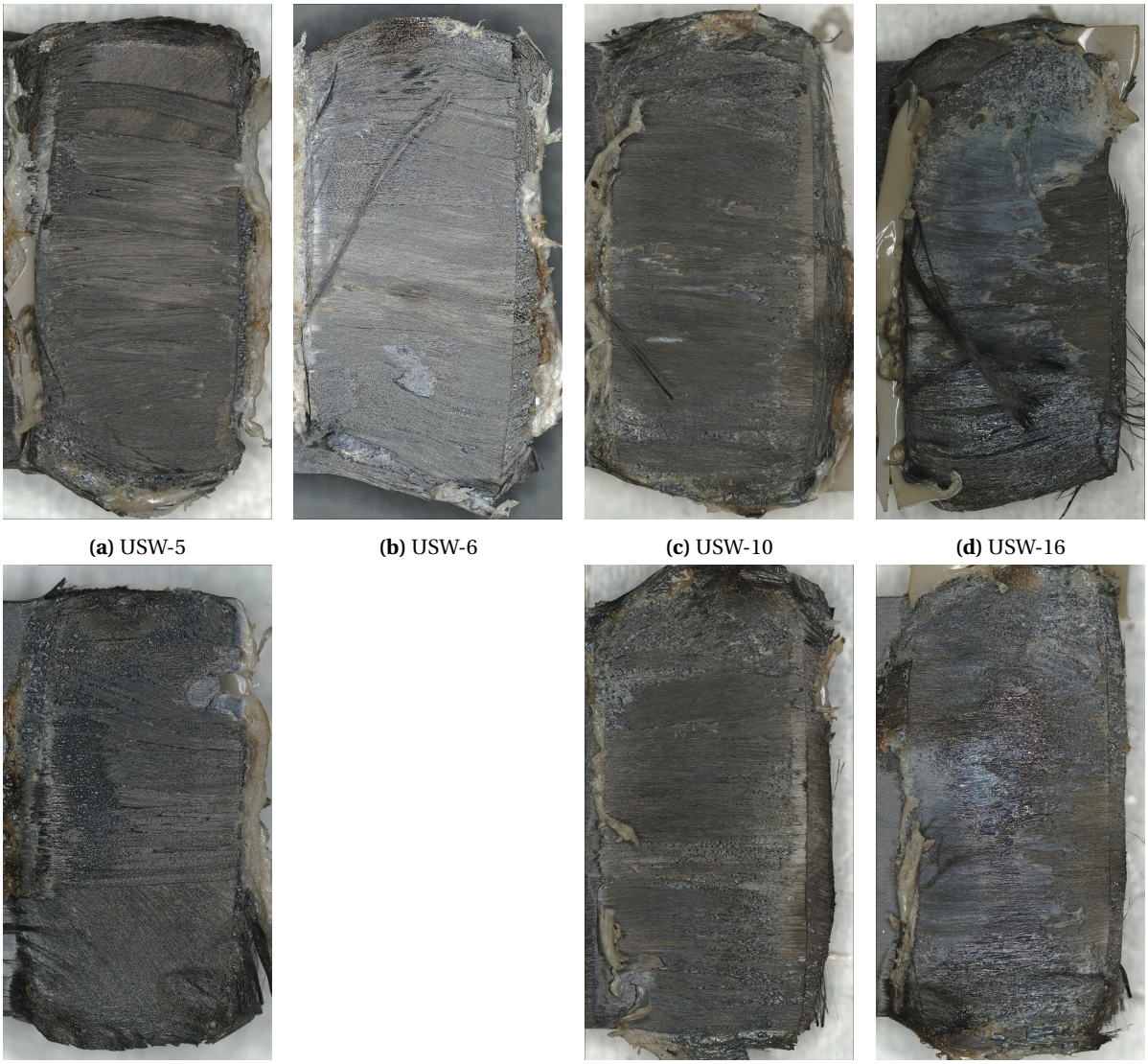
Figure D.1: Two series of fracture surfaces of co-consolidated samples with susceptor, ordered from highest to lowest weight level. No more samples at 15 kg were tested.



(a) CC-3 **(b)** CC-10 **(c)** CC-18 **(d)** CC-23

(e) CC-4 **(f)** CC-11 **(g)** CC-17 **(h)** CC-24

Figure D.2: Two series of fracture surfaces of co-consolidated samples without susceptor, ordered from highest to lowest weight level



(a) USW-5 **(b)** USW-6 **(c)** USW-10 **(d)** USW-16

(e) USW-1 **(f)** 10 kg missing **(g)** USW-12 **(h)** USW-18

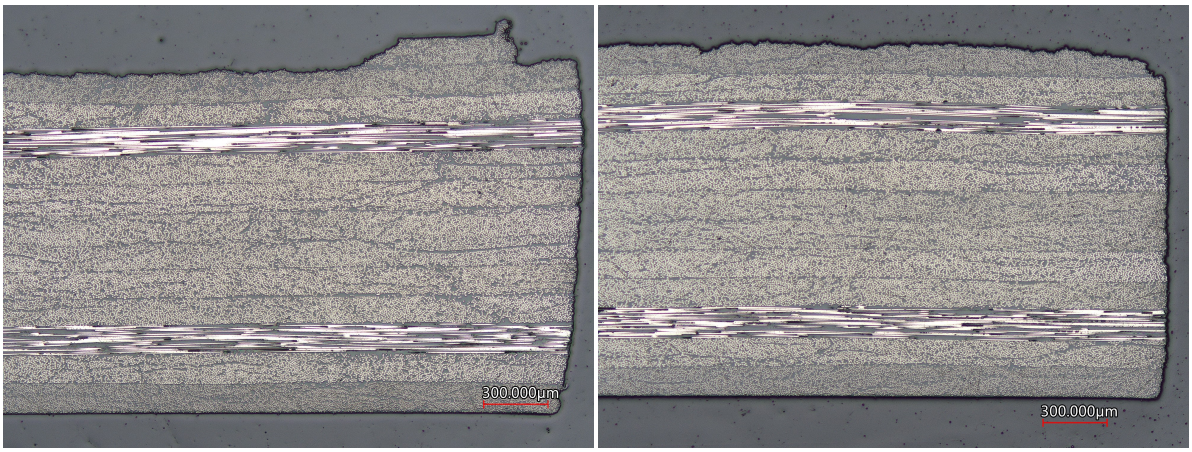
Figure D.3: Two series of fracture surfaces of ultrasonically welded samples, ordered from highest to lowest weight level. Only two samples were successfully disassembled at 10 kg (one in report, one in this figure).

D.2. Cross-sections

Samples of which cross-sections are already shown in the report are listed in table D.2. Other cross-sections are shown in this section. For co-consolidated samples, the sample's edge will be depicted and at 0 kg the damage pattern will be shown by using three pictures to "assemble" the full cross-section. For ultrasonically welded samples, three pictures per cross-section will also be given to get a better overview of the full cross-section. The captions of all figures and the codes used in the table refer to the sample names of table 4.4.

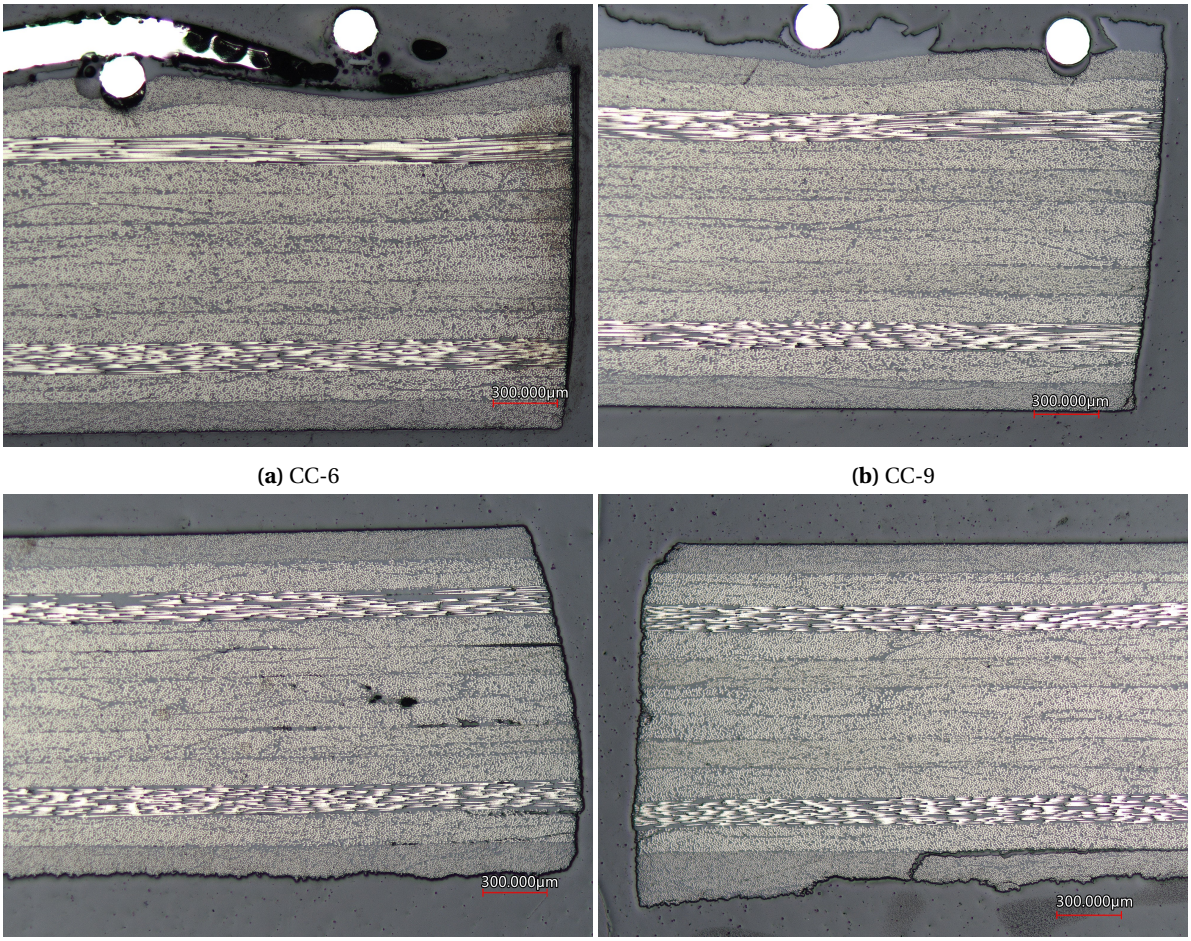
Table D.2: Sample names of cross-sections shown in report

	15 kg	**10 kg**	**5 kg**	**0 kg**
with mesh	CC-1	CC-8	CC-15	CC-21
without mesh	CC-5	CC-12	CC-18	CC-23
welded	USW-3	USW-9	USW-11	USW-15



(a) CC-3 **(b)** CC-4

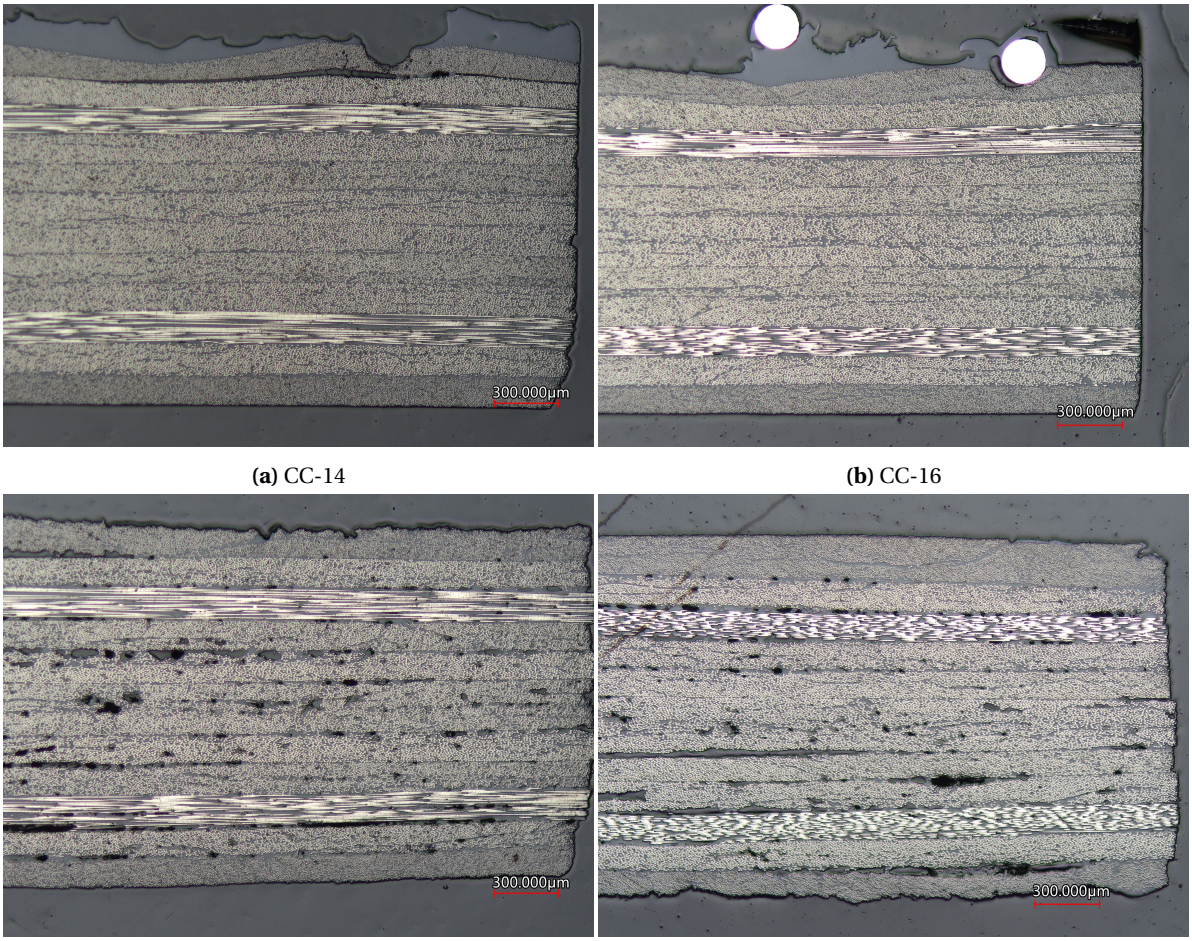
Figure D.4: Cross-sections of co-consolidated samples disassembled at 15 kg. Only one sample with susceptor was disassembled at this level. This sample is already shown in the main report.



(a) CC-6 **(b)** CC-9

(c) CC-11 **(d)** CC-13

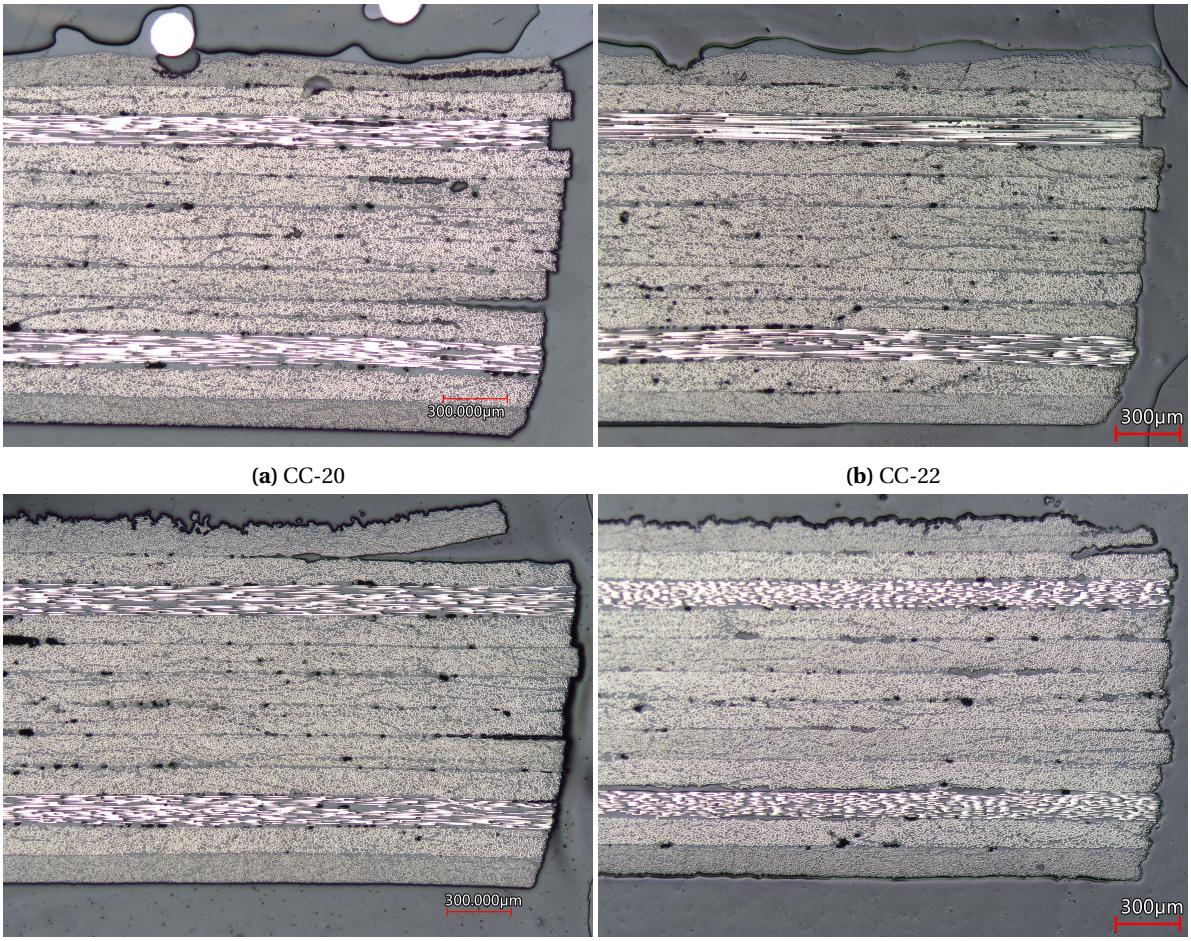
Figure D.5: Cross-sections of co-consolidated samples disassembled at 10 kg



(a) CC-14 **(b)** CC-16

(c) CC-17 **(d)** CC-19

Figure D.6: Cross-sections of co-consolidated samples disassembled at 5 kg

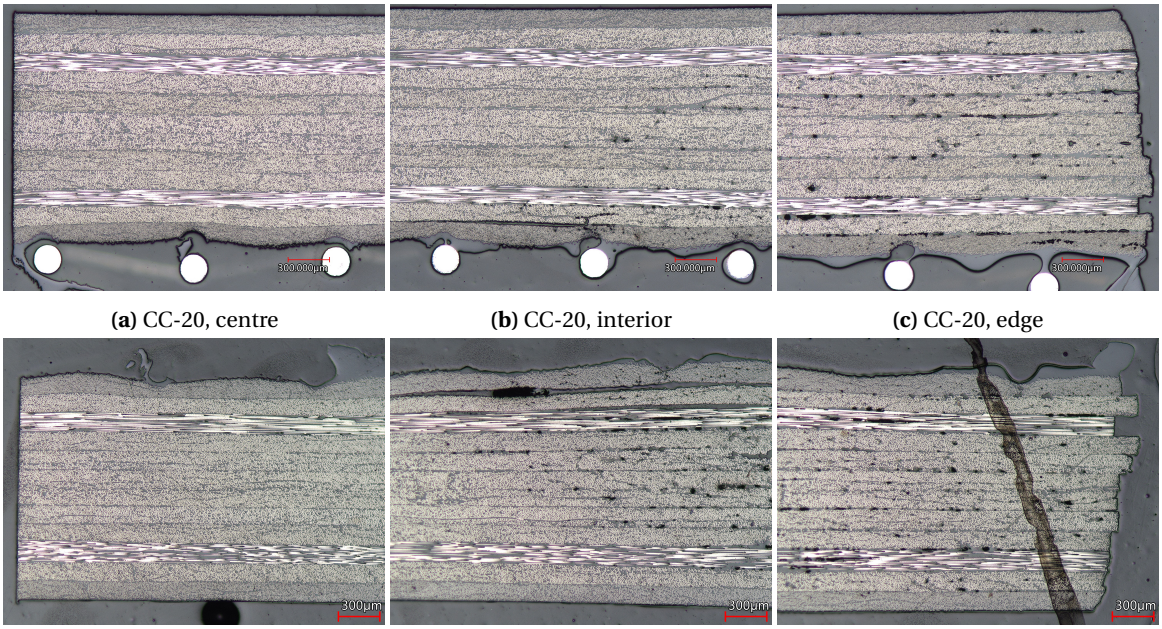


(a) CC-20 **(b)** CC-22

(c) CC-24 **(d)** CC-25

Figure D.7: Cross-sections of co-consolidated samples disassembled at 0 kg

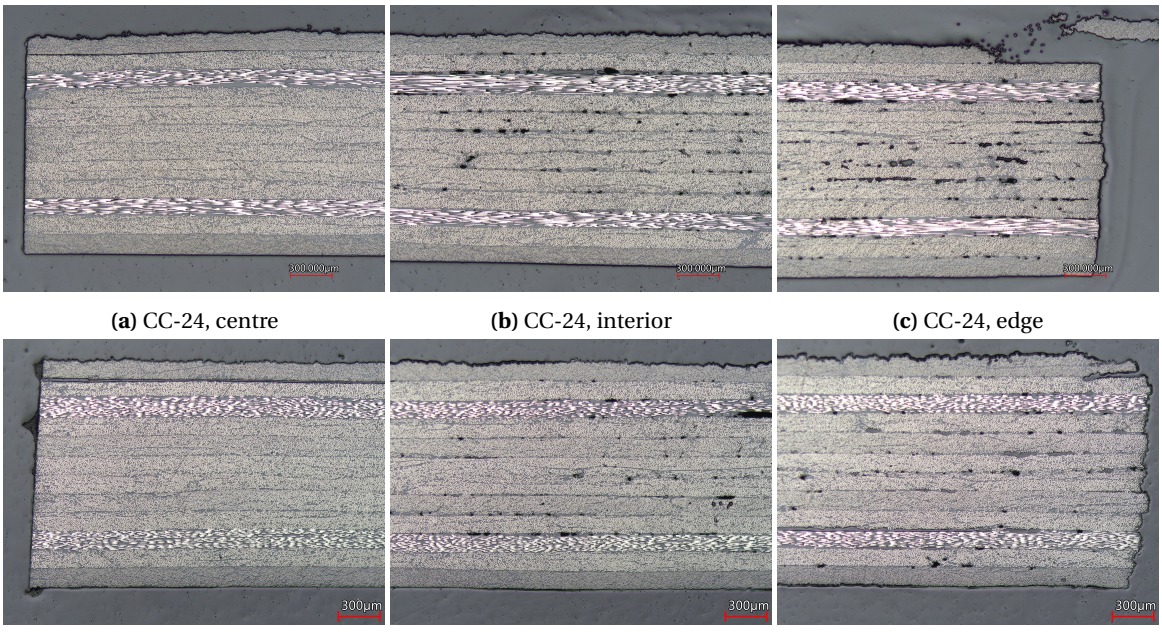
To identify differences between co-consolidated samples with and without susceptor, full cross-sections of samples disassembled at 0 kg were given in figure 4.31 (samples CC-21 and CC-23). The main takeaway of this figure was that damage patterns were different at the coil-facing adherend. When moving from the edge to the centre of the joint, damage faded first at the sample's coil-facing surface and only later at the interface, while for susceptorless samples the damage faded simultaneously throughout the thickness. Due to time constraints, no more full cross-section pictures were taken. Instead, pictures of the edge, interior and centre will be shown. The damage transition is visible in the "interior" picture.



(a) CC-20, centre **(b)** CC-20, interior **(c)** CC-20, edge

(d) CC-22, centre **(e)** CC-22, interior **(f)** CC-22, edge

Figure D.8: Damage pattern on cross-sections of co-consolidated samples with susceptor disassembled at 0 kg

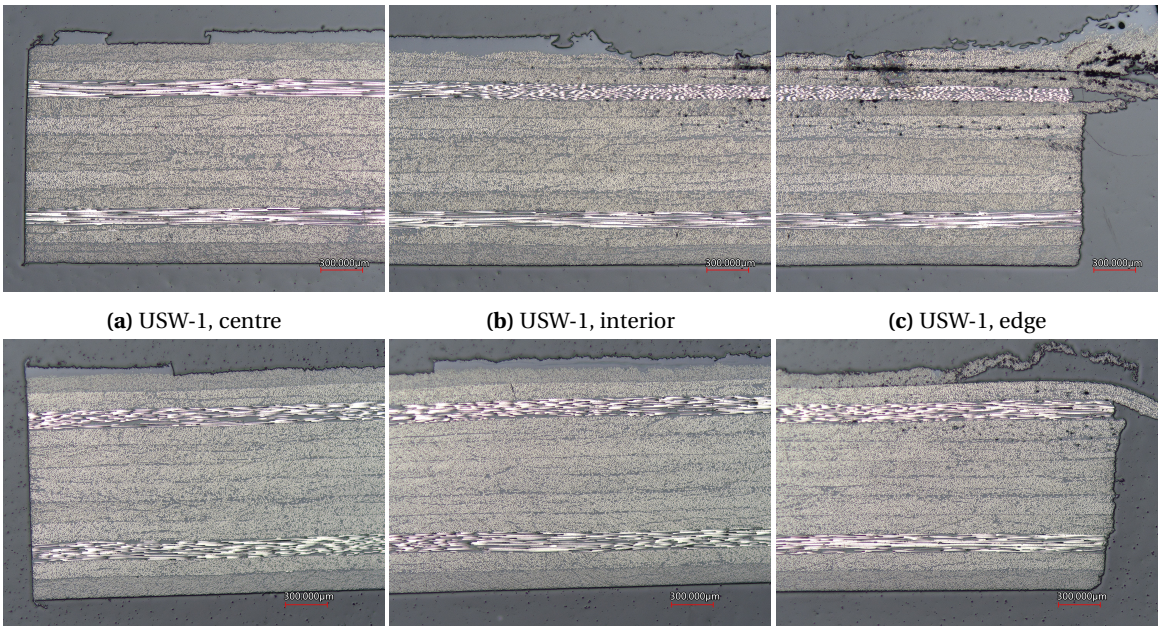


(a) CC-24, centre **(b)** CC-24, interior **(c)** CC-24, edge

(d) CC-25, centre **(e)** CC-25, interior **(f)** CC-25, edge

Figure D.9: Damage pattern on cross-sections of co-consolidated samples without susceptor disassembled at 0 kg

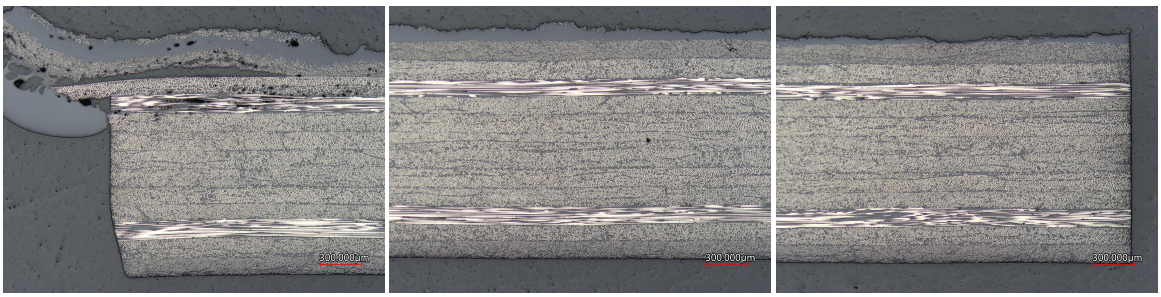
For ultrasonically welded samples, cross-sections are again "assembled" out of 3 pictures. At 5 kg and 0 kg damage inflicted during disassembly starts becoming visible. Therefore, both coil-facing and coil-opposing cross-sections are given for these weight levels. In the report, the 5 kg load case was also compared with susceptorless co-consolidated samples. This will be done here too, by depicting 6 pictures (3 per side) for CC-24 and CC-25.



(a) USW-1, centre **(b)** USW-1, interior **(c)** USW-1, edge

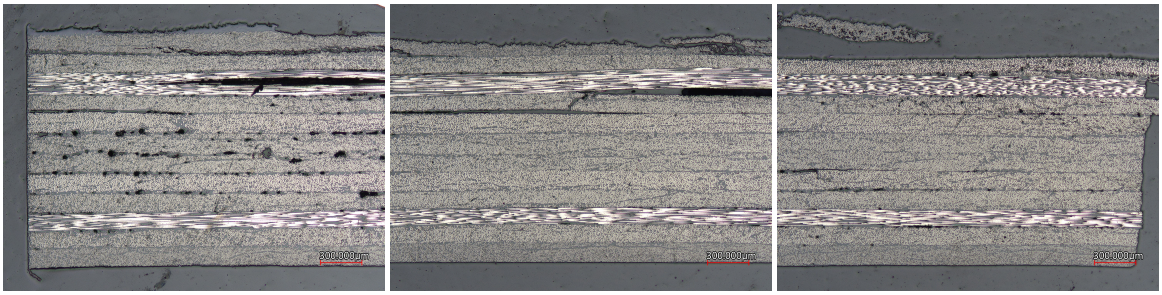
(d) USW-5, centre **(e)** USW-5, interior **(f)** USW-5, edge

Figure D.10: Cross-sections of ultrasonically welded samples disassembled at 15 kg

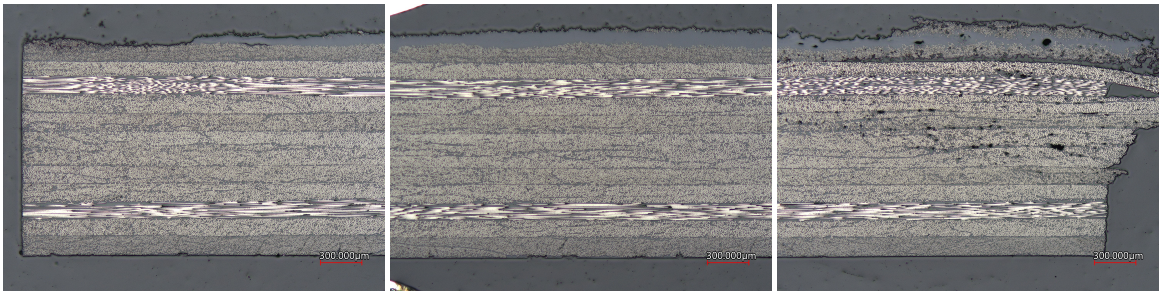


(a) USW-6, edge **(b)** USW-6, interior **(c)** USW-6, centre

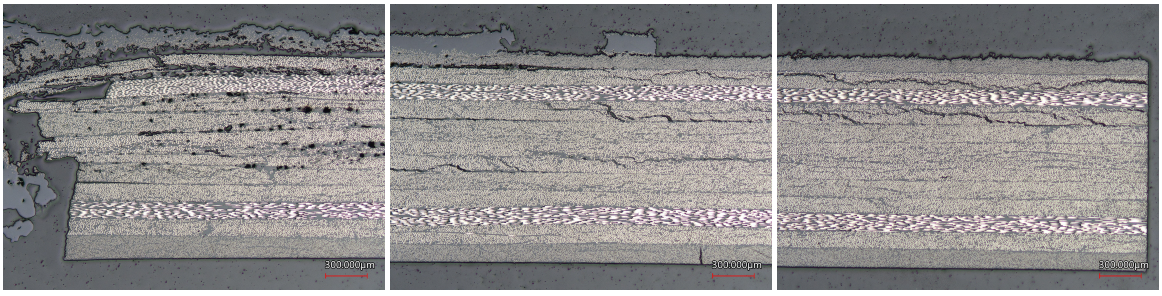
Figure D.11: Cross-sections of ultrasonically welded samples disassembled at 10 kg. Only two samples were successfully disassembled at this level, the other one is shown in the report.



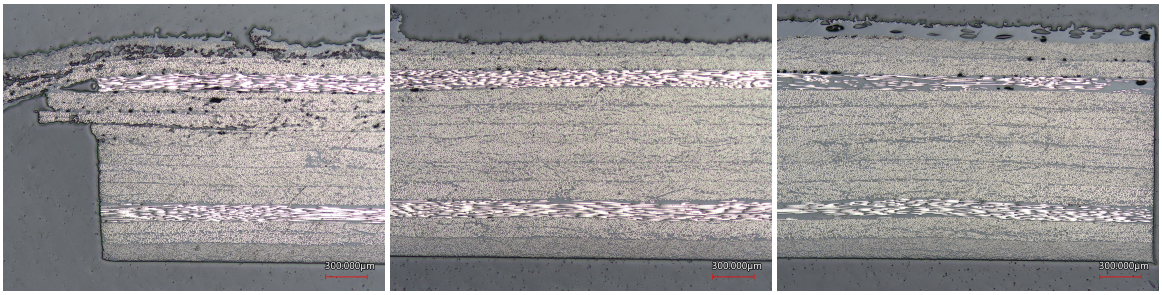
(a) USW-10, centre, coil-facing **(b)** USW-10, interior, coil-facing **(c)** USW-10, edge, coil-facing



(d) USW-10, centre, coil-opposing **(e)** USW-10, interior, coil-opposing **(f)** USW-10, edge, coil-opposing

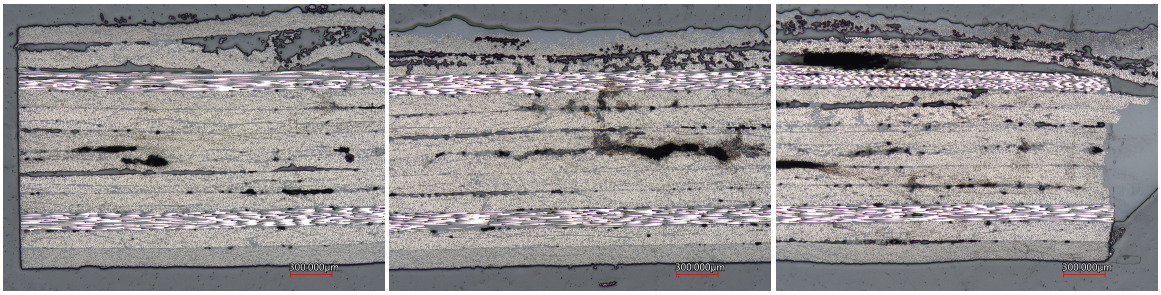


(g) USW-12, edge, coil-facing **(h)** USW-12, interior, coil-facing **(i)** USW-12, centre, coil-facing

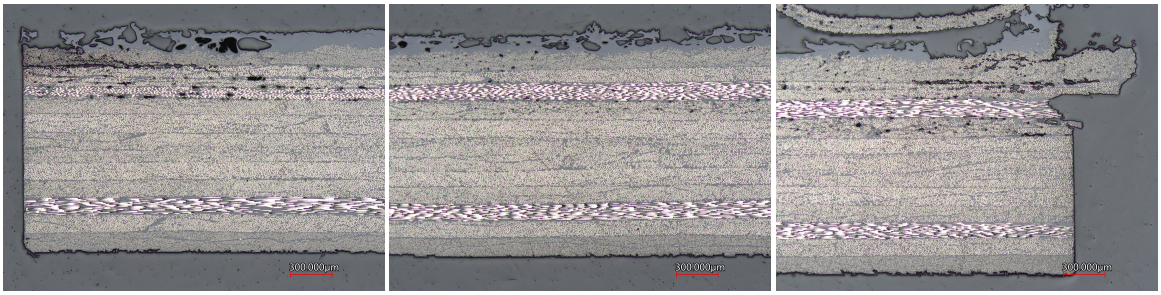


(j) USW-12, edge, coil-opposing **(k)** USW-12, interior, coil-opposing **(l)** USW-12, centre, coil-opposing

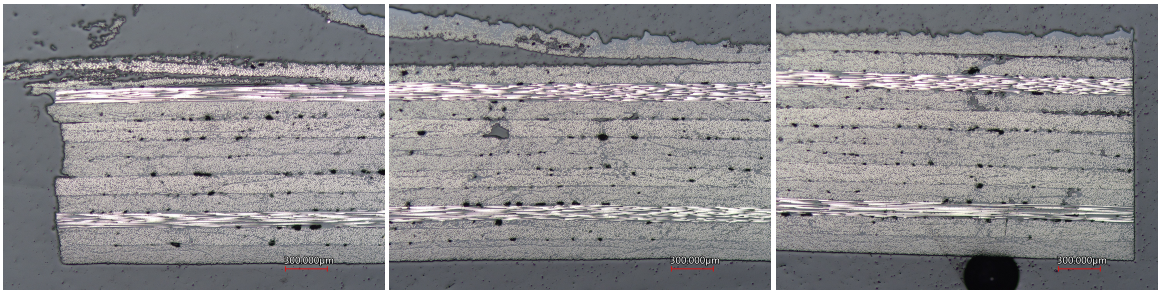
Figure D.12: Cross-sections of ultrasonically welded samples disassembled at 5 kg



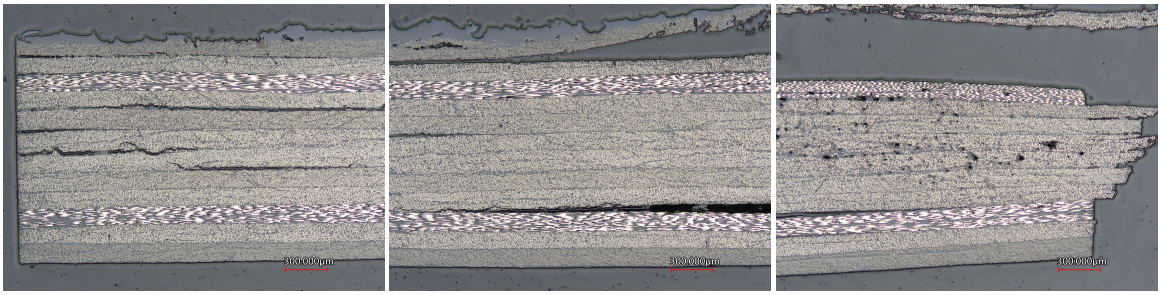
(a) USW-16, centre, coil-facing **(b)** USW-16, interior, coil-facing **(c)** USW-16, edge, coil-facing



(d) USW-16, centre, coil-opposing **(e)** USW-16, interior, coil-opposing **(f)** USW-16, edge, coil-opposing

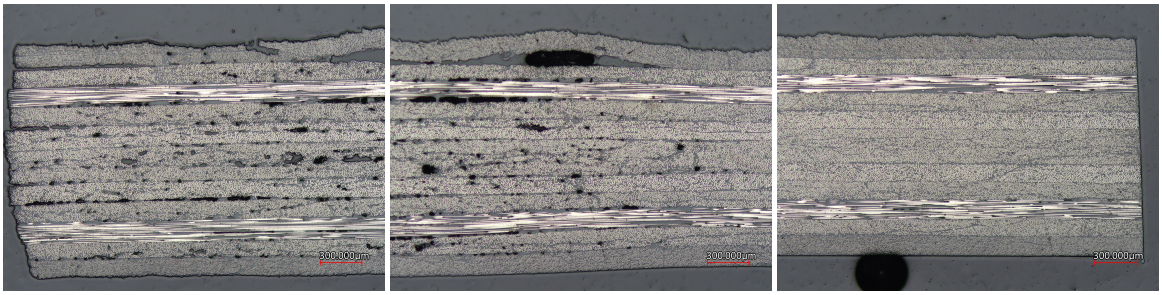


(g) USW-18, edge, coil-facing **(h)** USW-18, interior, coil-facing **(i)** USW-18, centre, coil-facing

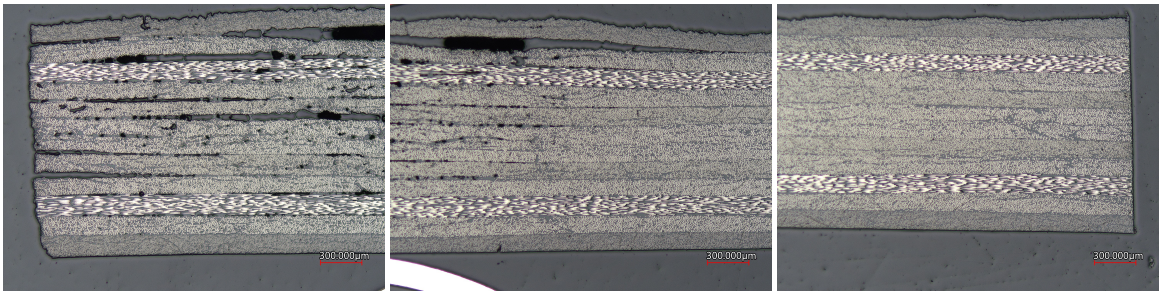


(j) USW-18, centre, coil-opposing **(k)** USW-18, interior, coil-opposing **(l)** USW-18, edge, coil-opposing

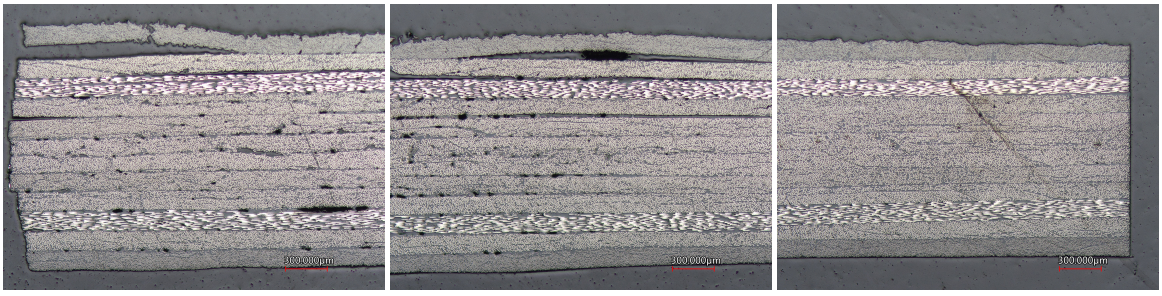
Figure D.13: Cross-sections of ultrasonically welded samples disassembled at 0 kg



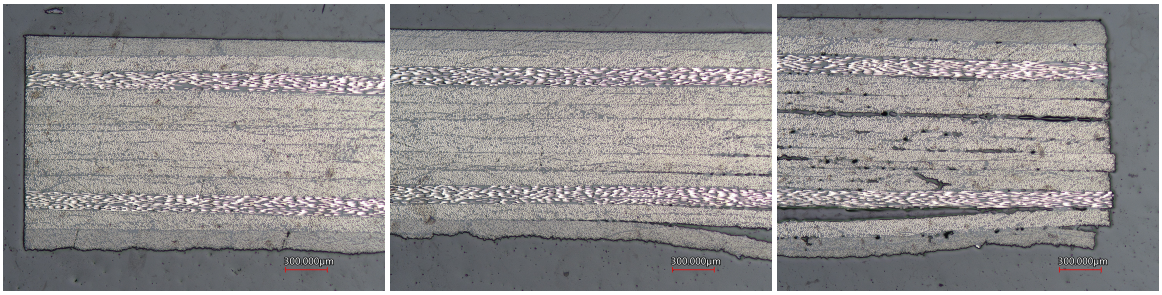
(a) CC-17, edge, coil-facing **(b)** CC-17, interior, coil-facing **(c)** CC-17, centre, coil-facing



(d) CC-17, edge, coil-opposing **(e)** CC-17, interior, coil-opposing **(f)** CC-17, centre, coil-opposing



(g) CC-19, edge, coil-facing **(h)** CC-19, interior, coil-facing **(i)** CC-19, centre, coil-facing



(j) CC-19, centre, coil-opposing **(k)** CC-19, interior, coil-opposing **(l)** CC-19, edge, coil-opposing

Figure D.14: Cross-sections of co-consolidated samples without susceptor, disassembled at 5 kg

Bibliography

[1] C. Ageorges, L. Ye, and M. Hou. Experimental investigation of the resistance welding for thermoplastic-matrix composites. part i: Heating element and heat transfer. *Composites Science and Technology*, 60(7): 1027–1039, 2000. doi: 10.1016/S0266-3538(00)00005-1.

[2] C. Ageorges, L. Ye, and M. Hou. Experimental investigation of the resistance welding of thermoplastic-matrix composites. part ii: Optimum processing window and mechanical performance. *Composites Science and Technology*, 60(8):1191–1202, 2000.

[3] C. Ageorges, L. Ye, and M. Hou. Advances in fusion bonding techniques for joining thermoplastic matrix composites: A review. *Composites - Part A: Applied Science and Manufacturing*, 32(6):839–857, 2001. doi: 10.1016/S1359-835X(00)00166-4.

[4] T. Bayerl, M. Duhovic, P. Mitschang, and D. Bhattacharyya. The heating of polymer composites by electromagnetic induction – a review. *Composites Part A: Applied Science and Manufacturing*, 57:27–40, 2014. ISSN 1359-835X. doi: https://doi.org/10.1016/j.compositesa.2013.10.024.

[5] S. Becker and P. Mitschang. Influences of laminate parameters on the induction behavior of cfrpc, June 2018. 18th International Conference on Composite Materials, Xi'an.

[6] M. R. Choudhury and K. Debnath. A review of the research and advances in electromagnetic joining of fiber-reinforced thermoplastic composites. *Polymer Engineering & Science*, 59(10):1965–1985, 2019. ISSN 0032-3888. doi: 10.1002/pen.25207.

[7] A.J.D. de Bruin, I. Fernandez Villegas, and C.A. Dransfeld. *Investigating the Degree of Crystallinity in Ultrasonically Welded Thermoplastic Composite Joints*. Thesis, Delft University of Technology, 2020.

[8] M. Dhondt, J. Stüve, and N. Menke. *Induction welding of high performance thermoplastic composites: Focused heat generation in weld zones of carbon fiber laminates by magnetic field manipulation and carbon fiber susceptors*. Thesis, Delft University of Technology, 2020.

[9] M. Dubé, P. Hubert, J. N. A. H. Gallet, D. Stavrov, H. E. N. Bersee, and A. Yousefpour. Fatigue performance characterisation of resistance-welded thermoplastic composites. *Composites Science and Technology*, 68(7-8):1759–1765, 2008. doi: 10.1016/j.compscitech.2008.02.012.

[10] M. Duhovic, P. L'Eplattenier, I. Caldichoury, and J. Hausmann. Advanced 3d finite element simulation of thermoplastic composite induction welding. In *ICCM International Conferences on Composite Materials*, volume 2015-July, 2015.

[11] I. Fernandez Villegas. Strength development versus process data in ultrasonic welding of thermoplastic composites with flat energy directors and its application to the definition of optimum processing parameters. *Composites Part A: Applied Science and Manufacturing*, 65:27–37, 2014. doi: 10.1016/j.compositesa.2014.05.019.

[12] I. Fernandez Villegas. In situ monitoring of ultrasonic welding of thermoplastic composites through power and displacement data. *Journal of Thermoplastic Composite Materials*, 28(1):66–85, 2015. doi: 10.1177/0892705712475015.

[13] I. Fernandez Villegas. Ultrasonic welding of thermoplastic composites. *Frontiers in Materials*, 6, 2019. doi: 10.3389/fmats.2019.00291.

[14] I. Fernandez Villegas, L. Moser, A. Yousefpour, P. Mitschang, and H. E. N. Bersee. Process and performance evaluation of ultrasonic, induction and resistance welding of advanced thermoplastic composites. *Journal of Thermoplastic Composite Materials*, 26(8):1007–1024, 2013. doi: 10.1177/0892705712456031.

[15] P. Gouin O'Shaughnessey, M. Dubé, and I. Fernandez Villegas. Modeling and experimental investigation of induction welding of thermoplastic composites and comparison with other welding processes. *Journal of Composite Materials*, 50(21):2895–2910, 2016. ISSN 0021-9983. doi: 10.1177/0021998315614991.

[16] D.A. Grewell, A. Benatar, and J.B. Park. *Plastics and Composites Welding Handbook*. Hanser Gardener, 2003. ISBN 9781569903131.

[17] W. Grouve, E. Vruggink, F. Sacchetti, and R. Akkerman. Induction heating of ud c/pekk cross-ply laminates. In *Procedia Manufacturing*, volume 47, pages 29–35, 2020. doi: 10.1016/j.promfg.2020.04.112.

[18] M. Hagenbeek, J.V. Bramon, and I. Fernandez Villegas. Controlling the edge effect using a bypass conductor for induction welding of carbon fibre thermoplastic composites. 2018.

[19] M. Haq and L. T. Drzal. Active, tailorable adhesives for dissimilar material bonding, repair and reassembly. Report DOE-MSU-EE0006424, Michigan State Univ., East Lansing, MI (United States), 2019.

[20] Hexcel. Hexcel hextow as4 carbon fiber (technical data sheet). URL `https://www.hexcel.com/user_area/content_media/raw/AS4_HexTow_DataSheet.pdf`. accessed on 22.03.2021.

[21] C.Y. Ho and T.K. Chu. Electrical resistivity an dthermal conductivity of nine selected aisi stainless steels. Technical report, Thermophysical properties research center, 1977.

[22] S. T. Holmes and J. W. Gillespie. Thermal analysis for resistance welding of large-scale thermoplastic composite joints. *Journal of Reinforced Plastics and Composites*, 12(6):723–736, 1993. doi: 10.1177/073168449301200609.

[23] A. Hutchinson, Y. Liu, and Y. Lu. Overview of disbonding technologies for adhesive bonded joints. *The Journal of Adhesion*, 93(10):737–755, 2017. ISSN 0021-8464. doi: 10.1080/00218464.2016.1237876.

[24] M. Irfan and M. Raza. A simple method for generation of statistical tables by the help of excel software. *Journal of Social and Development Sciences*, 2:38–50, 07 2011. doi: 10.22610/jsds.v2i1.651.

[25] N. Koutras, R. Benedictus, and I. Fernandez Villegas. *Thermal effects on thermoplastic composites welded joints: A physical and mechanical characterisation.* doctoral thesis, Delft University of Technology, 2020. URL `https://repository.tudelft.nl/islandora/object/uuid%3A8bdf06e6-8e42-463a-af45-20a56e0e2022?collection=research`.

[26] A. Levy, S. Le Corre, and A. Poitou. Ultrasonic welding of thermoplastic composites: A numerical analysis at the mesoscopic scale relating processing parameters, flow of polymer and quality of adhesion. *International Journal of Material Forming*, 7(1):39–51, 2014. doi: 10.1007/s12289-012-1107-6.

[27] X. Ma, F. Scarpa, H. Peng, G. Allegri, J. Yuan, and R. Ciobanu. Design of a hybrid carbon fibre/carbon nanotube composite for enhanced lightning strike resistance. *Aerospace Science and Technology*, 47: 367–377, 2015. ISSN 1270-9638. doi: https://doi.org/10.1016/j.ast.2015.10.002.

[28] matweb. Aisi type 304 stainless steel. URL `http://www.matweb.com/search/datasheet.aspx?matguid=bd20a4281ae3430d97cfbebf6904ec50&ckck=1`. accessed on 21.03.2021.

[29] R. H. McCurdy, A. R. Hutchinson, and P. H. Winfield. The mechanical performance of adhesive joints containing active disbonding agents. *International Journal of Adhesion and Adhesives*, 46:100–113, 2013. ISSN 0143-7496. doi: https://doi.org/10.1016/j.ijadhadh.2013.06.001.

[30] Metalcor. Datasheet 1.4301. URL `http://www.metalcor.de/en/datenblatt/5/`. accessed on 21.03.2021.

[31] L. Moser. *Experimental Analysis and Modeling of Susceptorless Induction Welding of High Performance Thermoplastic Polymer Composites.* Thesis, Institut für Verbundwerkstoffe GmbH, 2012.

[32] G. Palardy and I. Fernandez Villegas. On the effect of flat energy directors thickness on heat generation during ultrasonic welding of thermoplastic composites. *Composite Interfaces*, 24(2):203–214, 2017. doi: 10.1080/09276440.2016.1199149. URL `https://www.scopus.com/inward/record.uri?eid=2-s2.0-84975138850&doi=10.1080%2f09276440.2016.1199149&partnerID=40&md5=73899e6c777faee7882899076afb0b22https://www.tandfonline.com/doi/pdf/10.1080/09276440.2016.1199149?needAccess=true`.

[33] N. Pausan, Y. Liu, Y. Lu, and A. R. Hutchinson. The use of expandable graphite as a disbonding agent in structural adhesive joints. *The Journal of Adhesion*, 93(10):791–810, 2017. ISSN 0021-8464. doi: 10.1080/00218464.2016.1226169.

[34] S. Roychowdhury, J. W. Gillespie, and S. G. Advani. *Void Formation and Growth in Thermoplastic Processing*, pages 89–107. Springer Netherlands, Dordrecht, 1992. ISBN 978-94-011-2874-2. doi: 10.1007/978-94-011-2874-2_7. URL https://doi.org/10.1007/978-94-011-2874-2_7.

[35] A. Smalcerz and R. Przylucki. Impact of electromagnetic field upon temperature measurement of induction heated charges. *International Journal of Thermophysics*, 34(4):667–679, 2013. doi: 10.1007/s10765-013-1423-1.

[36] S. Staicovici, C. Y. Wu, and A. Benatar. Welding and disassembly of microwave welded hdpe bars. *Journal of Reinforced Plastics and Composites*, 18(1):35–43, 1999. doi: 10.1177/073168449901800104.

[37] D. Stavrov and H. E. N. Bersee. Resistance welding of thermoplastic composites - an overview. *Composites Part a-Applied Science and Manufacturing*, 36(1):39–54, 2005. ISSN 1359-835X. doi: 10.1016/j.compositesa.2004.06.030.

[38] L. Taerwe and N. De Belie. *Statistische gegevensverwerking*. Universiteit Gent, 2018.

[39] Toray. Toray cetex tc1200 peek (technical data sheet). URL https://www.toraytac.com/media/7765d981-1f9f-472d-bf24-69a647412e38/Pr7gdw/TAC/Documents/Data_sheets/Thermoplastic/UD%20tapes,%20prepregs%20and%20laminates/Toray-Cetex-TC1200_PEEK_PDS.pdf. accessed on 22.03.2021.

[40] Victrex. Victrex peek 450g (technical data sheet). URL https://www.victrex.com/~/media/datasheets/victrex_tds_450g.pdf. accessed on 21.03.2021.

[41] I.F. Villegas, B. Valle Grande, H. E. N. Bersee, and R. Benedictus. A comparative evaluation between flat and traditional energy directors for ultrasonic welding of cf/pps thermoplastic composites. *Composite Interfaces*, 22(8):717–729, 2015. doi: 10.1080/09276440.2015.1053753.

[42] J. Xu and R. Wirtz. In-plane effective thermal conductivity of plain-weave screen laminates. *IEEE Transactions on Components and Packaging Technologies*, 25:615–620, 2002.

[43] S. Yarlagadda, H. J. Kim, J. W. Gillespie Jr, N. B. Shevchenko, and B. K. Fink. A study on the induction heating of conductive fiber reinforced composites. *Journal of Composite Materials*, 36(4):401–421, 2002. doi: 10.1177/0021998302036004171.

[44] A. Yousefpour, M. Hojjati, and J. P. Immarigeon. Fusion bonding/welding of thermoplastic composites. *Journal of Thermoplastic Composite Materials*, 17(4):303–341, 2004. doi: 10.1177/0892705704045187.

[45] Z. Zhao, Y. Peles, and M. K. Jensen. Properties of plain weave metallic wire mesh screens. *International Journal of Heat and Mass Transfer*, 57(2):690–697, 2013. ISSN 0017-9310. doi: https://doi.org/10.1016/j.ijheatmasstransfer.2012.10.055.

[46] S. Zinn, S. L. Semiatin, S. L. Semiatin, S. Zinn, and S. L. Semiatin. *Elements of Induction Heating : Design, Control, and Applications*. A S M International, Materials Park, UNITED STATES, 1988. ISBN 9781615031986.